1-1-2014

Residual-based Variational Multiscale LES with Wall-modeling for Oceanic Boundary Layers in Shallow Water

Roozbeh Golshan
University of South Florida, rgolshan@mail.usf.edu

Residual-based Variational Multiscale LES with Wall-modeling for Oceanic Boundary Layers in Shallow Water

by

Roozbeh Golshan

A dissertation submitted in partial fulfillment
of the requirements for the degree of
Doctor of Philosophy
Department of Civil and Environmental Engineering
College of Engineering
University of South Florida

Major Professor: Andrés E. Tejada-Martínez, Ph.D.
Yuncheng You, Ph.D.
Rasim Guldiken, Ph.D.
Autar Kaw, Ph.D.
Daniel C. Simkins, Jr., Ph.D.

Date of Approval:
November 4, 2014

Keywords: Langmuir Circulation, Residual-based Variational Multiscale (RBVMS) Method, Wall Modeling

Dedication

To glorious memory of Alan Turing...

Acknowledgments

First and foremost I would like to express my special appreciation to my advisor Dr. Andrés E. Tejada-Martínez. Without his support, guidance and patience, compilation of the research and this thesis would have been inconceivable.

I also am very grateful to my committee members: Dr. Rasim Guldiken, Dr. Autar Kaw Prof. Yuncheng You, & Dr. Daniel C. Simkins, Jr. for their time and interest. Some of the best classes I attended during my studies were offered by them and I truly appreciate that.

I also gratefully acknowledge National Science Foundation for providing the funding sources that made my Ph.D. work possible.

It was a pleasure to share doctoral studies with the wonderful people in our research group: Nityanand Sinha, Cigdem Akan, Rachel Walker, Amine Hafsi and Jie Zhang. Last but not the least, I would like to thank my family for everything they did for me.

Table of Contents

List of Tables

List of Figures

Abstract

Large-eddy simulation (LES) of wind and wave forced oceanic turbulent boundary layers is performed using the residual-based variational multiscale method (RBVMS) and near-wall modeling. Wind and surface gravity wave forcing generates Langmuir turbulence characterized by Langmuir circulation (LC) with largest scales consisting of streamwise vortices aligned in the direction of the wind, acting as a secondary flow structure to the primary wind-driven component of the flow. The LES here is representative of a shallow water continental shelf flow (10 to 30 meters in depth) far from lateral boundaries in which LC engulfs the full depth of the water column and disrupts the bottom log layer. Field measurements indicate that occurrence of full-depth LC is typical during the passage of storms. The RBVMS method with quadratic NURBS (Non-Uniform Rational B-splines) with near-wall resolution is shown to possess good convergence characteristics for this flow. The use of near-wall modeling facilitates simulations with expanded domains over horizontal directions. Thus, these simulations are able to resolve multiple Langmuir cells permitting analysis of the interaction between the cells. Results in terms of velocity statistics are presented from simulations performed with various domain sizes and distinct near-wall treatments: (1) the classical treatment based on prescription of the wall shear stress assuming a law of the wall and (2) a recent treatment based on weak imposition of the no-slip bottom boundary condition.

Chapter 1:

Introduction

1.1 Introduction to Turbulence and Turbulence-Resolving Computation

Turbulence is a commonly occurring phenomenon influencing many aspects of our lives. Turbulence is experienced by us all the time and everywhere one can imagine. Fluid flows around cars, ships and air crafts, blood flow in our veins and flows in the atmosphere and oceans can all be characterized as turbulent flows spanning different spatial and temporal ranges of scales.

During his laboratory experiments on water flow through long tubes in 1883, Osborne Reynolds introduced the dimensionless Reynolds number, *Re*, to characterize pipe flows into laminar or turbulence regimes. Reynolds' published article based on those experiments was the first step towards scientific study of turbulence. Reynolds showed that the smooth flow in a pipe breaks down into a random, chaotic and eddying turbulent motion when $Re \geq 2000$. The Reynolds number is directly proportional to pipe diameter and mean velocity of the fluid and inversely proportional to the fluid's kinematic viscosity. In a more physical sense, *Re* is the ratio of inertial forces to viscous forces.

Of interest in this research are oceanic boundary layer flows. Looking at averaged Reynolds number values for typical ocean flows (of order of 4×10^8 based on a characteristic velocity scale and length scale) reported in the literature [59], we realize that these values by far exceed the critical value (≈ 2000) prescribed by Reynolds for pipe flows. Although generalizing pipe flows

to averaged ocean flows seems unreasonable and even though Reynolds number values higher than the critical value do not necessarily indicate a turbulent regime, the truth is that the ocean is turbulent with relatively large eddy structures (larger than those in pipe flows).

The motion of fluids is considered as one the most difficult problems of mathematics and modern physics. The existence and uniqueness of solutions to the Navier-Stokes equations which govern fluid flow behavior including turbulence is yet not proved and this problem is considered as one of the seven Millennium Prize Problems. Despite the challenges posed by this problem, a wealth of knowledge has been gained about turbulence through numerical solutions of the Navier-Stokes equations. Capability of numerical simulations of turbulence, however, is limited by serious drawbacks due to the complex nature of turbulent flows and the high price of scientific computing.

Turbulent flows are characterized by fluctuating velocity and pressure fields. There is a wide range of fluctuation scales in a fully turbulent flow. Among these scales or eddies are those of very small size and high frequency which can be less than on the order of millimeters and seconds. Ideally, numerical simulation should be capable of resolving all of the small and large scales characteristic of the turbulence in what is often referred to as direct numerical simulation or DNS. According to [10], the number of grid points required to fully resolve the flow grows as $Re^{9/4}$. As it was discussed earlier, the average Reynolds number for the ocean is of order of 4×10^8. For atmospheric boundary layer flows, the averaged Reynolds number and consequently the aforementioned order are even higher. To this date, DNS for such high Reynolds number flows are well beyond the capability of any existing computer.

Given that DNS is far too expensive to be used in applied fields of engineering and geophysical sciences, introducing proper physical and mathematical models is vital. One of the most popular methods for reducing the cost of turbulence computations is large eddy simulation (LES).

The history of LES dates back to the early 1960s when Smagorinsky [49] introduced his famous subgrid-scale stress model. LES could roughly be described as cutting off those scales smaller than a certain size and explicitly computing (or resolving) the larger scales, giving rise to a computationally less expensive simulation. In traditional LES, the cutting or filtering of small scales is accomplished via application of an explicit low-pass spatial filter to the Navier-Stokes equations.

According to the Kolmogorov energy cascade theory, in a turbulent flow, energy is passed from larger scales to smaller scales [43]. At the smallest scales, molecular viscosity acts as a converter of energy into heat. Thus, small scales play an important role in determining the energy distribution across scales in a turbulent flow and may not be overlooked. In LES, a so called residual stress arises from the filtering of the Navier-Stokes equations, serving to drain energy from the resolved scales thereby modelling the effect of unresolved scales on the resolved ones. This stress is often referred to as the subgrid-scale (SGS) stress as it accounts for the effect of unresolved scales which typically correspond to scales of size on the order of the grid size and smaller.

In order to introduce an energy dissipating model (i.e. an SGS model) there are two very naturally distinctive paths to follow, namely, physical or purely mathematical. The traditional approach in LES to model energy dissipation is based on the physics of turbulent flows. The most common model is the well-known Smagorinsky SGS stress model [49]. This model consists of an eddy (or turbulent) viscosity-based representation of the residual stress in the filtered Navier-Stokes equations. Eddy viscosity-based SGS stress models are analogous to the molecular viscous stress also present in the Navier-Stokes equations. In the latter, molecular viscosity accounts for the effect of molecular dynamics on scales at the continuum level governed by the Navier-Stokes equations. In the former, the eddy viscosity accounts for the effect of unresolved scales on resolved scales, as described earlier.

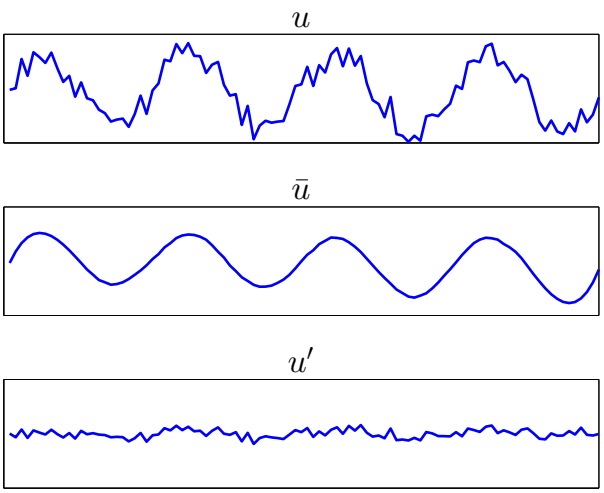

Figure 1.1: Splitting of velocity field ($\mathbf{u}$) into resolved ($\bar{\mathbf{u}}$) and subgrid-scale ($\mathbf{u}'$) components in the RBVMS method. This is analogous to the explicit filtering operation in traditional LES which splits the velocity field into a filtered (resolved) component and a residual component.

Most numerical discretizations implicitly add artificial dissipation in order to provide stability to solutions. As such, a more recent approach in LES is to not introduce the filtering operation bypassing the need for an SGS stress model, but to rather let the numerical dissipation implicit in most discretizations account for the dissipation caused by the unresolved scales. This approach is often referred to as monotone integrated LES or MILES (or alternatively implicit LES) [6, 16].

An example of the implicit LES approach is the residual-based variational multiscale (RBVMS) method introduced in [21] and further developed for the Navier-Stokes equation in [3]. The RBVMS is the method of choice in this research. This method consists of a discretization technique for advection-dominated phenomena such as turbulent flows. This method is purely numerical and is derived from the mathematics of splitting the space of solutions into scales resolvable by the grid and smaller subgrid scales unresolved by the grid (see Figure 1.1), analogous to spatial filtering in traditional LES. This splitting applies to all possible flow regimes and is not unique to turbulence. The splitting generates a discrete equation governing the dynamics of the resolved scales and a continuum equation governing the behavior of the unresolved, subgrid

scales. Solution of the discrete equation yields the resolved velocity and pressure associated with the larger eddies or scales of a turbulent flow. The two equations are coupled, and in particular, the discrete equation governing the larger scales contains a term defined in terms of the SGS velocity and pressure components. This approach calls for solution of the large scale components only via the discrete equation, thus SGS velocity and pressure components are not directly accessible. Instead, mathematical approximations (simplifications) of the continuum equations governing these SGS components are made leading to approximate analytical solutions for the SGS velocities and pressure which are then used to approximate the coupling term appearing in the discrete equation for the large scales. Approximation of the coupling term in the large scale discrete equation is often referred to as an SGS model, and thus is similar in nature to the SGS stress model in traditional, spatial filtering-based LES. However, note that typically the SGS stress model in the latter approach is represented via the Smagorinsky stress model derived directly under the physical assumption of a Kolmogorov energy cascade across the turbulent scales, as described earlier. In the case of the RBVMS method, no such physical considerations are made and the SGS velocity and thus the coupling term in the discrete equation for the large scales are approximated solely based on mathematical considerations.

Studies in [3, 5] have shown the ability of the RBVMS method (with solution variables expressed in terms of non-Uniform rational B-splines (NURBS) basis functions) to accurately capture the largest resolved scales in LES of various turbulent flows. Thus, the RBVMS method behaves as an SGS LES model when used to solve turbulent flows and the methodology will be referred to as RBVMS LES. But beyond this, the method serves as a numerical stabilization technique enabling stable and accurate solutions of advection-dominated processes that could be either laminar or turbulent. It can be shown that the RBVMS method consists of a Galerkin weighted residual

statement plus stabilization terms arising from the multiscale decomposition described previously. It has been well-established that without such stabilization, the Galerkin method yields unstable solutions of advection-dominated processes [8]. These solutions are characterized by parasitic (unphysical) node-to-node oscillations.

To summarize, in LES of turbulent flows, the role of the RBVMS method (i.e. the Galerkin method plus stabilization) is two-fold (1) serving as an SGS LES model in the traditional sense of subgrid-scales draining energy from resolved scales and (2) serving to numerically stabilize the discretization due to the advective nature of all turbulent flows.

Next we discuss yet another key feature in studying analytical and numerical fluid dynamics that is the concept of boundary layer. Prandtl boundary layer theory divides wall-bounded flows into two different regions: the core region (or outer layer) in which viscous effects are insignificant and the area near the wall (or inner layer) in which viscosity plays an important role and should not be neglected. Within the inner layer, velocity vanishes rapidly due to the no-slip condition, thereby inducing a fairly large velocity gradient.

The existence of sharp gradients in very thin layers poses enormous computational difficulty and cost when numerical simulations are performed. According to [41], the number of grid points required to resolve the outer layer is proportional to $Re^{0.5}$ while the number of grid points required to resolve the inner layer is $Re^{2.4}$. To reduce this computational cost, yet another level of modeling is introduced to LES which is referred to as wall modeling [41]. The idea behind wall modeling is to only resolve the core flow and model the inner layer with suitable boundary conditions in what is often referred to as LES with near-wall modeling or LES-NWM. With the lower computation cost brought about with wall models, more realistic problems in terms of computational domain

size and Reynolds number can be solved when compared to those of DNS and LES with resolution of the inner layer (i.e. LES with near-wall resolution or LES-NWR).

1.2 Turbulence in The Coastal Ocean

For this dissertation, RBVMS LES-NWM will be applied to turbulence in the coastal ocean, and in particular to Langmuir turbulence generated by wave-current interaction.

Wind speeds greater than 3 m s^{-1} can lead to the generation of Langmuir turbulence in the upper ocean [58]. Interaction between surface gravity waves and the wind-driven shear current in the upper ocean is well-known to produce Langmuir turbulence characterized by Langmuir circulation or cells consisting of parallel counter-rotating vortices roughly aligned in the direction of the wind (see Figure 1.2). The longest Langmuir cells extend in the downwind direction for tens of meters to kilometers. In the upper ocean mixed layer, the cells can extend to the base of the mixed layer which is tens of meters deep, depending on various factors such as winds, surface waves and surface buoyancy conditions. In shallow coastal shelf regions, Langmuir cells have been observed occupying the full-depth of the water column while serving as an important mechanism for sediment re-suspension [17, 18]. These cells have been observed in water columns ranging from 10 to 30 meters deep. Furthermore, these cells can interact with the tidally-driven and/or wind-driven bottom boundary layer leading to disruption of the classical log-layer dynamics often observed in this region [45, 53].

Wind-wave interaction giving rise to Langmuir circulation is not the only source of turbulence in the ocean. Other sources include destabilizing surface heat fluxes leading to convection-dominated turbulence and surface wave-breaking serving to inject turbulence at the surface. In

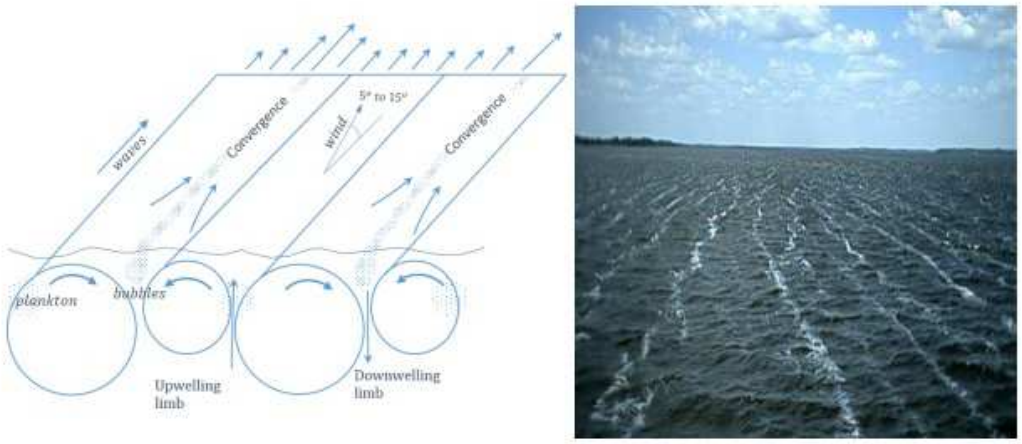

Figure 1.2: (a) Sketch of Langmuir cells and (b) photograph of windrows consisting of foam lined up along the surface convergence zone of the Langmuir cells. Source: [45].

coastal regions, these turbulence regimes often occur embedded within a field of submesoscale and mesoscale eddies characterized by horizontal scales on the order of tens and hundreds of kilometers respectively. In coastal regions, submesoscale eddies resulting from instabilities at river plume density fronts have been identified as an important mechanism for transport from on-shore to off-shore and vice-versa [19]. Furthermore, in idealized simulations characterized by artificially imposed density fronts generating submesoscale eddies [38], Langmuir submesoscales interactions have been shown to be important as Langmuir circulation can counteract the re-stratifying tendency of the submesoscale eddies. In cases when front conditions are not favorable to the generation of submesoscale eddies at a density front, the idealized simulations of [48] (similar to those of [38]) have shown that Langmuir circulation rapidly mixes the front through vertical and horizontal transport induced by the cells.

In [45], it is hypothesized that Langmuir turbulence and associated Langmuir cells may also potentially play an important role in coastal upwelling dynamics in concert with other mechanisms involving stratification, bottom topography and Coriolis forcing effects. The Coriolis effect gives

rise to Ekman transport consisting of surface currents directed at right angles to the direction of the winds in the Northern Hemisphere (and vice-versa in the Southern Hemisphere). In the coastal shelf, along-shore winds can cause Ekman surface transport offshore. As a result, warm surface water flowing away from the coast is replaced by colder bottom water brought by upwelling cross-shore currents. As shown by the two-dimensional simulations in [15], strong mixing of the water column in regions closest to the coast (i.e. the inner shelf region) can limit the cross-shore extent of upwelling currents, forcing these currents to rise and reverse direction farther off-shore (i.e. at distances farther away from the coast). This results in a shut-down of cross-shelf transport of nutrients within the inner shelf, as well-mixed water becomes trapped at the coast. In [45] it is hypothesized that the shut-down mechanism may be enhanced by the intense vertical mixing caused by the action of full-depth Langmuir cells. Furthermore, Langmuir submesoscale interactions developing at the density front established by the upwelling current may also be important.

1.3 Motivation and Objectives

Current regional and coastal circulation models are not able to resolve down to Langmuir turbulence scales due to the need of resolving much larger submesoscale and mesoscale eddies that require computational domains of horizontal size on the order of hundreds of kilometers or greater. Furthermore typical regional and coastal circulation models solve the governing equations under the hydrostatic approximation which is only valid for scales of greater size than the submesoscales [35] and thus not valid for accurately resolving turbulent scales. The importance of Langmuir turbulence in shallow coastal regions as well as the recently uncovered Langmuir submesoscale interactions previously described give rise to the need of developing numerical codes (or solvers)

capable of performing LES that resolves down to the Langmuir turbulence scales and up to the submesoscales while simultaneously being able to handle complex geometry features due to bottom bathymetry and lateral boundaries in coastal regions. Such a code could potentially serve to predict transport in coastal regions including estuaries over relatively short time scales on the order of days and relatively short distances on the order of tens of kilometers, which is often heavily influenced by turbulence and submesoscales. This numerical capability could potentially be a valuable resource for tracking/predicting the path of accidentally spilled materials such as oil products and other pollutants.

Ideally, computational methods for turbulent flow must be able to resolve, or accurately model all the relevant flow scales and their interactions in the presence of complex geometrical configurations. Most current computational approaches for turbulent flows involve efficient techniques that are based on high-order functions (e.g. global polynomial and Fourier (spectral) bases) able to accurately represent the resolved small scale physics in turbulent processes. Such techniques are limited to simple geometry and mesh configurations and periodic boundary conditions. On the other end of the spectrum, much progress has been made over the last several decades on the computation of flows over complex geometrical configurations. These methods, based on low-order functional representations, are able to represent relatively well the gross features of a given turbulent flow, yet they do not possess the high-order accuracy of the aforementioned spectral techniques to predict the more detailed features of the flow. More specifically, these methods are often not able to predict accurately the smallest resolved scales in a computation. Thus, it appears that there is a gap between techniques capable of accurately capturing all resolved scales in turbulent flows on simple geometries and techniques capable of accurately resolving only large scale (gross) features on complex geometries. In order to bridge this gap, a methodology is necessary that simultane-

ously possesses superior approximation and uniform convergence behavior over a wide range of spatial and temporal scales, necessary for capturing flow physics, and the geometrical flexibility, necessary for geophysical applications such as LES of coastal and estuarine flows. The RBVMS method of [21] together with NURBS basis representation of flow variables, recently proposed and tested for turbulence computations in [3], is an excellent candidate for the task and is the method of choice for this research. NURBS are spline basis functions that can be used to approximate the space of solutions to the governing equations and may be used for representation of complex geometry. These basis functions are locally supported, and possess spectral-like approximation properties compared to standard complex-geometry approaches (e.g. low-order finite elements) [22].

In order to develop a code capable of performing RBVMS LES of flows in coastal regions and estuaries, advances in numerous research areas must be made. Next, several of these areas are described.

- *Computing at extreme scales:* Simulations resolving submesoscale eddies as well as the small scale turbulence regimes require horizontal domain lengths on the order of tens of kilometers with grid cell sizes on the order of meters. These resolution needs may be satisfied with meshes consisting of grid points on the order of billions thereby demanding computations at extreme scales. The code used in this research has been written using message passing interface (MPI) protocols enabling parallel computing [60]. Furthermore, meshing strategies suitable for the solver are being developed (e.g. [61]) admitting computations at extreme scales.

- *Open boundary conditions:* Simulations of flows in coastal regions and estuaries require imposition of turbulent flow variables (e.g. velocity, temperature, salinity, etc.) at open boundaries based on data obtained from coastal circulation models. Difficulty with these variables arises from the fact that the circulation models do not resolve the turbulence. Thus, the turbulent component of the prescribed boundary condition has to be calculated synthetically. Research addressing this issue has been presented in [39].

- *Bottom boundary conditions:* Given that the near-wall region in wall-bounded turbulent flows is expensive to resolve, LES simulations are often performed without resolution of this region (as described earlier). LES without resolution of the wall region requires a wall model often consisting of a wall shear stress boundary condition relying on the assumption that the near-wall region is characterized by a well-develop log layer [41]. However, as noted earlier, full-depth Langmuir cells in the coastal ocean have been shown to disrupt bottom log layer dynamics in LES simulations with near-wall resolution [53]. Thus, further research should investigate the suitability of near-wall models for LES simulations of full-depth Langmuir cells. This topic is of focus in this dissertation and will be presented in detail in Chapters 4 and 6. In particular, wall models within the RBVMS LES methodology will be assessed in the presence of full-depth Langmuir cells. Additional developments in wall-modeling with RBVMS LES in general will be presented in Chapter 5.

- *Craik-Leibovich vortex force:* As noted earlier, Langmuir turbulence and associated Langmuir cells are generated by the interaction of the wind-driven shear current with surface gravity waves. In order to avoid resolution of surface gravity waves, the Langmuir turbulence generating mechanism in LES is often represented via the well-known Craik-Leibovich (C-

L) vortex force [11] added to the momentum equation. The C-L vortex force consists of the cross product between Stokes drift velocity induced by surface gravity waves and flow vorticity. In [54], this C-L vortex force has been shown to be of an advective nature, requiring a modification of the RBVMS method (i.e. a modification to the stabilization of the Galerkin method). This topic will be the focus of Chapter 3.

- *Stratification:* Surface buoyancy (surface cooling or surface heating) and or submescoscale eddies among other factors may lead to stratification of the local water column. In particular, stable stratification leads to suppression of turbulence fluctuations [2], and thus a numerical method that can accurately capture this effect is of importance. Stably stratified turbulence has been numerically studied primarily using high order discretization techniques (e.g. see [2]) and the ability of lower order discretizations to accurately represent this turbulence regime remains largely unexplored.

The developments presented in this dissertation constitute an initial attempt towards RBVMS of the coastal ocean. As such, this dissertation focuses on the third and fourth research areas summarized above. Chapter 2 gives a description of the RBVMS method while highlighting the spatial stabilization required for the advection-dominated flows encountered, the time integration scheme and the handling of nonlinearities. Chapter 3 introduces the Craik-Leibovich vortex force augmenting the Navier-Stokes equations and describes the stabilization of this term within the RBVMS framework as originally proposed in [54]. Chapter 3 also presents LES simulations of full-depth Langmuir cells with the RBVMS method using a quadratic NURBS mesh able to resolve the near-wall region (i.e. LES-NWR). Chapter 4 investigates the performance of two near-wall models in LES simulations of full-depth Langmuir cells without resolution of the near-wall region

(i.e. LES-NWM). Chapter 5 extends the use of these near-wall models to RBVMS simulations based on the Reynolds-averaged Navier-Stokes equations in which the Langmuir turbulence is not resolved, but rather parametrized via an eddy viscosity. Chapter 6 revisits RBVMS LES-NWM and proposes a new wall model shown to significantly improve results in simulations of open channel flow. Finally, Chapter 7 presents a summary of important accomplishments and results derived from the research and provides future research directions.

Chapter 2:

Discretization of The Navier-Stokes Equation

In this chapter the spatial and time discretizations of the Navier-Stokes equation used in this research are presented. Spatial discretization consists of the residual-based variational multiscale (RBVMS) method. The RBVMS method together with representation of velocity and pressure variables in terms of, for example, standard finite element-based tri-linear Lagrange shape functions or non-Uniform rational B-splines (NURBS) give rise to a semi-discrete system. Gauss quadrature of weak form spatial integrals associated with the RBVMS method results in a system of first-order, nonlinear ordinary differential equations (ODEs) in time. The coupled ODEs are integrated using the generalized-α method described in [30], which reduces the ODEs to a system of nonlinear algebraic equations, solved via a predictor-multicorrector algorithm. The generalized-α method is a second-order scheme with user control over damping at high frequencies.

The work for this dissertation has been performed using an existing code (solver) implementing the previously summarized solution schemes. Various versions of this code are at the core of research on-going at several institutions. The code dates back to the 1980s when it was initially developed by T.J.R. Hughes and his group at Stanford University for the solution of fluid dynamics problems with stabilized finite elements [9]. Work on this code was continued at Rensselaer Polytechnic Institute (RPI) and more recently at University of Colorado, Boulder by K.E. Jansen and his group, with emphasis on the extension of stabilized finite element methods to computations of turbulent flows [28, 56] and on the development of new unstructured mesh partition schemes to

enable computations at extreme scale [61]. The latter is also the focus of O. Sahni and his group at RPI. The RBVMS method along with NURBS basis for the Navier-Stokes equation were proposed and implemented within this code by Y. Bazilevs, V. Calo, A. Cotrell and T.J.R Hughes at University of Texas, Austin. Work in these areas and extensions to fluid-structure interactions among others has been continued by Y. Bazilevs and his group at University of California, San Diego.

This chapter provides an introduction to the previously described solution techniques in preparation for application of these techniques to wind and wave-driven boundary layer flows in the coastal ocean.

2.1 Spatial Discretization: The RBVMS Method

It is well-known the Galerkin method is unstable for advective-diffusive systems such as the Navier-Stokes equation, yielding solutions characterized by unphysical oscillations when advection is dominant over diffusion. A simple demonstrations in two-dimensions can be found in [8]. In addition to being unstable under dominant advection (over diffusion), the Galerkin method is susceptible to a second instability arising for certain approximation spaces of velocity and pressure that do not satisfy the well-known Babuska-Brezzi condition. Residual-based methods such as a the streamline upwind Petrov/Galerkin (SUPG) method were designed to remedy these spatial instabilities of the Galerkin method via the addition of stabilization terms to the Galerkin residual statement (i.e. the Galerkin weak form). These methods have been shown to damp unphysical oscillations under advection-dominated flow regimes and to allow equal order approximation spaces for velocity and pressure thereby circumventing the Babuska-Brezzi condition. For more details please see [60] and references within. The stabilization terms themselves are residual-based, en-

suring consistency of the formulation. In other words, an exact solution of the Navier-Stokes equations also satisfy the stabilized formulation exactly. Furthermore, these methods have been shown to posses good convergence properties across the full range of advective and diffusive phenomena (e.g. linear finite elements lead to second order accuracy in terms of the L_2 error norm; see [60]).

Although stabilized methods had been in use dating back to the early 80s [8], a general framework for their derivation was not presented until 1995 in [21]. In the variational multiscale framework of [21], solution variables are split into a resolvable component (corresponding to the larger scales) and an unresolved component (corresponding to finer scales). The resolvable scales are those admitted by the discretization (e.g. the approximation solution spaces and the grid) while unresolved scales are those unsupported by the discretization typically of size smaller than the grid cell size, hence these latter scales are often referred to as subgrid scales. The splitting of the solution variables generates a discrete equation governing the dynamics of the resolved component and a continuum equation governing the behavior of the unresolved, subgrid-scale (SGS) component. The two equations are coupled, and in particular, the discrete equation governing the resolved component contains a term defined in terms of the SGS variables. Simplifications of the continuum equation are made leading to approximate analytical solutions for the SGS variables which are then used to approximate the coupling term appearing in the discrete equation for the resolved scales, giving rise to the stabilized method.

At about the same time that the variational multiscale framework was introduced, stabilized methods such as SUPG began to be applied for large-eddy simulation (LES) of turbulent flows (e.g. see [27]). Turbulent flows are characterized by a wide range of spatial and temporal scales. The range of scales increases with increasing Reynolds number, making the resolution of all of the

scales intractable for most flows of interest. In traditional LES, a low-pass, spatial filter is applied to the Navier-Stokes equation in order to filter out scales smaller than the filter width [43]. The resulting filtered equations govern the behavior of the larger more energetic scales (i.e. the large eddies) which (because of their size range) may be resolved with a coarser (less expensive) grid than the full range of scales extending out to the smallest eddies. Filtering generates an extra stress tensor in the filtered Navier-Stokes equation often referred to as the residual stress or the SGS stress. This stress represents the effect of the unresolved scales on the resolved scales which is primarily to drain energy from the resolved scales. The SGS stress is typically modeled or approximated via an eddy viscosity model such as the Smagorinsky model [49]. In [56], it was shown that stabilization techniques such as SUPG serve to drain energy from resolved scales analogous to the SGS stress (modeled, say, with the Smagorinsky model). The fact that the modeled SGS stress and stabilization terms behave similarly suggests a redundancy, and perhaps one of these two sinks may be discarded from the formulation. However, this should not be the case, as will become apparent in the upcoming sub-section.

The spatial filtering operation in traditional LES splits the velocity field ($\mathbf{u}$) into a resolved (filtered) component ($\bar{\mathbf{u}}$) and a residual (SGS) component ($\mathbf{u}'$):

$$\mathbf{u} = \bar{\mathbf{u}} + \mathbf{u}' \tag{2.1}$$

A sketch showing these components for a simple function is shown in Figure (2.1). In [25], the splitting of solution variables in the variational multiscale framework of [21] was re-introduced as an alternative to the spatial filtering operation in classical LES in (2.1). Using this approach, in [3] stabilized methods were re-casted as LES SGS models in what is referred to as residual-based vari-

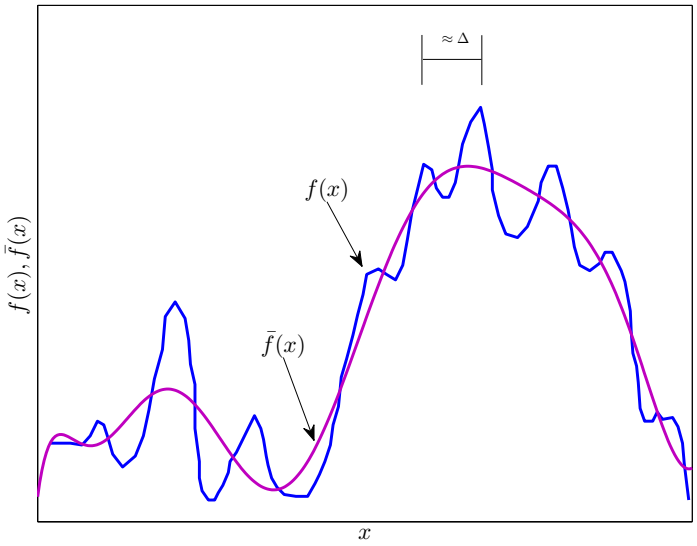

Figure 2.1: Sketch showing the effect of spatial filtering in traditional LES. The filtered function is denoted as $\bar{f}$. Filtering damps scales on the order of the filter width Δ or less. In the variational multiscale framework of [21], decomposition of approximation spaces gives rise to a resolvable component analogous to $\bar{f}$.

ational multiscale (RBVMS) LES. In [3], the RBVMS LES approach was shown to yield accurate solutions of canonical turbulence problems such as turbulent channel flow and forced isotropic turbulence. Furthermore, representation of solution variables (approximation spaces) in terms of non-Uniform rational B-splines (NURBS) within this framework yielded superior approximation of turbulent scales compared to linear finite elements. For example, in simulations of forced isotropic turbulence, the RBVMS method with quadratic and cubic NURBS elements yielded an energy spectrum in closer agreement with the expected (theoretical) spectrum compared to the RBVMS method with linear finite elements. All three simulations had the same number of elements.

2.1.1 Weak Form of The Navier-Stokes Equation

Next, the weak form of the Navier-Stokes equations is presented, in preparation for an introduction to the RBVMS method.

Let $\Omega \in \mathbb{R}^3$ be the problem domain and let Γ denote its boundary. The boundary is expressed as $\Gamma = \Gamma_E \cup \Gamma_N$ where Γ_N is the portion where essential boundary conditions are applied and Γ_N is where natural (Neumann) boundary conditions are applied. The dimensionless Navier-Stokes equation (conservation of momentum) and continuity equation (conservation of mass) for an incompressible fluid may be written as

$$\frac{\partial \mathbf{u}}{\partial t} + \nabla \cdot (\mathbf{u} \otimes \mathbf{u}) + \nabla p - \nabla \cdot (2\nu \nabla^s \mathbf{u}) = \mathbf{f} \text{ in } \Omega \tag{2.2}$$

$$\nabla \cdot \mathbf{u} = 0 \text{ in } \Omega \tag{2.3}$$

where t is time, $\mathbf{u} = (u_1, u_2, u_3)^T$ and p are the fluid velocity and pressure (divided by density), ν is kinematic viscosity, $\nabla^s = \frac{1}{2}\left(\nabla + (\nabla)^T\right)$ is the symmetric spatial gradient of the velocity (with $\nabla = (\partial/\partial x_1, \partial/\partial x_2, \partial/\partial x_3)^T$), and $\mathbf{f}$ is a body force per unit mass. The expression $\mathbf{u} \otimes \mathbf{u}$ is a tensor with entries given by $u_i u_j$.

The first step in deriving the weak form of the flow equations in (6.1) consists of dotting the momentum equation with weighting vector $\mathbf{w}$ and multiplying the continuity equation by weight function q. The two equations are integrated over the problem domain Ω and may be added together for simplicity since the entries of $\mathbf{w}$ (w_1, w_2, w_3) and q are independent of each other. Advection, pressure, viscous stress and continuity equation terms are integrated by parts giving rise to the weak form. Formally, the weak form of the strong form problem in (6.1) can be stated as follows: Let $\mathscr{V}$ denote the solution space for the velocity-pressure pair $\{\mathbf{u}, p\}$ and let $\mathscr{W}$ denote the weighting space for the momentum and continuity weighting functions $\{\mathbf{w}, q\}$. Find $\{\mathbf{u}, p\} \in \mathscr{V}$

such that $\forall\{\mathbf{w},q\} \in \mathscr{W}$,

$$B(\{\mathbf{w},q\},\{\mathbf{u},p\}) + (\mathbf{w}, u_n\mathbf{u} + p\mathbf{n} - 2\nu\nabla^s\mathbf{u}\cdot\mathbf{n})_\Gamma + (q,u_n)_\Gamma = (\mathbf{w},\mathbf{f})_\Omega \tag{2.4}$$

where

$$B(\{\mathbf{w},q\},\{\mathbf{u},p\}) = \left(\mathbf{w}, \frac{\partial\mathbf{u}}{\partial t}\right)_\Omega - (\nabla\mathbf{w}, \mathbf{u}\otimes\mathbf{u})_\Omega - (\nabla\cdot\mathbf{w}, p)_\Omega + (\nabla^s\mathbf{w}, 2\nu\nabla^s\mathbf{u})_\Omega - (\nabla q, \mathbf{u})_\Omega. \tag{2.5}$$

In the above, $(\cdot,\cdot)_A$ denotes the L_2-inner product over A defined as

$$(\mathbf{a},\mathbf{b}) = \int_A \mathbf{a}\cdot\mathbf{b}\, dA. \tag{2.6}$$

Furthermore $u_n = \mathbf{u}\cdot\mathbf{n}$ where $\mathbf{n}$ denotes the outward unit normal vector to the boundary, Γ.

The boundary integrals in (2.4) yield

$$(\mathbf{w}, u_n\mathbf{u} + p\mathbf{n} - 2\nu\nabla^s\mathbf{u}\cdot\mathbf{n})_\Gamma + (q,u_n)_\Gamma = (\mathbf{w}, p\mathbf{n} - 2\nu\nabla^s\mathbf{u}\cdot\mathbf{n})_{\Gamma_N} \tag{2.7}$$

making use of the fact that (1) in flow problems considered here $u_n = 0$ over the entire boundary Γ and (2) the integral over the essential portion of the boundary Γ_E is zero since $\mathbf{w} = 0$ on Γ_E as is traditionally chosen [20]. Finally, the term $\{p\mathbf{n} - 2\nu\nabla^s\mathbf{u}\cdot\mathbf{n}\}_{\Gamma_N}$ appearing in the right hand side of (2.7) corresponds to the known traction on Γ_N.

Making use of (2.7), the weak form in (2.4) can be re-written as

$$B(\{\mathbf{w},q\},\{\mathbf{u},p\}) = (\mathbf{w},\mathbf{f})_\Omega + (\mathbf{w},2\nu\nabla^s\mathbf{u}\cdot\mathbf{n} - p\mathbf{n})_{\Gamma_N}. \tag{2.8}$$

where terms involving known quantities such as the body force $\mathbf{f}$ and the traction on Γ_N appear on the right hand side.

2.1.2 The RBVMS Method for The Weak Form of The Navier-Stokes Equations

In the variational multiscale method of [21], solution and weight spaces are split into resolvable or discrete components (denoted by superscript h) and unresolved or subgrid-scale components (denoted by a prime) via direct summation:

$$\mathscr{V} = \mathscr{V}^h \oplus \mathscr{V}' \quad \text{and} \quad \mathscr{W} = \mathscr{W}^h \oplus \mathscr{W}' \tag{2.9}$$

The resolvable (discrete) components may be spanned, for example, by standard finite element-based tri-linear Lagrangian basis functions or non-Uniform rational B-splines (NURBS); the latter is the method of choice in this research based on the positive results described earlier (e.g. in [3]) and will be presented in some detail in the next chapter. On the other hand, the unresolved, subgrid-scale components are not discrete but rather infinite-dimensional. Given the direct sums in (2.9), the trial solution ($\{\mathbf{u},p\}$ belonging to space $\mathscr{V}$) and weighting functions ($\{\mathbf{w},q\}$ belonging to space $\mathscr{W}$) can be expressed as

$$\mathbf{u} = \mathbf{u}^h + \mathbf{u}' \tag{2.10}$$

$$\mathbf{w} = \mathbf{w}^h + \mathbf{w}' \tag{2.11}$$

$$p = p^h + p' \tag{2.12}$$

$$q = q^h + q' \tag{2.13}$$

Inserting (2.10-2.13) into the left hand side of (2.8) and inserting (2.11) into the right side of (2.8), expanding (while recalling (2.5)) and grouping terms weighted by $\mathbf{w}^h$ and its gradient leads to the following postulation: Let $\mathscr{V}^h$ denote the discrete solution space for the velocity-pressure pair $\{\mathbf{u}^h, p^h\}$ and let $\mathscr{W}^h$ denote the discrete weighting space for the momentum and continuity weighting functions $\{\mathbf{w}^h, q^h\}$. The problem statement now becomes as follows: Find $\{\mathbf{u}^h, p^h\} \in \mathscr{V}^h$ such that $\forall \{\mathbf{w}^h, q^h\} \in \mathscr{W}^h$,

$$B(\{\mathbf{w}^h, q^h\}, \{\mathbf{u}^h, p^h\}) + B_{vms}(\{\mathbf{w}^h, q^h\}, \{\mathbf{u}^h, p^h\}) = (\mathbf{w}^h, \mathbf{f}^h)_\Omega + \left(\mathbf{w}^h, 2\nu\nabla^s\mathbf{u}^h \cdot \mathbf{n} - p^h\mathbf{n}\right)_{\Gamma_N}. \tag{2.14}$$

where the Galerkin terms are

$$\begin{aligned} B(\{\mathbf{w}^h, q^h\}, \{\mathbf{u}^h, p^h\}) = \left(\mathbf{w}^h, \frac{\partial \mathbf{u}^h}{\partial t}\right)_\Omega - \left(\nabla\mathbf{w}^h, \mathbf{u}^h \otimes \mathbf{u}^h\right)_\Omega - (\nabla \cdot \mathbf{w}^h, p^h)_\Omega \\ + \left(\nabla^s\mathbf{w}^h, 2\nu\nabla^s\mathbf{u}^h\right)_\Omega - (\nabla q^h, \mathbf{u}^h)_\Omega. \end{aligned} \tag{2.15}$$

and the terms associated with the variational multiscale (VMS) method are

$$\begin{aligned} B_{vms}(\{\mathbf{w}^h, q^h\}, \{\mathbf{u}^h, p^h\}) = \left(\mathbf{w}^h, \frac{\partial \mathbf{u}'}{\partial t}\right)_\Omega - \left(\nabla\mathbf{w}^h, \mathbf{u}' \otimes \mathbf{u}^h + \mathbf{u}^h \otimes \mathbf{u}' + \mathbf{u}' \otimes \mathbf{u}'\right)_\Omega \\ -(\nabla \cdot \mathbf{w}^h, p')_\Omega + \left(\nabla^s\mathbf{w}^h, 2\nu\nabla^s\mathbf{u}'\right)_\Omega - (\nabla q^h, \mathbf{u}')_\Omega. \end{aligned} \tag{2.16}$$

The pair $\{\mathbf{u}', p'\}$ appearing in (2.16) denotes the velocity and pressure subgrid scales that are too small to be reasonably approximated on a given mesh and will be the topic of discussion next. The term $\left(\nabla \mathbf{w}^h, \mathbf{u}' \otimes \mathbf{u}^h + \mathbf{u}^h \otimes \mathbf{u}'\right)_\Omega$ is referred to as the cross stress and the term $\left(\nabla \mathbf{w}^h, \mathbf{u}' \otimes \mathbf{u}'\right)_\Omega$ is referred to as the Reynolds stress [25].

In order to find an (approximate) expression for the subgrid-scale components $\mathbf{u}'$ and p', a second equation may be obtained by re-inserting (2.10-2.13) into the left hand side of (2.8) and re-inserting (2.11) into the right side of (2.8) and expanding as was done before, but now grouping terms weighted by $\mathbf{w}'$ and its gradient. Note that the resulting equation is not discrete but rather of infinite dimension, thus this equation can be referred to as a continuum equation as was done earlier. The interested reader is directed to [3] for this equation. In [21] analysis of a simpler, but analogous equation for the subgrid-scale velocity arising in a VMS framework application to the steady, linear, advection-diffusion equation lead to an analytical expression for the scalar analog of $\mathbf{u}'$. In [3], this analysis was extended to the more general setting of the Navier-Stokes equation resulting in the following residual-based expressions:

$$\begin{aligned} \mathbf{u}' &= -\tau_M \left(\frac{\partial \mathbf{u}^h}{\partial t} + \mathbf{u}^h \nabla \mathbf{u}^h + \nabla p^h - \nu \Delta \mathbf{u}^h - \mathbf{f}^h \right) \\ p' &= -\tau_C \nabla \cdot \mathbf{u}^h \end{aligned} \tag{2.17}$$

where the residual of the Navier-Stokes equation (with the viscous stress (the term proportional to ν) simplified by making use of the continuity equation) appears in the expression for $\mathbf{u}'$ and the residual of the continuity equation appears in the expression for p'. Furthermore Δ is the Laplacian and τ_M and τ_C are subgrid-scale parameters also known as stabilization parameters to be described further below.

Discarding the Reynolds stress and the time derivative and spatial gradients of $\mathbf{u}'$ in (2.16) and using the expressions in (2.17) to evaluate the cross stress term in (2.16) leads to the SUPG method as used in [56]. Furthermore, the latter simplifications but while approximating the Reynolds stress term via the well-known Smagorinsky eddy viscosity model [49] leads to a method equivalent to the overall method of [56] in which SUPG stabilization is combined with the Smagorinsky model in traditional LES sense (i.e. LES based on spatial filtering as described earlier). Further models of the Reynolds stress based on variations of the Smagorinsky model have been proposed and studied in [25, 29]. In the implementation followed in this research, the cross stress and Reynolds stress terms have all been evaluated using the expression for $\mathbf{u}'$ given in (2.17). This gives rise to what is termed as residual-based variational multiscale (RBVMS) LES, first proposed in [3]. The name "residual-based" follows from the fact that all of the subgrid-scale terms in (2.16) are approximated with the residual-based expressions in (2.17), thereby making the entire formulation residual-based and thus consistent. Consistency refers to the fact that an exact solution pair $\{\mathbf{u}, p\}$ of the Navier-Stokes and continuity equations would also satisfy exactly the RBVMS LES formulation.

In summary, the VMS method, described here for the Navier-Stokes equation, admits two important stress terms: the cross stress and the Reynolds stress. Approximation of the cross stress gives rise to the ingredients required for a stabilized method. Meanwhile, the Reynolds stress consists of a term that may be modeled, for example, proportional to the residual of the Navier-Stokes equation (see (2.17) or in terms of the Smagorinsky SGS stress as it is often done for the spatially filtered Navier-Stokes equation employed in traditional LES. Thus, the VMS method may be considered not only as the progenitor of stabilized methods (noted in [3]), but also as the progenitor of methods resulting from combination of stabilized methods with traditional LES approaches (e.g. see [29]).

The stability parameters τ_M and τ_C (appearing in (2.17)) are chosen based on extensive research of the the stabilized methods community, e.g. see [3, 9, 26, 57]. Parameter τ_M is taken as

$$\tau_M = \left(\frac{C_1}{\Delta t^2} + \mathbf{u}^h \cdot \mathbf{G}\mathbf{u}^h + C_2 G_{ij} G_{ij} \nu^2 \right)^{-\frac{1}{2}}. \tag{2.18}$$

where Δt is time step, and constants C_1 and C_2 may be obtained from convergence analysis of the SUPG method applied to a one-dimensional, advection-diffusion equation with constant advection velocity [60]. The term $\mathbf{G} = [G_{ij}]$ is the metric-tensor of the mapping from the physical domain to the parametric domain of the finite element or NURBS element. The tensor entries are defined as

$$G_{ij} = \frac{\partial \xi_k}{\partial x_i} \frac{\partial \xi_k}{\partial x_j} \tag{2.19}$$

where $\mathbf{x} = (x_1, x_2, x_3)^T$ denotes the coordinates of an element in physical space and $\xi = (\xi_1, \xi_2, \xi_3)^T$ denotes the coordinates of the element in parametric space. Parameter τ_M above may be shown to come from a discrete approximation of $\mathscr{L}_{\text{ad}}^{-1}$ where $\mathscr{L}_{\text{ad}} = \partial/\partial t + \mathbf{u} \cdot \nabla - \nu\Delta$. Alternatively, τ_M may be seen as a generalization of the analogous parameter arising from the analysis of the one-dimensional, steady state, linear advection-diffusion equation with linear finite elements. In the case of the latter equation, an exact stability parameter may be found. This exact stability parameter leads to a nodally exact linear finite element solution [21]. It may be shown (see [13]) that an approximation of the exact stabilization parameter for the one-dimensional, steady state, linear advection-diffusion equation is

$$\tau = \left(C_1 \frac{U^2}{h^2} + C_2 \frac{\kappa^2}{h^2} \right)^{-1/2} \tag{2.20}$$

where U and κ are the constant advecting velocity and diffusivity. Coefficient In the generalized expression in (2.18) metric-tensor $\mathbf{G}$ may be associated with an element length scale; for example, in the case of a cube-shape element with edges of length h, $G_{ij} = (4/h^2)\delta_{ij}$ where δ_{ij} is the Kronecker delta. Furthermore, the terms $\mathbf{u}^h \cdot \mathbf{G}\mathbf{u}^h$ and $G_{ij}G_{ij}\nu^2$ in (2.18) are analogous, and actually reduce to $4U^2/h^2$ and $C_2\kappa^2/h^2$, respectively, in (2.20) for 1D flow.

Stability parameter τ_C is taken as

$$\tau_C = \frac{1}{\tau_M \mathbf{g} \cdot \mathbf{g}} \tag{2.21}$$

where the entries of vector $\mathbf{g}$ are

$$g_i = \sum_{j=1}^{3} \frac{\partial \zeta_j}{\partial x_i} \tag{2.22}$$

As noted in [3], this definition of τ_C arises from a discrete approximation of $\nabla \cdot \mathscr{L}_{\text{ad}}^{-1} \nabla$, where $\mathscr{L}_{\text{ad}}$ was defined earlier above.

To recapitulate, the RBVMS LES approach followed here is: Find $\{\mathbf{u}^h, p^h\} \in \mathscr{V}^h$ such that $\forall \{\mathbf{w}^h, q^h\} \in \mathscr{W}^h$,

$$B(\{\mathbf{w}^h, q^h\}, \{\mathbf{u}^h, p^h\}) + B_{vms}(\{\mathbf{w}^h, q^h\}, \{\mathbf{u}^h, p^h\}) = (\mathbf{w}, \mathbf{f})_\Omega + \left(\mathbf{w}^h, 2\nu\nabla^s\mathbf{u}^h \cdot \mathbf{n} - p^h\mathbf{n}\right)_{\Gamma_N}. \tag{2.23}$$

where the Galerkin terms are

$$\begin{aligned} B(\{\mathbf{w}^h, q^h\}, \{\mathbf{u}^h, p^h\}) = \left(\mathbf{w}^h, \frac{\partial \mathbf{u}^h}{\partial t}\right)_\Omega - \left(\nabla\mathbf{w}^h, \mathbf{u}^h \otimes \mathbf{u}^h\right)_\Omega - (\nabla \cdot \mathbf{w}^h, p^h)_\Omega \\ + \left(\nabla^s\mathbf{w}^h, 2\nu\nabla^s\mathbf{u}^h\right)_\Omega - (\nabla q^h, \mathbf{u}^h)_\Omega. \end{aligned} \tag{2.24}$$

and the simplified VMS terms are

$$B_{vms}(\{\mathbf{w}^h,q^h\},\{\mathbf{u}^h,p^h\}) = -\left(\nabla\mathbf{w}^h,\mathbf{u}'\otimes\mathbf{u}^h+\mathbf{u}^h\otimes\mathbf{u}'+\mathbf{u}'\otimes\mathbf{u}'\right)_\Omega \\ -(\nabla\cdot\mathbf{w}^h,p')_\Omega-(\nabla q^h,\mathbf{u}')_\Omega. \tag{2.25}$$

with all subgrid-scale terms defined through (2.17), (2.18) and (2.21). For simplicity when working with the time discretization in the upcoming section, let (2.23) be re-expressed as

$$\tilde{B}(\{\mathbf{w}^h,q^h\},\{\mathbf{u}^h,p^h\}) = \tilde{L}(\{\mathbf{w}^h,q^h\},\{\mathbf{u}^h,p^h\}) \tag{2.26}$$

2.2 Time Discretization: The Generalized-α Method

Time discretization is accomplished via the generalized-α method introduced for the first time for the Navier-Stokes equation in [30]. As noted earlier, this method is second-order accurate while providing user control over damping at high frequencies.

Expanding the weighting functions and solution variables in (2.24-2.25) in terms of basis N_A (where this could be a Lagrangian basis or NURBS basis, for example) with $A = 1,...n_b$ and n_b being the number of basis functions,

$$\phi = \sum_{A=1}^{n_b} \phi_A(t) N_A(\mathbf{x}), \tag{2.27}$$

the RBVMS method leads to a set of non-linear ordinary differential equations (ODEs) which may be expressed in residual form as

$$\mathbf{R}(\mathbf{V},\dot{\mathbf{V}},\mathbf{P}) = \mathbf{0} \tag{2.28}$$

In the previous expression, $\mathbf{V}$, $\dot{\mathbf{V}}$ and $\mathbf{P}$ denote vectors of nodal (in the case of Lagrangian basis) or control point (in the case of NURBS) degrees of freedom of velocity, acceleration, and pressure, respectively (e.g. the ϕ_A's in (2.27)). Note that in the generalized-α method, acceleration is viewed as independent. The system in (2.28) may be re-expressed as

$$\begin{pmatrix} \mathbf{R}^M \\ \mathbf{R}^C \end{pmatrix} = \begin{pmatrix} \mathbf{0} \\ \mathbf{0} \end{pmatrix} \tag{2.29}$$

where the momentum residual $\mathbf{R}^M$ corresponds to the portions of $\mathbf{R}$ in (2.28) multiplying $\mathbf{w}^h$ and its gradient and the continuity residual $\mathbf{R}^C$ corresponds to the portions of $\mathbf{R}$ multiplying the gradient of q^h. The entries of $\mathbf{R}^M$ may be obtained from

$$\begin{gathered} \mathbf{R}^M = [R^M_{A,i}] \quad \text{with} \\ R^M_{A,i} = \tilde{B}(\{N_A\mathbf{e}_i, 0\}, \{\mathbf{u}^h, p^h\}) - \tilde{L}(\{N_A\mathbf{e}_i, 0\}, \{\mathbf{u}^h, p^h\}) \end{gathered} \tag{2.30}$$

for $A = 1 \cdots n_b$ and $i = 1,2,3$, where $\mathbf{e}_1 = (1,0,0)^T$ $\mathbf{e}_2 = (0,1,0)^T$ and $\mathbf{e}_3 = (0,0,1)^T$. The $\tilde{B}$ and $\tilde{L}$ operators were defined in (2.26). Similarly, the entries of $\mathbf{R}^C$ may be obtained from

$$\begin{gathered} \mathbf{R}^C = [R^C_A] \quad \text{with} \\ R^C_A = \tilde{B}(\{\mathbf{0}, N_A\}, \{\mathbf{u}^h, p^h\}) - \tilde{L}(\{\mathbf{0}, N_A\}, \{\mathbf{u}^h, p^h\}) \end{gathered} \tag{2.31}$$

Applying the generalized-α method to solve the non-linear ODE system in (2.29) leads to the following set of equations

$$\mathbf{R}^M(\dot{\mathbf{V}}_{n+\alpha_m}, \mathbf{V}_{n+\alpha_f}, \mathbf{P}_{n+1}) = 0 \tag{2.32}$$

$$\mathbf{R}^C(\dot{\mathbf{V}}_{n+\alpha_m}, \mathbf{V}_{n+\alpha_f}, \mathbf{P}_{n+1}) = 0 \tag{2.33}$$

$$\dot{\mathbf{V}}_{n+\alpha_m} = \dot{\mathbf{V}}_n + \alpha_m(\dot{\mathbf{V}}_{n+1} - \dot{\mathbf{V}}_n) \tag{2.34}$$

$$\mathbf{V}_{n+\alpha_f} = \mathbf{V}_n + \alpha_f(\mathbf{V}_{n+1} - \mathbf{V}_n) \tag{2.35}$$

$$\mathbf{V}_{n+1} = \mathbf{V}_n + \Delta t\dot{\mathbf{V}}_n + \gamma\Delta t(\dot{\mathbf{V}}_{n+1} - \dot{\mathbf{V}}_n) \tag{2.36}$$

to solve for $\dot{\mathbf{V}}_{n+1}$, $\mathbf{V}_{n+1}$, $\dot{\mathbf{V}}_{n+\alpha_m}$, $\mathbf{V}_{n+\alpha_f}$ and $\mathbf{P}_{n+1}$, given vectors $\dot{\mathbf{V}}_n$ and $\mathbf{V}_n$ In these equations $\Delta t = t_{n+1} - t_n$ is the time step size and $t_{n+\alpha_f}$ and $t_{n+\alpha_m}$ are intermediate times between t_n and t_{n+1}. Parameters α_m, α_f and γ control the accuracy and stability of the method. Second-order accuracy is obtained setting

$$\gamma = 1/2 + \alpha_m - \alpha_f \tag{2.37}$$

and unconditional stability is obtained if

$$\alpha_m \geq \alpha_f \geq 1/2. \tag{2.38}$$

A one-parameter family of schemes possessing second-order accuracy and unconditional stability (i.e. satisfying the two previous relations) is obtained by setting

$$\alpha_m = \frac{1}{2}\left(\frac{3-\rho_\infty}{1+\rho_\infty}\right) \quad \text{and} \quad \alpha_f = \frac{1}{1+\rho_\infty} \tag{2.39}$$

where parameter ρ_∞ controls damping at high frequencies [30, 60]. As noted in [30], setting ρ_∞ to 1 preserves all frequencies of the usual linear test problem $\dot{y} = \lambda y$. On the other end of the spectrum, setting $\rho_\infty = 0$ leads to annihilation of the highest frequency in one time step.

Application of the generalized-α method to the spatially discrete RBVMS formulation for momentum and continuity equations led to the system of algebraic equations in (2.32-2.36). Equations (2.32) and (2.33) are non-linear, thus solution of the system requires an iterative solution technique, taken here as Newton's method. Incorporation of Newton's method gives rise to a predictor-multicorrector scheme.

The predictor stage of the predictor-multicorrector scheme sets

$$\mathbf{V}_{n+1,(0)} = \mathbf{V}_n \tag{2.40}$$

$$\dot{\mathbf{V}}_{n+1,(0)} = \frac{(\gamma-1)}{\gamma}\dot{\mathbf{V}}_n \tag{2.41}$$

$$\mathbf{P}_{n+1,(0)} = \mathbf{P}_n \tag{2.42}$$

where the subscript 0 refers to the fact that this is an initial estimate of the solution required to begin the iterative (multi-corrector) stage.

The multi-corrector stage consists of iterations (denoted by subscript i) through the following steps:

1. Evaluate acceleration and velocity at intermediate time steps ($t_{n+\alpha_m}$, $t_{n+\alpha_f}$) and pressure at t_{n+1} as

$$\dot{\mathbf{V}}_{n+\alpha_m,(i)} = \dot{\mathbf{V}}_n + \alpha_m(\dot{\mathbf{V}}_{n+1,(i-1)} - \dot{\mathbf{V}}_n) \tag{2.43}$$

$$\mathbf{V}_{n+\alpha_f,(i)} = \mathbf{V}_n + \alpha_f(\mathbf{V}_{n+1,(i-1)} - \mathbf{V}_n) \tag{2.44}$$

$$P_{n+1,(i)} = P_{n+1,(i-1)} \tag{2.45}$$

2. Insert the previous expressions in the residuals in (2.32) and (2.33) and solve the following corresponding linear systems admitted by Newton's method:

$$\mathbf{K}_{(i)}\Delta\dot{\mathbf{V}}_{n+1,(i)} + \mathbf{G}_{(i)}\Delta\mathbf{P}_{n+1,(i)} = -\mathbf{R}^{M}_{(i)} \tag{2.46}$$

$$\mathbf{D}_{(i)}\Delta\dot{\mathbf{V}}_{n+1,(i)} + \mathbf{L}_{(i)}\Delta\mathbf{P}_{n+1,(i)} = -\mathbf{R}^{C}_{(i)} \tag{2.47}$$

3. Solving the previous linear system leads to the following updates:

$$\dot{\mathbf{V}}_{n+1,(i)} = \dot{\mathbf{V}}_{n+1,(i-1)} + \Delta\dot{\mathbf{V}}_{n+1,(i)} \tag{2.48}$$

$$\mathbf{V}_{n+1,(i)} = \mathbf{V}_{n+1,(i-1)} + \gamma\Delta t\Delta\dot{\mathbf{V}}_{n+1,(i)} \tag{2.49}$$

$$\mathbf{P}_{n+1,(i)} = \mathbf{P}_{n+1,(i-1)} + \Delta\mathbf{P}_{n+1,(i)} \tag{2.50}$$

The tangent matrices in (2.46)-(2.47) arising from Newton's method are as follows:

$$\mathbf{K}_{(i)} = \frac{\partial\mathbf{R}^{M}_{(i)}(\dot{\mathbf{V}}_{n+\alpha_m,(i)}, \mathbf{V}_{n+\alpha_f,(i)}, \mathbf{P}_{n+1,(i-1)})}{\partial\dot{\mathbf{V}}_{n+1,(i)}} \tag{2.51}$$

$$\mathbf{G}_{(i)} = \frac{\partial\mathbf{R}^{M}_{(i)}(\dot{\mathbf{V}}_{n+\alpha_m,(i)}, \mathbf{V}_{n+\alpha_f,(i)}, \mathbf{P}_{n+1,(i-1)})}{\partial\mathbf{P}_{n+1,(i)}} \tag{2.52}$$

$$\mathbf{D}_{(i)} = \frac{\partial\mathbf{R}^{C}_{(i)}(\dot{\mathbf{V}}_{n+\alpha_m,(i)}, \mathbf{V}_{n+\alpha_f,(i)}, \mathbf{P}_{n+1,(i-1)})}{\partial\dot{\mathbf{V}}_{n+1,(i)}} \tag{2.53}$$

$$\mathbf{L}_{(i)} = \frac{\partial\mathbf{R}^{C}_{(i)}(\dot{\mathbf{V}}_{n+\alpha_m,(i)}, \mathbf{V}_{n+\alpha_f,(i)}, \mathbf{P}_{n+1,(i-1)})}{\partial\mathbf{P}_{n+1,(i)}} \tag{2.54}$$

Expressions for the entries of these matrices in terms of the basis function N_A can be found in [3].

2.3 Summary

This chapter summarized the discretization approaches for the governing fluid flow equations (Navier-Stokes and continuity equations) used in this research. Spatial discretization consists in the RBVMS method which serves to stabilize the formulation under advection-dominated phenomena such as turbulent flow regimes. Furthermore, the RBVMS method serves to provide energy dissipation of the resolved scales in the sense of traditional LES-based subgrid-scale modeling. Time discretization consists of the generalized-α method providing a family of second-order accurate, unconditionally stable schemes with user-controlled damping of high-frequency content. Spatial and time discretizations of weak form of the governing equations results in a set of nonlinear algebraic equations which are handled via Newton's method. The combination of the generalized-α method and the Newton's method results in a predictor-multicorrector algorithm.

In the upcoming chapter, a term will be added to the momentum equation in order to represent surface wave-current interaction giving rise to Langmuir turbulence, a typical turbulence regime occurring in the upper ocean. The added term can be shown to be of advective nature, thereby requiring modification of the RBVMS method and associated stability parameters described above.

Chapter 3:

RBVMS LES of Shallow Water Langmuir Turbulence

All the figures here were regenerated are different from those in that paper. Surface wave effects play an important role in determining surface boundary fluxes of momentum, energy and scalars and ultimately vertical mixing [14]. Wave-current interaction is among several flow phenomena generating turbulence in the upper ocean; others include wind- and tidal-driven shear, buoyancy-driven convection and wave breaking. Wind speeds greater than 3 m s^{-1} often lead to wave-current interaction sufficiently strong to generate Langmuir circulation (LC), consisting of pairs of parallel counter-rotating vortices (or cells) oriented approximately in the downwind direction, as shown in the sketch in Figure 1.2a in Chapter 1. The cells are characteristic of the turbulence (i.e. the Langmuir turbulence) advected by the mean flow. As with all turbulence, Langmuir turbulence encompasses a range of spatial and temporal scales. Amongst the larger spatial scales are those of the cells which extend in the downwind direction for tens of meters to kilometers and are separated by distances on the order of meters [58].

The surface convergence of each cell generates a downwelling region characterized by negative vertical velocity fluctuations while the bottom divergence generates an upwelling region characterized by positive vertical velocity fluctuations, leading to increased levels of vertical mixing. Bubbles, particulate matter and flotsam accumulate along the surface convergence of the cells forming what are often referred to as "windrows" as seen in Figure 1.2b. Surface convergences of

the cells are characterized by intensification of positive downwind velocity fluctuations leading to an enhanced mean current as seen in Figure 1.2a.

Historically, Langmuir cells have been measured within the upper ocean surface mixed layer in deep water far above the bottom of the water column. However, these cells have also been known to occur in shallower water masses such as in inner shelf coastal regions, estuaries and lakes. For example, [18] reported detailed acoustic Doppler current profiler (ADCP) measurements of Langmuir cells engulfing the entire water column lasting as long as 18 hours in a shallow water region off the coast of New Jersey. Measurements were made at Rutgers University's LEO15 cabled observatory in 15 m depth water. The observed full-depth cells were denoted as Langmuir supercells or LSC because of their important contribution towards transport of sediment and bio-active material on shallow shelves. The strong coherence of LSC makes them more effective than classical bottom boundary layer turbulence at moving material out of the low-speed layer near bottom and into the strong and strongly directional downwind mean flow associated with these events. In [18], it was suggested that transport in such supercell events dominates net annual transport of sediment at LEO15.

Originally described by Langmuir [31], LC is now generally accepted to be the result of wave-current interaction or, more specifically, the interaction between the wind-driven shear current and the Stokes drift velocity induced by surface gravity waves [11]. A model for the generation of LC was first proposed by Craik and Leibovich [11]. It consists of a vortex force (the Craik-Leibovich force or C-L force) in the momentum equation representing the interaction between the Stokes drift velocity and the vertical shear of the wind-driven current; specifically, the C-L vortex force is the vector cross product between the Stokes drift velocity and the vorticity of the flow. Main parameter

ingredients in this force are the dominant wavelength and amplitude of the surface waves used to define the Stokes drift velocity profile.

The C-L force arises from low-pass time filtering or wave-phase averaging of the Navier-Stokes equation in order to filter out the high frequency surface waves. Hereafter, the time filtered Navier-Stokes equation with the C-L force will be referred to as the C-L equation. Inclusion of the C-L force in the momentum equation greatly reduces the computational complexity as it eliminates the need to resolve the surface waves giving rise to LC. Instead, the top of the flow domain is simply taken to be bounded by a flat (non-deforming) surface denoting the mean water height. Note that the C-L framework does not account for the impact of wave-breaking on the turbulence resolved. Sullivan and McWilliams [51] have incorporated a stochastic model of wave breaking into the C-L equation in their LES of Langmuir circulations within the upper ocean mixed layer. Such a model is beyond the scope of the present work.

The C-L equation has enabled a number of successful LES describing the vertical and horizontal structure of upper ocean Langmuir turbulence in statistical equilibrium, e.g. [34, 36, 46]. However, note that most of these simulations have been made using spectral numerical methods. The interested reader is directed to the review [50] for further references. As described in the Introduction chapter, the main goal of this dissertation is to initiate the development of a more flexible code or solver that is able to accurately capture the turbulence scales, while affording future capability to represent complex geometry features associated with coastal/estuarine boundaries and bathymetries that can not be resolved by the spectral codes traditionally used for LES of Langmuir turbulence. The solver and LES methodology described in Chapter 2 present an ideal setting to accomplish this goal.

Solution of the Navier-Stokes equation augmented with the C-L vortex force is non-trivial as the latter term is an advective term giving rise to instabilities requiring stabilization of the type presented in the previous chapter. Note that the C-L vortex force has been previously identified in [46] and [55] as giving rise to instabilities by triggering scales of size smaller than the grid (i.e. subgrid-scales). The aim of this chapter is to present the extension of advection stabilization within the RBVMS formulation of the previous chapter to consistently account for the advective nature of the C-L vortex force. This extension was originally developed in [54]. Results from simulations of full-depth Langmuir cells with the RBVMS methodology will be presented showing good convergence properties and good agreement with field measurements of [17, 18].

3.1 The Navier-Stokes Equation with C-L Vortex Forcing: The Craik-Leibovich Equation

Let $\Omega \in \mathbb{R}^3$ be the problem domain and let Γ denote its boundary as in Chapter 2. Recall that the boundary is expressed as $\Gamma = \Gamma_E \cup \Gamma_N$ where Γ_N is the portion where essential boundary conditions are applied and Γ_N is where natural boundary conditions are applied.

The Craik-Leibovich momentum equation and the continuity equation are given as follows:

$$\frac{\partial \mathbf{u}}{\partial t} + \nabla \cdot (\mathbf{u} \otimes \mathbf{u}) + \nabla p - \nabla \cdot (2\nu \nabla^s \mathbf{u}) - \boldsymbol{\phi} \times \nabla \times \mathbf{u} = \mathbf{f} \text{ in } \Omega \tag{3.1}$$

$$\nabla \cdot \mathbf{u} = 0 \text{ in } \Omega \tag{3.2}$$

where all variables are as before (recall Chapter 2) and $\boldsymbol{\phi} = (\phi_1, \phi_2, \phi_2)^T$ is the known Stokes drift velocity vector induced by surface gravity waves (to be defined in more detail further below). The last term on the left-hand-side of Eq. (6.1) represents C-L forcing. Because the term depends on the first-order derivatives of the velocity field, it has the mathematical structure of advection. With

this in mind, the C-L momentum equation is written as

$$\frac{\partial \mathbf{u}}{\partial t} + \nabla \cdot (\mathbf{u} \otimes \mathbf{u}) + \nabla p - \nabla \cdot (2\nu \nabla^s \mathbf{u}) + \tilde{\mathbf{A}}_i \frac{\partial \mathbf{u}}{\partial x_i} = \mathbf{f} \text{ in } \Omega \tag{3.3}$$

where $\tilde{\mathbf{A}}_i$'s are

$$\tilde{\mathbf{A}}_1 = \begin{pmatrix} 0 & -\phi_2 & -\phi_3 \\ 0 & \phi_1 & 0 \\ 0 & 0 & \phi_1 \end{pmatrix} \tag{3.4}$$

$$\tilde{\mathbf{A}}_2 = \begin{pmatrix} \phi_2 & 0 & 0 \\ -\phi_1 & 0 & -\phi_3 \\ 0 & 0 & \phi_2 \end{pmatrix} \tag{3.5}$$

$$\tilde{\mathbf{A}}_3 = \begin{pmatrix} \phi_3 & 0 & 0 \\ 0 & \phi_3 & 0 \\ -\phi_1 & -\phi_2 & 0 \end{pmatrix}, \tag{3.6}$$

and summation on the repeated index i is employed. In the following section the RBVMS method is applied to the above partial differential equations.

3.2 The RBVMS Formulation of The Craik-Leibovich Equation

The RBVMS formulation of the C-L momentum equation is a straight-forward extension of the RBVMS formulation for the incompressible Navier-Stokes equation (given in Chapter 2) that also accounts for the presence of the C-L forcing terms.

Following the splitting of the approximation spaces into resolvable (discrete) and subgrid components introduced in Chapter 2, let $\mathscr{V}^h$ denote the discrete solution space for the velocity-pressure pair $\{u^h, p^h\}$ and let $\mathscr{W}^h$ denote the discrete weighting space for the linear momentum and continuity weighting functions $\{w^h, q^h\}$. The space-discrete problem is stated as: Find $\{\mathbf{u}^h, p^h\} \in \mathscr{V}^h$ such that $\forall \{w^h, q^h\} \in \mathscr{W}^h$,

$$B(\{\mathbf{w}^h, q^h\}, \{\mathbf{u}^h, p^h\}) + B_{vms}(\{\mathbf{w}^h, q^h\}, \{\mathbf{u}^h, p^h\}) = (\mathbf{w}^h, \mathbf{f}^h)_\Omega + \left(\mathbf{w}^h, 2\nu\nabla^s\mathbf{u}^h \cdot \mathbf{n} - p^h\mathbf{n}\right)_{\Gamma_N}. \tag{3.7}$$

where the boundary term (i.e. the integral over Γ_N) has been developed in Chapter 2. The Galerkin and VMS terms follow similar those in (2.24) and (2.25), respectively, each with an extra term due to the C-L vortex force:

$$\begin{aligned} B(\{\mathbf{w}^h, q^h\}, \{\mathbf{u}^h, p^h\}) \;=\; & \left(\mathbf{w}^h, \frac{\partial \mathbf{u}^h}{\partial t}\right)_\Omega - \left(\nabla \mathbf{w}^h, \mathbf{u}^h \otimes \mathbf{u}^h\right)_\Omega - (\nabla \cdot \mathbf{w}^h, p^h)_\Omega \\ & + \left(\nabla^s \mathbf{w}^h, 2\nu\nabla^s \mathbf{u}^h\right)_\Omega + \left(\mathbf{w}^h, \tilde{\mathbf{A}}_i \frac{\partial \mathbf{u}^h}{\partial x_i}\right)_\Omega - (\nabla q^h, \mathbf{u}^h)_\Omega. \end{aligned} \tag{3.8}$$

$$\begin{aligned} B_{vms}(\{\mathbf{w}^h, q^h\}, \{\mathbf{u}^h, p^h\}) \;=\; & -\left(\nabla \mathbf{w}^h, \mathbf{u}' \otimes \mathbf{u}^h + \mathbf{u}^h \otimes \mathbf{u}' + \mathbf{u}' \otimes \mathbf{u}'\right)_\Omega \\ & -(\nabla \cdot \mathbf{w}^h, p')_\Omega - \left(\tilde{\mathbf{A}}_i^T \frac{\partial \mathbf{w}^h}{\partial x_i}, \mathbf{u}'\right) - (\nabla q^h, \mathbf{u}')_\Omega. \end{aligned} \tag{3.9}$$

Analogously to (6.6), the subgrid scales are modeled as

$$\begin{aligned} \mathbf{u}' &= -\tau_M \left(\frac{\partial \mathbf{u}^h}{\partial t} + \mathbf{u}^h \nabla \mathbf{u}^h + \nabla p - \nu \Delta \mathbf{u}^h + \tilde{\mathbf{A}}_i \frac{\partial \mathbf{u}^h}{\partial x_i} - \mathbf{f}\right) \\ p' &= -\tau_C \nabla \cdot \mathbf{u}^h \end{aligned} \tag{3.10}$$

To define the subgrid-scale parameters for the C-L equations, the momentum equations are written in the form of a generalized advective-diffusive system as

$$\frac{\partial \mathbf{u}}{\partial t} + \mathbf{A}_i \frac{\partial \mathbf{u}}{\partial x_i} - \nu \Delta \mathbf{u} = f - \nabla p \quad \text{in } \Omega, \tag{3.11}$$

where $\mathbf{A}_i = (u_i \mathbf{I} + \tilde{\mathbf{A}}_i)$ (with $\mathbf{I}$ being the identity matrix) are the advective flux jacobians given by

$$\mathbf{A}_1 = \begin{pmatrix} u_1 & -\phi_2 & -\phi_3 \\ 0 & u_1 + \phi_1 & 0 \\ 0 & 0 & u_1 + \phi_1 \end{pmatrix} \tag{3.12}$$

$$\mathbf{A}_2 = \begin{pmatrix} u_2 + \phi_2 & 0 & 0 \\ -\phi_1 & u_2 & -\phi_3 \\ 0 & 0 & u_2 + \phi_2 \end{pmatrix} \tag{3.13}$$

$$\mathbf{A}_3 = \begin{pmatrix} u_3 + \phi_3 & 0 & 0 \\ 0 & u_3 + \phi_3 & 0 \\ -\phi_1 & -\phi_2 & u_3 \end{pmatrix}. \tag{3.14}$$

with $\mathbf{u} = (u_1, u_2, u_3)^T$. The C-L forcing contributions render these jacobians non-diagonal and non-symmetric, which requires an appropriate definition of the subgrid-scale parameters. Based on the developments in [23, 24, 44] for generalized advective-diffusive systems, parameter τ_M may be computed in matrix form as follows:

$$\tau_M = \left(\frac{4}{\Delta t^2} \mathbf{I} + G_{ij} \mathbf{A}_i \mathbf{A}_j + C_I G_{ij} G_{ij} \nu^2 \mathbf{I} \right)^{-\frac{1}{2}}. \tag{3.15}$$

where G_{ij} is the metric-tensor of the mapping from the physical domain to the parametric domain of the finite element or NURBS element, defined in Eq. (2.19) of Chapter 2.

The new definition of τ_M in (3.15) requires the computation of the matrix square root inverse. This is done using the Denman-Beavers algorithm [12], which computes the matrix square root inverse in an iterative fashion. The algorithm is started by setting $\mathbf{X}_0 = \tau_M^{-2}$ and $\mathbf{Y}_0 = \mathbf{I}$, and the iteration consists of the following updates:

$$\begin{aligned} \mathbf{X}_{k+1} &= \tfrac{1}{2}\left(\mathbf{X}_k + \mathbf{Y}_k^{-1}\right) \\ \mathbf{Y}_{k+1} &= \tfrac{1}{2}\left(\mathbf{Y}_k + \mathbf{X}_k^{-1}\right), \end{aligned} \tag{3.16}$$

where k is the iteration index. In a small number of iterations (3 to 5) $\mathbf{Y}$ converges to τ_M defined by Eq. (3.15).

Finally, given τ_M, τ_C is computed as

$$\tau_C = \left(G_{ij}\tau_{Mij}\right)^{-1}, \tag{3.17}$$

which is a generalization of the relationship given in Chapter 2, Eq. (2.21). Note that τ_{Mij} are the entries of matrix τ_M.

3.3 Computational Setup

The computational domain, depicted in Figure 6.1, is a rectangular box with dimensions $4\pi\delta \times \frac{8}{3}\pi \times 2\delta$ in the stream-wise or downwind (x_1), span-wise or crosswind (x_2) and wall-normal or vertical (x_3), directions, respectively. The velocity vector corresponding to this domain is $\mathbf{u}^h =$

$(u_1^h, u_2^h, u_3^h)^T$ where u_1^h, u_2^h and u_3^h are velocity components in the stream-wise (downwind), span-wise (crosswind) and wall-normal (vertical) directions, respectively. The half-depth of the domain (in the x_3-direction) is δ. The flow is driven by a wind stress in the x_1 direction applied at the top surface ($x_3 = \delta$), generating a shear flow as depicted via the velocity vectors in Figure 6.1. At the top surface, a no-penetration boundary condition is also assumed to hold. No-slip conditions are applied at the bottom wall boundary ($x_3^d = -\delta$). In the stream-wise and span-wise directions periodic boundary conditions are employed in order to represent an unbounded domain in these directions, representative of an inner continental shelf shear flow unaffected by coastal boundaries nor meso and subemsoscale eddies. In this case, the flow and associated turbulence is in direct response to local wind and surface wave forcing conditions.

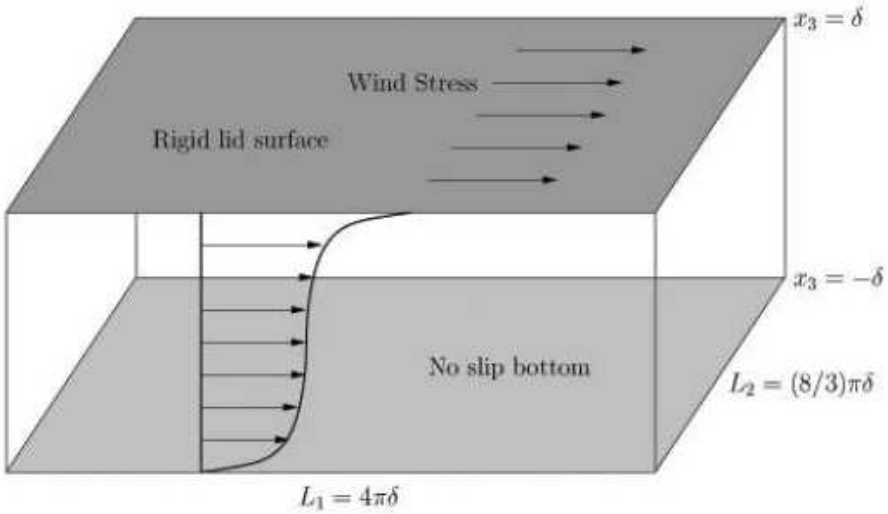

Figure 3.1: The sketch of a wind driven channel flow used as the computational domain in the numerical simulations.

The Stokes drift velocity is taken to be aligned with the wind and defined as

$$\phi = u_s \begin{pmatrix} \frac{\cosh(2\kappa x_3)}{2\sinh(2\kappa\delta)} \\ 0 \\ 0 \end{pmatrix} \qquad x_3 \in [-\delta, \delta] \tag{3.18}$$

with $u_s = \omega\kappa a^2$, where ω is the dominant frequency, $\kappa = 2\pi/\gamma$ is the dominant wavenumber and γ is the dominant wavelength of surface gravity waves generating Langmuir circulation (see [33, 40] for details).

Characteristic flow velocity, length and pressure scales are taken as wind stress friction velocity u_τ, water column half-depth δ, and $P = \rho u_\tau^2$ (with ρ being density), respectively. Characteristic time scale is taken as δ/u_τ. Using these scales to non-dimensionalize the C-L equation gives rise to the Reynolds number defined as $Re = u_\tau\delta/\nu$ (where ν is kinematic viscosity) and the turbulent Langmuir number defined as $La_t = \sqrt{u_\tau/u_s}$. The turbulent Langmuir number is inversely proportional to wave forcing relative to wind forcing.

The flow is driven purely by a wind stress, thus the body force, $\mathbf{f}$ in Eq. (6.1) is $\mathbf{0}$. Furthermore, imposition of the wind stress in the x_1 while setting $u_3^d = 0$ at the surface (i.e. the no-penetration condition) results in the following natural or Neumann condition which in dimensional terms is given as

$$\nu\left(\frac{\partial u_1}{\partial x_3} + \frac{\partial u_3}{\partial x_1}\right)_{x_3=\delta} = u_\tau^2 \quad \text{and} \quad \nu\left(\frac{\partial u_2}{\partial x_3} + \frac{\partial u_3}{\partial x_2}\right)_{x_3=\delta} = 0 \tag{3.19}$$

Noting that $\partial u_3/\partial x_1 = \partial u_3/\partial x_1 = 0$ at the surface ($x_3 = \delta$) since $u_3 = 0$ there (no-penetration), and non-dimensionalizing with characteristic velocity and length scales (u_τ and δ) leads to

$$\nu \left(\frac{\partial u_1}{\partial x_3} \right)_{x_3=\delta} = u_\tau^2 \quad \text{and} \quad \left(\frac{\partial u_2}{\partial x_3} \right)_{x_3=\delta} = 0 \tag{3.20}$$

The previous conditions allow for the boundary integral in (3.7) to be re-expressed as

$$\begin{aligned} \left(\mathbf{w}^h, 2\nu \nabla^s \mathbf{u}^h \cdot \mathbf{n} - p^h \mathbf{n} \right)_{\Gamma_N} &\equiv \int_{\Gamma_N} w_1^h \nu \frac{\partial u_1^h}{\partial x_3} d\Gamma_N + \int_{\Gamma_N} w_2^h \nu \frac{\partial u_2^h}{\partial x_3} d\Gamma_N \\ &\quad + \int_{\Gamma_N} w_3^h \left(\nu \frac{\partial u_3^h}{\partial x_3} - p^h \right) d\Gamma_N \\ &= \int_{\Gamma_N} w_1^h u_\tau^2 \, d\Gamma_N \end{aligned} \tag{3.21}$$

where Γ_N corresponds to the top surface of the domain in Figure 6.1 (i.e. $x_3 = \delta$), $\mathbf{n} = (0,0,1)^T$ is the unit outward normal to Γ, $\mathbf{u}^h = (u_1^h, u_2^h, u_3^h)^T$ and $\mathbf{w}^h = (w_1^h, w_2^h, w_3^h)^T$. In the simplification of (3.21) the following have been used: $\nu \partial u_1^h/\partial x_3 = u_\tau^2$ on Γ_N and $w_3^h = 0$ on Γ_N since $u_3^h = 0$ there.

For the computations presented here, $Re = 395$, $La_t = 0.7$, and $\lambda = 12\delta$. The latter two wind/wave forcing parameter values are characteristic of the wind and wave forcing conditions during the field measurements of shallow water, full-depth Langmuir circulation of Gargett and Wells [17]. Their measurements were made in a 15 meters-deep water column on the coastal shelf off southern New Jersey with surface waves characterized by an 8 second period, a 1 meter amplitude and wind stress at 0.1 N/m^2.

Quadratic NURBS (non-Uniform rational B-splines) basis functions that are C^1-continuous across mesh knots are employed in the computations (see [22] for definition of knots and review of NURBS). That is the velocity, pressure and corresponding and weight functions are expanded

in terms of quadratic NURBS basis. For example, in one dimension this expansion takes the form

$$f^h = \sum_{A=1}^{n_b} f_A N_A(x) \tag{3.22}$$

where N_A is the basis function and n_b is the number of basis functions. In multiple dimensions the basis are constructed using tensor products [22]. An example of an 8-element uniform mesh showing the quadratic basis functions in one-dimension is shown in Figure 3.2. Note that in general this basis is not interpolatory, unlike standard linear finite elements basis. However, the first an last basis functions at then ends of a domain can be constructed such that they are interpolatory at these boundaries, thereby facilitating imposition of essential or Dirichlet boundary conditions. The interested reader is directed to [22] for details on this and Figure 3.3 further below for an example of a graded, 8-element mesh containing interpolatory basis functions at the ends of the domain.

Simulations using a sequence of h-refined quadratic NURBS meshes were performed to ensure convergence of the computational results. The coarsest mesh is comprised of $24 \times 24 \times 24$ NURBS elements, while the finest mesh has $64 \times 64 \times 64$ NURBS elements. In general, for NURBS of order p and maximal continuity $p-1$, the number of basis functions in each tensor-product direction equals to $n+p$, where n is the number of elements in this direction. (For periodic boundary conditions, the number of basis functions is n, which is independent of the polynomial order.) This is in contrast to the C^0-continuous finite elements of order p, where the number of basis functions is $pn+1$ (or pn in the periodic case).

The mesh is uniform in the periodic directions. The elements in the wall-normal (vertical) direction are stretched or graded toward the top and bottom boundaries in order to resolve surface and bottom boundary layers (see an example of this in Figure 3.3). The mesh knots are placed

according to

$$z_i = -1 + b^{-1} \tanh\left(\left(\frac{2i}{N_3+1} - 1\right) \tanh^{-1}(b)\right) \qquad i \in [1, N_3+1], \tag{3.23}$$

where z is equivalent to x_3, $b = 0.973$ is used and N_3 corresponds to the number of elements in x_3.

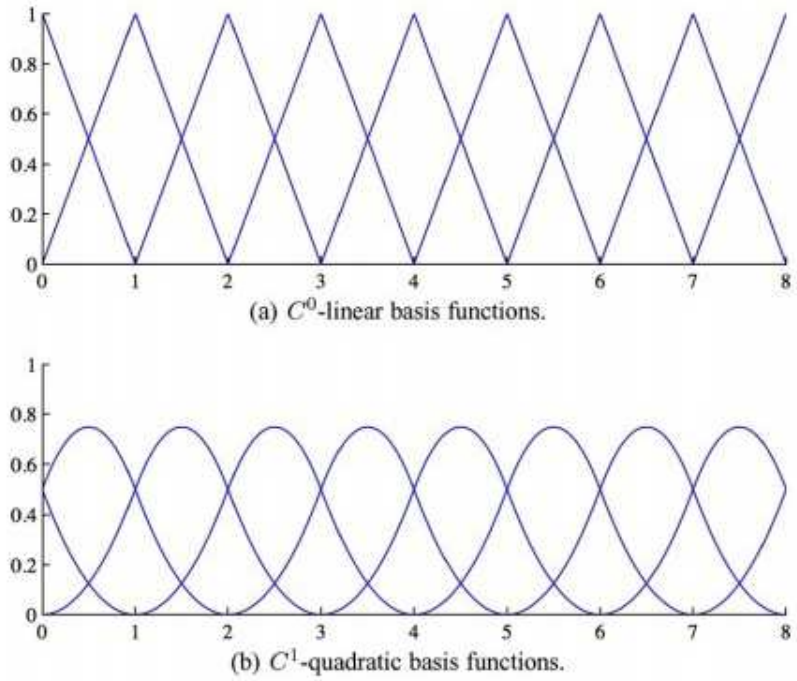

Figure 3.2: One-dimensional (a) linear basis functions (used in standard finite element analysis) and (b) quadratic basis functions for an 8-element periodic mesh. Source: [3].

The flow is advanced in time using the generalized-α method via the predictor multi-corrector algorithm described in Chapter 2. Details of the mesh and time step sizes may be found in Table 4.1. Time steps satisfy the well-known CFL condition. Meshes are stretched near the surface and near the bottom so as to resolve sharp boundary layers in these regions. The last column of Table 4.1 shows z_1^+ for each mesh, which is the size of the first element in the wall-normal direction in

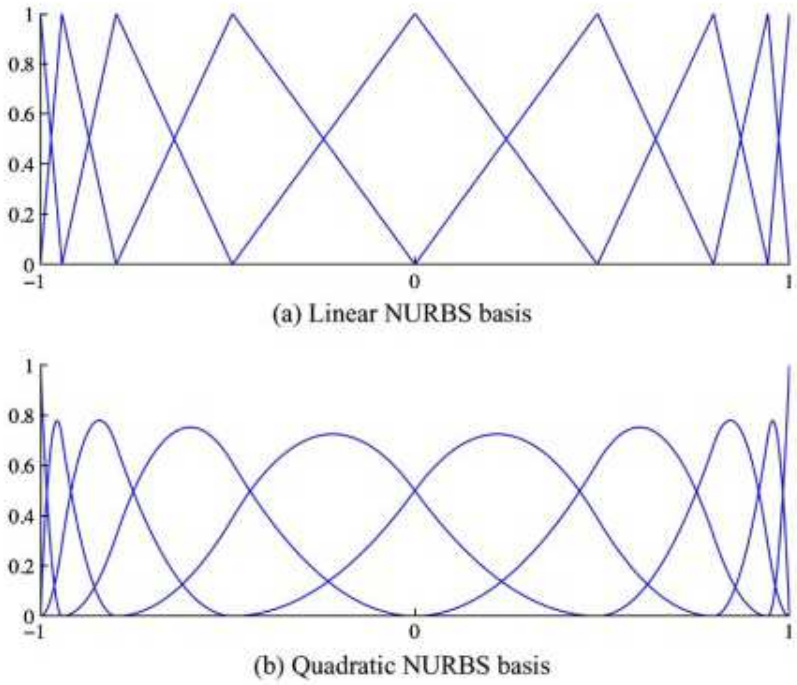

Figure 3.3: One-dimensional (a) standard linear finite elements basis functions and (b) quadratic NURBS basis functions for an 8-element mesh refined near the ends to better resolve boundary layers. This refinement is similar to the wall-normal discretization used in the RBVMS LES computations of wind-driven flow presented in this Chapter. Note that here the first and last quadratic NURBS basis are interpolatory facilitating imposition of the essential (no-slip) bottom boundary condition. Source: [3].

non-dimensional wall units ($z_1^+ = u_\tau \Delta x_3^d / \nu$). For all meshes z_1^+ is less than 7, indicating that the first element adjacent to the wall is within the viscous sublayer [43], thereby ensuring resolution of the sharp gradients expected within this region.

3.4 Numerical Results

In the following sub-sections results from LES of wind-driven flow with and without Langmuir circulation (LC) are presented. Statistics of the flow are presented under statistical equilibrium characterized by steady state mean flow variables. The simulation with LC was initialized

Table 3.1: Summary of mesh and time step sizes used in the simulations. In the table, N_1, N_2, and N_3 are the number of basis functions used in the simulation in each tensor product direction and N_{tot} is their total number. z_1^+ is the size of the first element in the wall-normal direction in non-dimensional wall units ($z_1^+ = u_\tau \Delta z/\nu$). Time step size Δt has been made dimensionless with characteristic time scale given as δ/u_τ.

N_1	N_2	N_3	N_{tot}	z_1^+	Δt
24	24	26	14976	4.62	0.025
32	32	34	34816	3.31	0.0188
48	48	50	115200	2.11	0.0125
64	64	66	270336	1.55	0.00935

by “turning on" the C-L vortex force in the simulation without LC after the latter had achieved statistical equilibrium.

3.4.1 Flow Structures

Flow structures are presented in terms of velocity fluctuations calculated from the classical Reynolds decomposition:

$$u_i^h = \left\langle u_i^h \right\rangle + u_i^{h\prime}, \tag{3.24}$$

where brackets denote averaging over downwind (x_1) and crosswind (x_2) directions and over time, and the superscript prime denotes the resolved turbulence fluctuation. Time averages have been collected over sufficiently long times periods such that mean flow variables (e.g. $\left\langle u_i^h \right\rangle$) are time-independent, indicative of statistical equilibrium. Note that the prime notation used here to define the resolved turbulence velocity fluctuation is different from the prime notation in Eqs. (2.16) and (6.6) used to define unresolved (subgrid) scales. Henceforth the superscript h is dropped from the resolved quantities for simplicity.

Figure 3.4 shows an instantaneous three-dimensional snapshot of iso-contours of vertical velocity fluctuations, u_3', in the wind-driven flow with LC. Vertical velocity fluctuations are characterized

by full-depth negative and positive downwind elongated regions, corresponding to the full-depth downwelling and upwelling limbs of the Langmuir cells sketched in Figure 1.2 in Chapter 1. Figure 3.5 shows an instantaneous snapshot of downwind velocity fluctuations on the horizontal plane at mid-depth of the domain ($x_3 = 0$ in Fig. 6.1) in wind-driven flows with and without LC. In both flows, downwind velocity fluctuation is characterized by downwind elongated streaks alternating in sign in the crosswind direction. Animations (not shown) reveal that the vortex force causes the positive streaks in the flow without LC to merge together leading to a single pair of streaks (positive and negative). The crosswind extent of the resulting positive streak is greater than the negative streak.

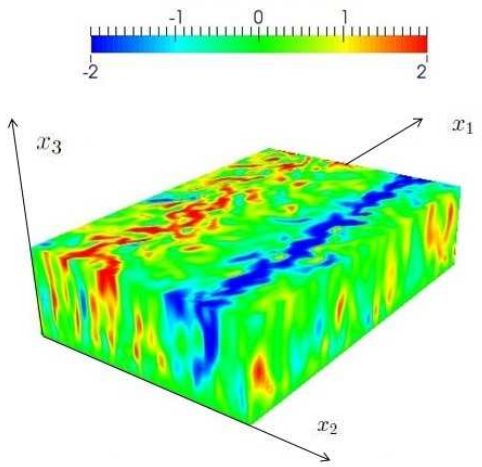

Figure 3.4: Instantaneous snapshot of iso-contours of wall-normal (vertical) velocity fluctuations in flow with LC on the $64 \times 64 \times 66$ quadratic NURBS mesh described earlier.

In order to reveal the crosswind-vertical structure of the previously described downwind elongated streaks, we perform the following triple decomposition of the computed velocity:

$$u_i = \langle u_i \rangle + \underbrace{\langle u_i' \rangle_{tx} + u_i''}_{=u_i'} \tag{3.25}$$

where $\langle\cdot\rangle_{tx}$ denotes averaging in time and over the downwind (x_1) direction and the instantaneous velocity fluctuation is obtained via the classical Reynolds decomposition in (3.24). The middle term on the right hand side of Eq. (3.25) is defined as a partially averaged fluctuation:

$$v_i'(x_2,x_3) \equiv \langle u_i' \rangle_{tx}. \tag{3.26}$$

This partially averaged velocity fluctuation emphasizes coherent, secondary flow structures in the downwind direction such as the downwind elongated streaks observed in Figure 3.5. Figures 3.6 and 3.7 show the crosswind-vertical structure of the partially averaged velocity fluctuation in the flows with and without LC, respectively. Overall, both cases exhibit positive and negative crosswind cell structures in each of the partially averaged fluctuating velocity components; the flow with LC has a spanwise one-cell structure while the flow without LC has a less coherent spanwise two-cell structure.

The one-cell structure in the flow with C-L forcing (Figure 3.6) is nearly identical to that obtained with a spectral LES in [52] with the same wind and wave forcing parameters described earlier. Recall that these parameters in the C-L vortex force have been chosen as $La_t = 0.7$ and $\gamma = 12\delta$ following the field measurements of [17]. Additionally, the one-cell structure in the flow with C-L forcing possesses all of the basic characteristics of full-depth Langmuir circulation expected based on the field measurements in [17]. Experimental data in [17] shows that the spanwise (crosswind) length of one Langmuir cell is in the range of 6δ and 12δ. Accordingly, our computation has predicted the generation of only one Langmuir cell as expected, given the crosswind extent chosen for the domain (see length L_2 in Figure 6.1).

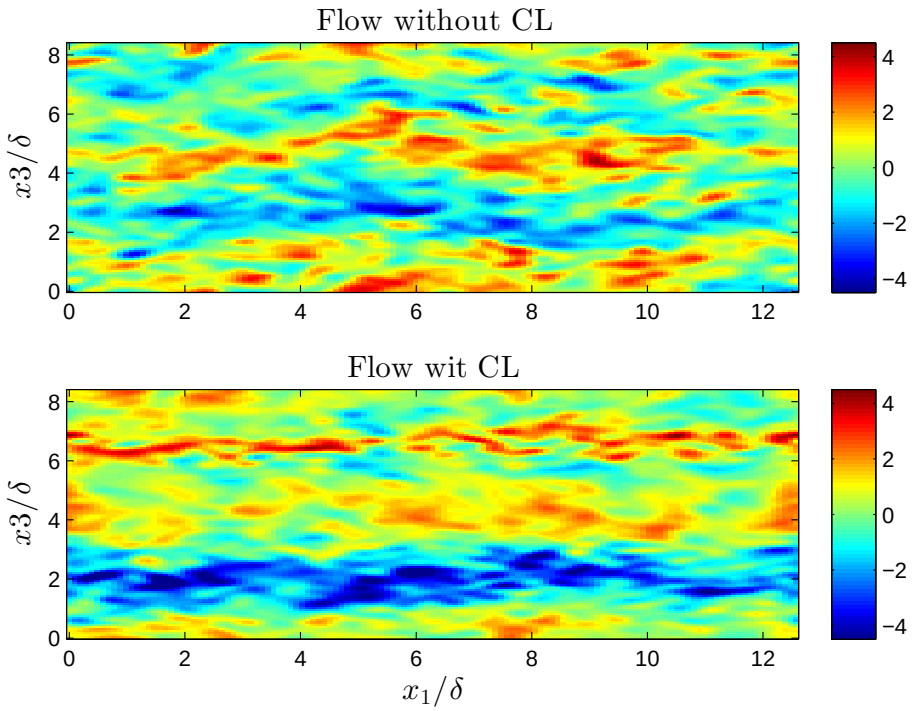

Figure 3.5: Color maps of instantaneous downwind velocity fluctuation u_1' on the downwind-crosswind plane at mid-depth in flows with and without C-L vortex forcing (i.e. with and without LC). Results are from the simulations on the $48 \times 48 \times 50$ quadratic NURBS mesh described earlier.

As seen in Figure 3.6, a change in sign of surface intensified v_2' (panel b) generates the surface convergence of the cell, which in turns leads to the downwelling limb of the cell. The downwelling limb is the full-depth region characterized by negative v_3' in panel c. This region is depicted in the sketch shown in Figure 1.2. Furthermore, the upwelling limb (region with positive v_3') of the cell is larger in crosswind extent than the downwelling region (region with negative v_3') in agreement with the field measurement of full-depth LC in [17]. At mid depth the upwelling limb is approximately 1.6 larger than the downwelling limb, which is close to the 1.4 factor measured in the field. The downwelling limb coincides with a region of bottom- and surface-intensified positive v_1' (panel a). Note that this region of full-depth positive v_1' leads to an enhanced downwind current as depicted in Figure 1.2. The enhancement of the downwind current within the Langmuir

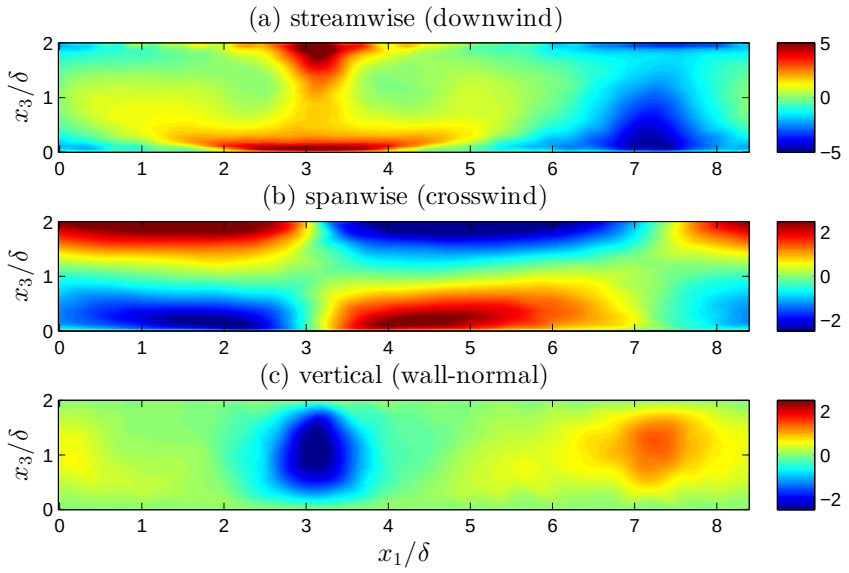

Figure 3.6: Crosswind-vertical variation of velocity fluctuations v_i' (defined in Eq. (3.26) in flow with LC. Results are from the simulation on the $48 \times 48 \times 50$ quadratic NURBS mesh.Streamwise (downwind) direction (x_1) is out of page.

cell downwelling region is by a factor of approximately $10u_\tau$ near the surface and near the bottom of the water column. Finally, the one-cell structure in the flow with C-L vortex forcing (Figure 3.6) is significantly different in structure and magnitude of fluctuations from the two-cell structure obtained in the flow without C-L vortex forcing (Figure 3.7).

In Figure 3.8, the instantaneous velocity fluctuations in the flow with LC have been made dimensional with the wind stress friction velocity reported by Gargett and Wells in [17] during their field observations of full-depth Langmuir cells. Magnitudes of these fluctuations in the LES are in close agreement with those measured in the field (shown in Figure 3.9) as well as with those computed using the spectral method of Tejada-Martínez et al. [52, 55]. In both, computations and field experiments, instantaneous streamwise and spanwise velocity fluctuations are in the ± 8 cm/s range and the vertical velocity fluctuation is in the ± 4 cm/s range. Note that the field measurements in [17] were made using a bottom-mounted, upward-facing acoustic Doppler current

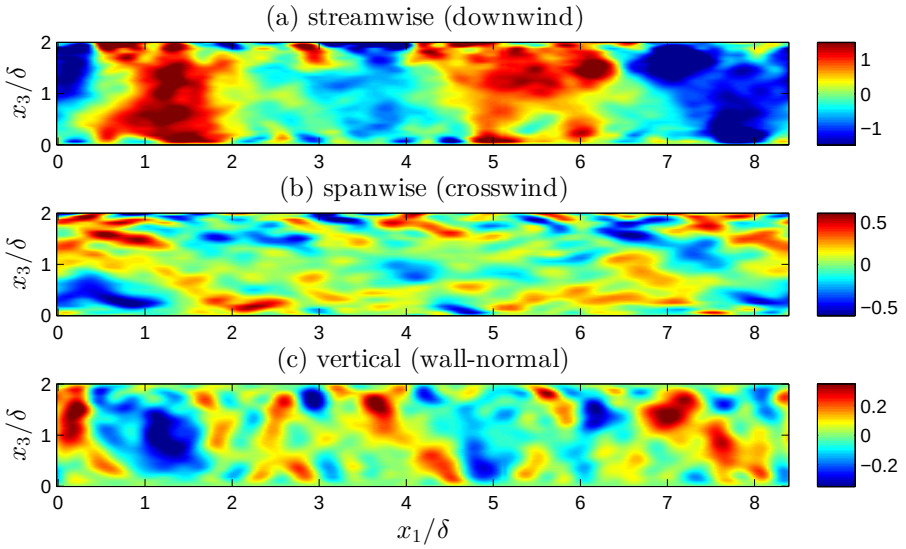

Figure 3.7: Crosswind-vertical variation of partially averaged velocity fluctuations v_i' (defined in Eq. 3.26) in flow without LC. Results are from the simulation on the $48 \times 48 \times 50$ quadratic NURBS mesh.

profiler (ADCP) in a 15-meter deep water column off the southern New Jersey coast undergoing strong wind and wave forcing. Mean wind stress was 0.1 N/m^2 and mean wave height was 1 m. The ADCP was not able to make a reliable measurement of the uppermost 15 percent of the water column. Furthermore, the computations do not take into account the effect of wave breaking at the surface. Thus comparison between field measurements and the LES should not include the near-surface region. Comparison of panels b in Figures 3.8 and 3.9 shows that the LES is able to resolve the near-bottom intensification of the full-depth region of positive downwind velocity fluctuations measured in the field. Furthermore, in Figure 3.9 note that the region of downwelling (panel c) coincides with a region of positive downwind velocity fluctuations (panel a), which as described earlier is also the case in the LES (see Figures 3.6 and 3.8).

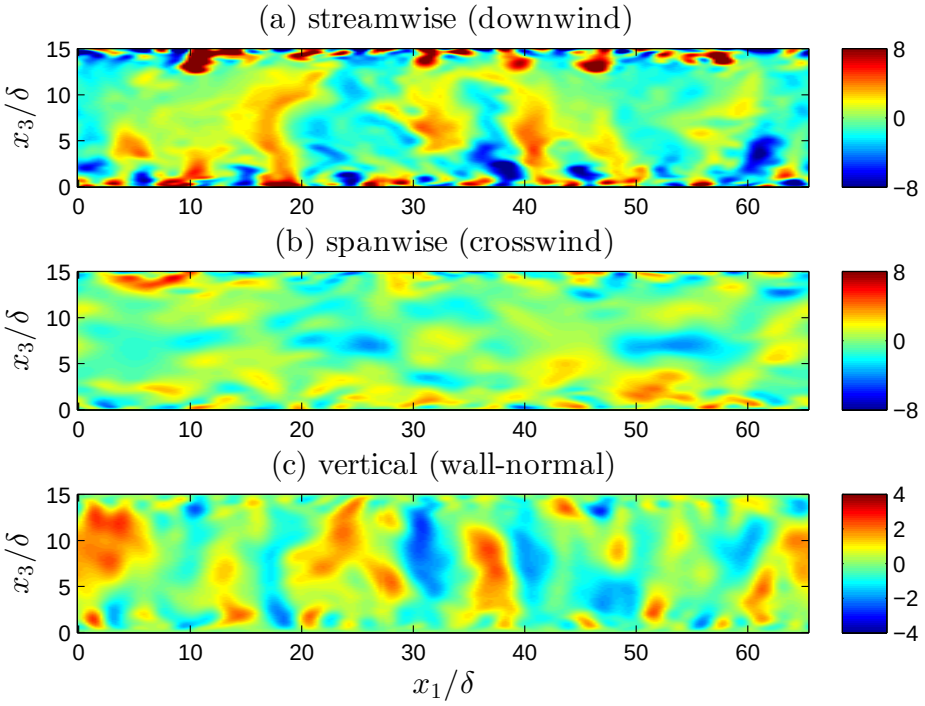

Figure 3.8: Crosswind-vertical variation of velocity instantaneous velocity fluctuations u_i' (in cm/s). Results are from the simulation on the $48 \times 48 \times 50$ quadratic NURBS mesh. Computational velocities have been made dimensional with wind stress friction velocity recorded in the field during episodes of full-depth LC [17]. Field measurements were made in a 15-meters deep water column under a wind stress of 0.1 N/m^2.

In conclusion, predictions from the LES with C-L vortex forcing compare favorably with field measurements in [17] in spite of the low Reynolds number of the computation ($Re = 395$) compared to the Reynolds number of the observations ($Re \approx 50,000$).

3.4.2 Mesh Convergence

Convergence studies on quadratic NURBS meshes in terms of mean downwind velocity and turbulent kinetic energy (TKE) for flow with full-depth LC are presented. Mean velocity, TKE, budgets of TKE and budgets of TKE components for this flow and the corresponding flow without LC have been analyzed in detail in [52]. Here the focus is strictly on mesh convergence. Details

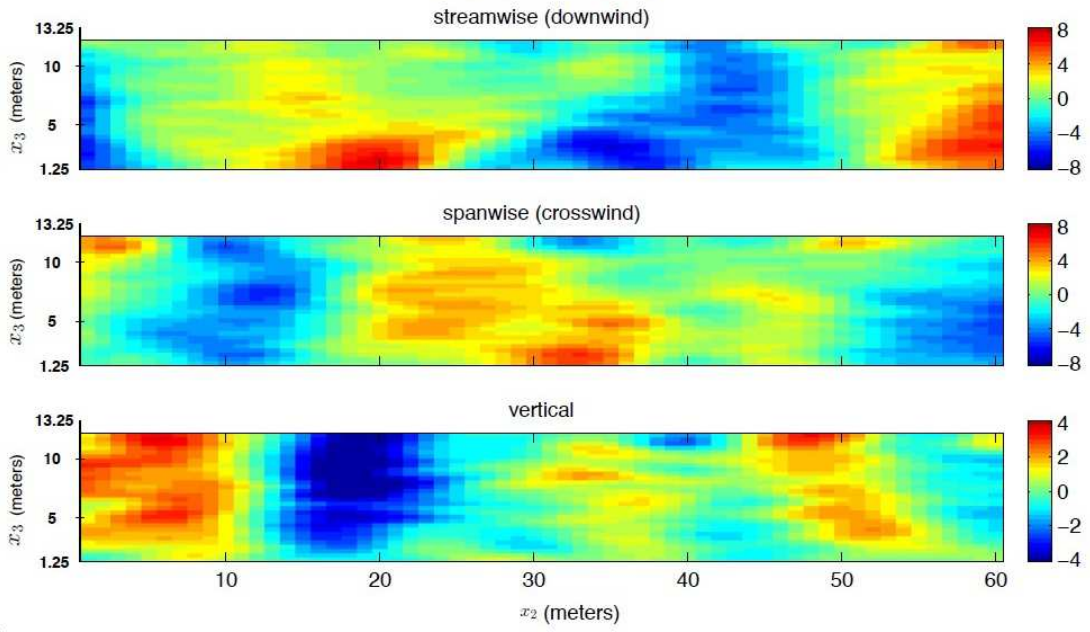

Figure 3.9: Crosswind-vertical variation of velocity instantaneous velocity fluctuations u_i' (in cm/s) during episode of full-depth Langmuir cells measured during field experiments of Gargett and Wells [17] using a bottom-mounted, upward-facing acoustic Doppler current profiler (ADCP). Field measurements were made in a 15 meters-deep water column under a wind stress of 0.1 N/m^2. This figure is courtesy of Ann Gargett.

of the meshes considered are given in Table 4.1. Recall that for the coarsest mesh of $24 \times 24 \times 26$ basis functions, the first wall-normal mesh knot is at a distance $z_1^+ = u_\tau \Delta y/\nu = 4.62$. For the the finest mesh of $64 \times 64 \times 66$ basis functions, $z_1^+ = 1.55$. Thus all meshes considered are able to resolve the near-wall viscous sublayer.

Mean downwind velocity is expressed as $\langle u_1 \rangle$, recalling that brackets denote averaging over time and downwind and crosswind directions. TKE is defined in terms of velocity fluctuations as $\text{TKE} = \langle u_1' u_1' + u_2' u_2' + u_3' u_3' \rangle / 2$, where velocity fluctuations are again obtained via the classical Reynolds decomposition: $\mathbf{u} = \langle \mathbf{u} \rangle + \mathbf{u}'$.

Results are not compared with those obtained with other codes because no direct numerical simulation (DNS) of this test case exists that may be used as a benchmark solution. Figure 3.10

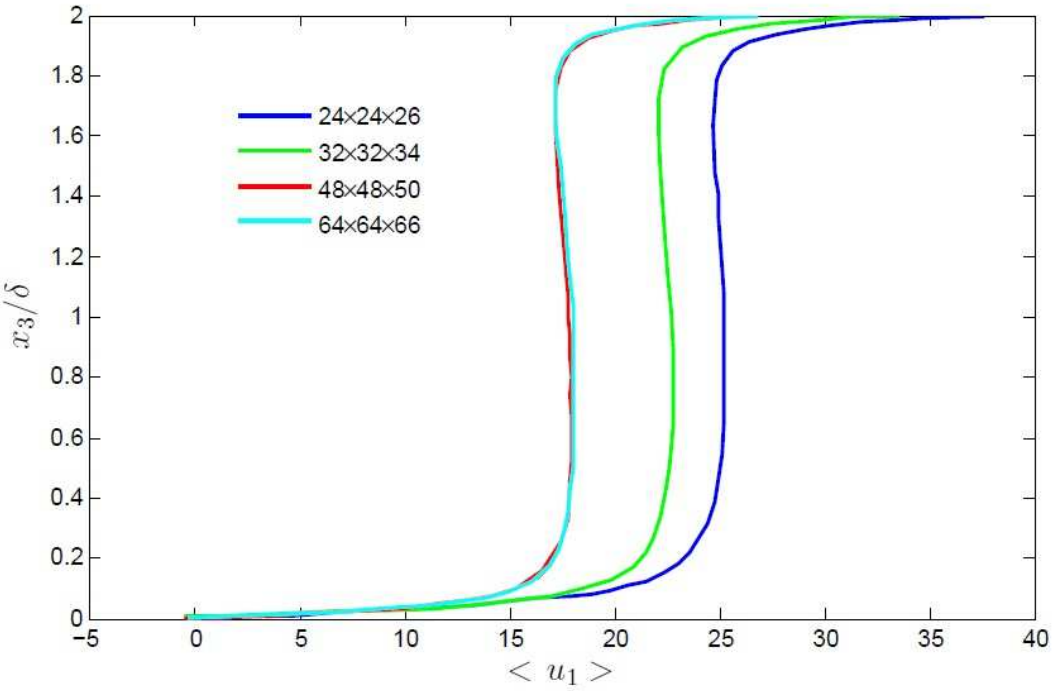

Figure 3.10: Convergence of mean downwind velocity in flow with LC. Quadratic NURBS meshes were used for all cases.

shows convergence of the mean velocity profile. The $24 \times 24 \times 26$ mesh gives a significant over-prediction of the mean flow. The results improve for the $32 \times 32 \times 34$ mesh. Further improvement is seen for the $48 \times 48 \times 50$ mesh. The $64 \times 64 \times 66$ mesh yields a nearly indistinguishable mean velocity profile from the $48 \times 48 \times 50$ case. A similar convergence pattern is observed for the TKE in Figure 3.11, however, very small differences between the $48 \times 48 \times 50$ and the $64 \times 64 \times 66$ cases are visible in the figure.

3.4.3 Disruption of The Log Layer

Figures 3.12 and 3.13 provide a comparison between the flow with LC and the same flow without LC in terms of mean velocity in order to highlight the effects induced by LC. The action

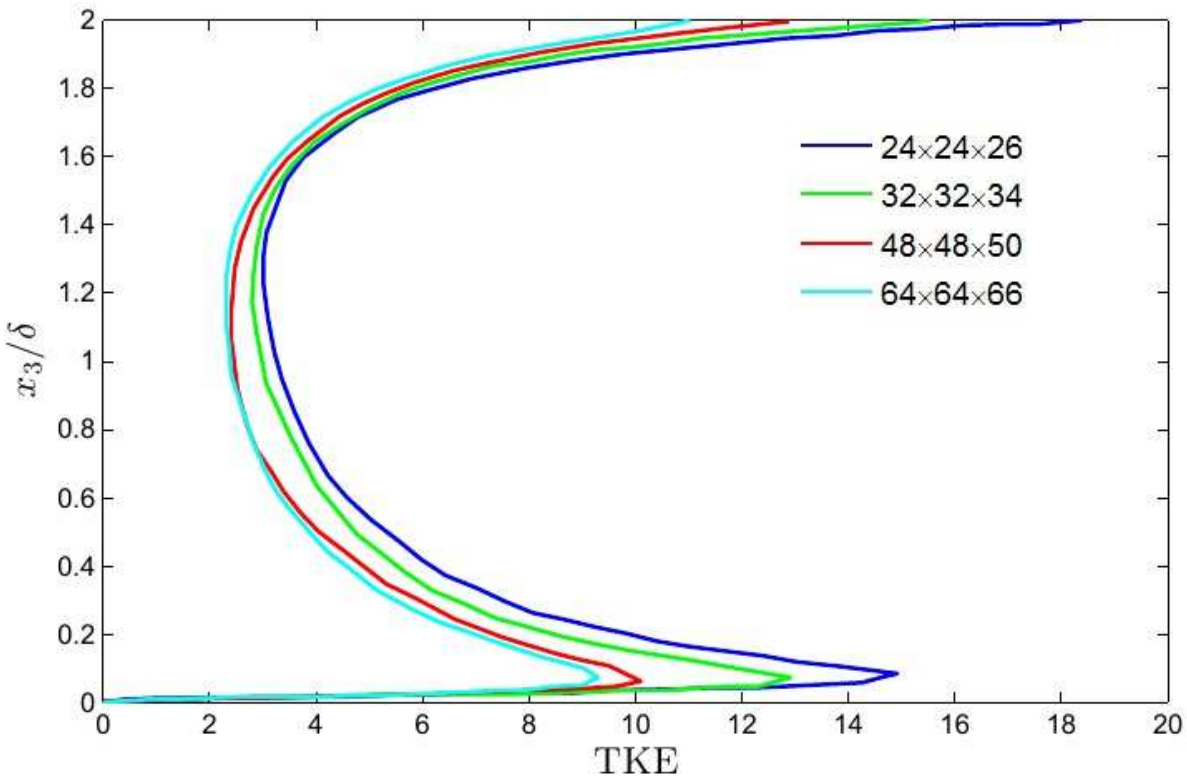

Figure 3.11: Convergence of turbulent kinetic energy (TKE) in flow with LC. Quadratic NURBS meshes were used for all cases.

of LC serves to homogenize momentum throughout the water column leading to a near constant velocity profile in the core region and thinner viscous sublayers at the surface and bottom. Figure 3.13 shows mean velocity versus wall-normal direction in wall units in the lower half of the water column. In this figure, the mean velocity, $u_1^+ = \langle u_1^h \rangle / u_*$, is plotted versus the log of $x_3^+ = x_3 u_* / \nu$, where x_3 is the wall-normal distance to the bottom wall and u_* is wall friction velocity. The latter is defined as $u_* = (\tau_{wall}/\rho)^{1/2}$ where τ_{wall} is wall shear stress and ρ is density. In flows with and without LC, global conservation of momentum yields a mean wall shear stress in balance with the imposed wind shear stress at the top surface of the domain, thus in the mean $u_* = u_\tau$,

where, recall that u_τ is wind stress friction velocity. In Figure 3.13, the flow without LC exhibits a well-developed, near-bottom log-layer in which the velocity satisfies the classical log-law of wall-bounded turbulent flows defined as

$$u_1^+ = \frac{1}{\kappa}\ln(x_3^+) + B \tag{3.27}$$

where $\kappa = 0.4$ is Von Karman's constant. In the flow without LC, $B = 7$. Meanwhile in the flow with LC, enhanced mixing associated with the Langmuir cells disrupts the classical log-layer region inducing an extended wake region at depths normally characterized by the log-law. A similar log-layer disruption has been reported in [55] in their spectral LES of full-depth LC. This deviation has been attributed to the high speed fluid brought down to the near-wall region by the downwelling limbs of the Langmuir cells [53]. A rough approximation of this disruption could be given by a shift of the usual log-law profile (i.e. by changing the B coefficient from 7 to 8.5 in (3.27), as shown in Figure 3.13. Finally, both flows exhibit a velocity profile close to the well-known theoretical profile $u_1^+ = x_1^+$ within the viscous sublayer, indicating that the near-wall region is well-resolved.

Disruption of the log-layer by the action of LC has important implications for coastal general circulation models (GCMs). Traditional RANS (Reynolds Navier-Stokes) parameterizations of the turbulent bottom boundary layer in coastal GCMs assume the presence of a well-developed log-layer. Thus, these parameterizations are not able to properly account for log-layer disruption caused by full-depth LC and ultimately wave-current interaction. This will be discussed further in Chapter 5.

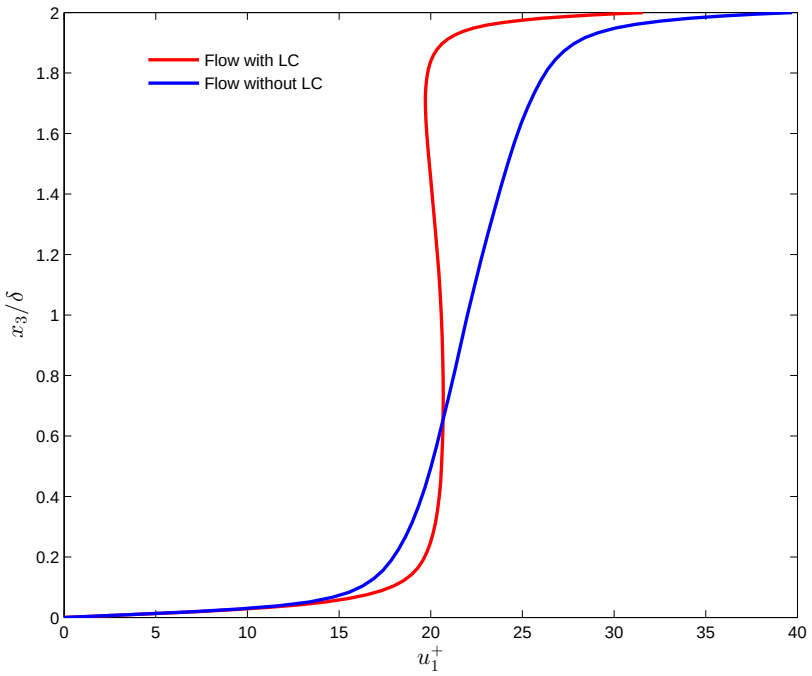

Figure 3.12: Mean downwind velocity in flows with and without LC. The $48 \times 48 \times 50$ quadratic NURBS mesh was used for both flows.

3.5 Summary

This chapter has described extension of variational multiscale turbulence modeling procedures to the C-L equation. Approximation spaces were expressed in terms of quadratic NURBS basis functions. The C-L equation was written in semilinear form revealing an advection-diffusion system characterized by non-symmetric advective matrices. The weak form of this system was treated with the RBVMS formulation described in Chapter 2 together with stabilization parameters defined in terms of the aforementioned advective matrices based on the theory presented in [44].

The methodology showed good convergence properties for a wind-driven shear flow characterized by full-depth Langmuir circulation in agreement with the field measurements in [17, 18]. A major impact of the full-depth Langmuir cells was shown to be enhanced mixing of momentum leading to a disruption of the classical near-bottom log-layer.

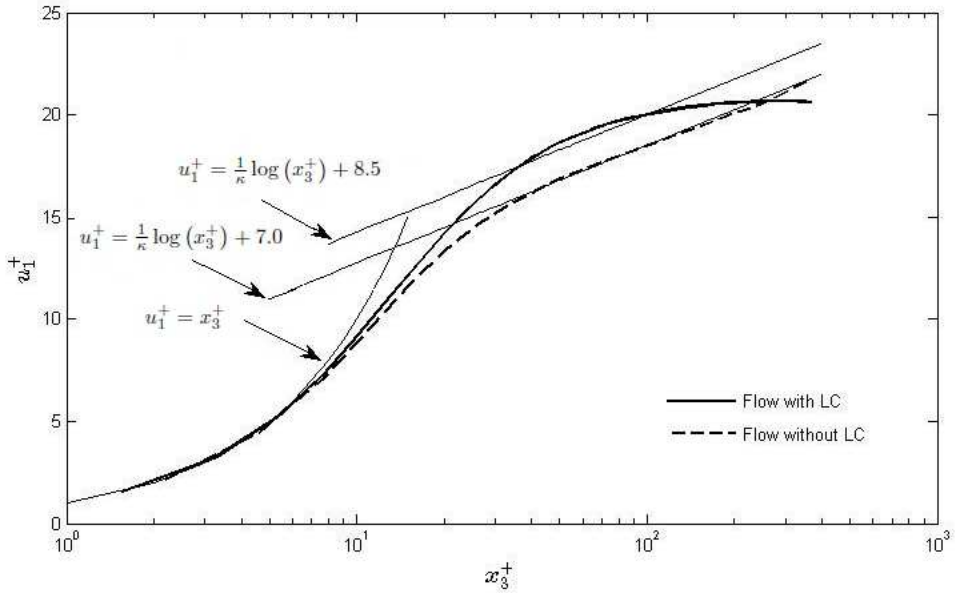

Figure 3.13: Mean downwind velocity versus wall-normal (vertical) direction in wall (plus) units in flows with and without LC. The $48 \times 48 \times 50$ quadratic NURBS mesh was used for both flows. Note that $z^+ = u_\tau(x_3^d + \delta)/\nu$.

The next chapter explores the use of wall-models as an alternative to the bottom no-slip condition imposed in the simulations presented above, bypassing resolution of the expensive near-wall viscous sublayer.

Chapter 4:

RBVMS Large Eddy Simulation of Shallow Water Langmuir Turbulence with Near-Wall Modeling

The existence of sharp gradients especially in the near-wall region poses undesired computational cost when numerical simulations are performed. To reduce this computational cost, yet another level of modeling is introduced in LES, referred to as wall modeling [41]. The idea behind wall modeling is to only resolve the core flow and model the near-wall region with suitable boundary conditions. This form of LES is often referred to as LES with near-wall modeling (or LES-NWM). The wall model obviates the need to refine the mesh in the near-wall region in order to capture near-wall sharp gradients. This is in contrast to the simulations presented in the previous chapter in which the mesh was made finer near the wall in order to resolve sharp gradients, often referred to as LES with near-wall resolution (or LES-NWR). With the lower computation cost brought about with wall modeling, more realistic problems in terms of computational domain size and Reynolds number can be solved when compared to those of DNS and LES-NWR.

In this chapter, two wall models will be explored. The first one is a model well-studied by the LES community. Instead of imposing the no-slip condition at a wall, the wall shear stress is prescribed by assumming the presence of a log layer where the mean velocity is expected to satisfy a log-law. The mean of the computed flow is assumed to satisfy such a log-law from which a wall friction velocity is extracted and in turn used to compute the prescribed wall shear stress. This model has worked well for wall-bounded flows such as in turbulent channels. However, wall

modeling has never been attempted for LES of full-depth Langmuir cells, thus its behavior in the presence of these large-scale turbulent structures needs to be evaluated. In particular, as was observed in LES-NWR in the previous chapter, the full-depth Langmuir cells induce a disruption of the log-law. An approximation of this disruption could be given by a shift of the usual log-law profile, as described in Chapter 3. However, this shift depends on the strength of the Langmuir cells, i.e. on wind and wave forcing parameters consisting of the turbulent Langmuir number and the dominant wavelength of surface waves generating LC, La_t and γ, respectively [53]. This implies that the wall model would have to depend on these parameters in order to properly adjust the assumed log-law profile used to compute the imposed wall shear stress. The current chapter investigates this dependence.

In additional to the traditional wall model used in LES, a more recent wall model is also tested. This model, introduced in [5], does not impose a wall shear stress, but rather weakly imposes the Dirichlet no-slip condition at the wall. Weak imposition of the no-slip condition is based on numerical considerations and not on physical or empirical conditions as is the case of traditional wall modeling.

In this chapter the performance of both wall models described above is investigated in RBVMS LES-NWM of full-depth Langmuir cells. Given that the near-wall region is not resolved thereby reducing the cost of the computation, the computationl domain is expanded in downwind (x_1) and crosswind (x_2) directions in order to resolve multiple cells. Recall from the previous chapter, in LES-NWR the domain was able to capture only a single Langmuir cell, thus excluding potentially important interactions between multiple cells. Here LES-NWM simulations with the horizontally expanded domain allows for resolution of multiple cells and their interaction. The impact of this

interaction on flow statistics such as mean velocity and root mean square of velocity fluctuations is investigated.

4.1 The RVBMS Formulation of The Craik-Leibovich Equations with Near-Wall Modeling

In this section two approaches at wall modeling are presented within the RVBMS formulation of the Craik-Leibovich equation developed in Chapter 3. Recall the space-discrete problem: Find $\{\mathbf{u}^h, p^h\} \in \mathscr{V}^h$ such that $\forall \{w^h, q^h\} \in \mathscr{W}^h$,

$$B(\{\mathbf{w}^h, q^h\}, \{\mathbf{u}^h, p^h\}) + B_{vms}(\{\mathbf{w}^h, q^h\}, \{\mathbf{u}^h, p^h\}) = (\mathbf{w}^h, \mathbf{f}^h)_\Omega + \left(\mathbf{w}^h, 2\nu\nabla^s\mathbf{u}^h \cdot \mathbf{n} - p^h\mathbf{n}\right)_{\Gamma_N}. \tag{4.1}$$

Furthermore, recall that the domain boundary Γ is decomposed as $\Gamma = \Gamma_E \cup \Gamma_N$ where Γ_N is the portion where essential boundary conditions are applied and Γ_N is where natural boundary conditions are applied. In the simulations of wind-driven flows performed in this chapter with domain depicted in Figure 6.1, Γ_E corresponds to the no-slip bottom at $x_3 = -\delta$ and Γ_N corresponds to the top surface at $x_3 = \delta$. In application of wall modeling techniques the no-slip bottom wall will instead be taken as a natural boundary. Thus, the bottom and top surfaces will both be taken as natural boundaries and to distinguish between these two, Γ_N is decomposed as $\Gamma_N = \Gamma_{\text{top}} \cup \Gamma_{\text{bottom}}$. Following this decomposition, the boundary term in (4.1) is re-expressed as

$$\left(\mathbf{w}^h, 2\nu\nabla^s\mathbf{u}^h \cdot \mathbf{n} - p^h\mathbf{n}\right)_{\Gamma_N} = \left(\mathbf{w}^h, 2\nu\nabla^s\mathbf{u}^h \cdot \mathbf{n} - p^h\mathbf{n}\right)_{\Gamma_{\text{top}}} + \left(\mathbf{w}^h, 2\nu\nabla^s\mathbf{u}^h \cdot \mathbf{n} - p^h\mathbf{n}\right)_{\Gamma_{\text{bottom}}} \tag{4.2}$$

The imposed wind stress in the x_1 direction at the top surface boundary remains the same as that developed in Eq. (3.21), where now the top surface is denoted as Γ_{top}:

$$\left(\mathbf{w}^h, 2\nu\nabla^s\mathbf{u}^h\cdot\mathbf{n} - p^h\mathbf{n}\right)_{\Gamma_{\text{top}}} = \int_{\Gamma_{\text{top}}} w_1^h u_\tau^2 \, d\Gamma_{\text{top}} \tag{4.3}$$

where recall that u_τ is the wind stress friction velocity. Treatment of the bottom boundary is described next.

4.1.1 Traditional Wall Model

In the traditional wall model employed, the boundary condition at the bottom wall is first developed similarly to the top surface. Following the developments of Eq. (3.21), but now applied to the bottom wall yields

$$\begin{aligned}\left(\mathbf{w}^h, 2\nu\nabla^s\mathbf{u}^h\cdot\mathbf{n} - p^h\mathbf{n}\right)_{\Gamma_{\text{bottom}}} \equiv & -\int_{\Gamma_{\text{bottom}}} w_1^h \nu\frac{\partial u_1^h}{\partial x_3} d\Gamma_{\text{bottom}} - \int_{\Gamma_{\text{bottom}}} w_2^h \nu\frac{\partial u_2^h}{\partial x_3} d\Gamma_{\text{bottom}} \\ & - \int_{\Gamma_{\text{bottom}}} w_3^h \left(\nu\frac{\partial u_3^h}{\partial x_3} - p^h\right) d\Gamma_{\text{bottom}}\end{aligned} \tag{4.4}$$

where $\mathbf{n} = (0,0,-1)^T$ has been used corresponding to the unit outward normal to Γ_{bottom}. The last two terms on the right side of (4.4) can be discarded for the following reasons. First $w_3^h = 0$ on Γ_{bottom} since $u_3^h = 0$ is imposed there, and second, $\partial u_2^h/\partial x_3 = 0$ on Γ_{bottom} corresponding to zero shear stress in the crosswind direction (x_2) at the bottom wall. Thus (4.4) may be re-expressed as

$$\left(\mathbf{w}^h, 2\nu\nabla^s\mathbf{u}^h\cdot\mathbf{n} - p^h\mathbf{n}\right)_{\Gamma_{\text{bottom}}} = -\int_{\Gamma_{\text{bottom}}} w_1^h \nu\frac{\partial u_1^h}{\partial x_3} d\Gamma_{\text{bottom}} \tag{4.5}$$

In the previous expression, the term $\nu \partial u_1^h / \partial x_3$ on Γ_{bottom} corresponds to the shear stress exerted by the wall (τ_{wall}) onto the fluid in the negative x_1 direction. The wall shear stress can be defined in terms of friction velocity u_* as follows:

$$\tau_{wall} \equiv u_*^2 \tag{4.6}$$

where the friction velocity may be obtained from its defintion

$$u_* \equiv \left(\nu \frac{\partial u_1}{\partial x_3} \right)^{1/2}_{x_3 = -\delta} \tag{4.7}$$

or alternatively may be obtained from the empirical log-law:

$$U^{\text{ol}+} = \frac{U^{\text{ol}}}{u_*} = \frac{1}{\kappa} \log \frac{\Delta z^{\text{ol}} u_*}{\nu} + B \tag{4.8}$$

where $\kappa = 0.41$ is the von Karman constant and coefficient B will be discussed further below. Furthermore, Δz^{ol} denotes the wall-normal distance from the wall to a location within the outer layer (ol) or log-layer where the mean flow velocity U^{ol} satisfies the log-law above.

As described in the introduction to this chapter, in LES-NWM, the mesh is not refined in the near-wall region, and consequently does not capture the sharp velocity gradient at the wall expected for a turbulent flow. Thus calculation of the wall friction velocity u_* via (4.7) is not possible. The friction velocity is solved iteratively at each time step from the log law in (4.8) with U^{ol} being the dimensionalized horizontally-averaged, downwind LES velocity within the log-layer layer. In the computational performed for this chapter, the NURBS elements at the wall are sufficiently coarse such that the first horizontal plane of grid points above the bottom wall lies within the log-layer.

Thus U^{ol} is calculated by averaging the dimensionalized downwind LES velocity over all of the grid points of this first horizontal plane above the wall.

In the log-law in (4.8), $B = 5.5$ for turbulent channel flows. However, as was seen in the previous chapter, the presence of full-depth Langmuir cells may cause a disruption of the log-law that may be approximated by a shifted log-law resulting from a value of B greater than 5.5. The value of B required to approximate the mean velocity induced by full-depth Langmuir cells depends on wind and wave forcing conditions (i.e. values of La_t and γ (the turbulent Langmuir number and the dominant wavelength of surface waves generating the Langmuir cells, respectively)). This dependence of B can be observed in the LES-NWR results of chapter 3 (see Figure (3.13)). In the absence of a parameterization of B in terms of La_t and γ, simulations for this chapter were conducted with different values of B in order to assess the dependence of LES statistics on this coefficient. Results from these simulations are presented further below.

In LES-NWR and in physical experiments it has been observed that τ_{wall} fluctuates in space (i.e. over x_1 and x_2) and in time. Although calculation of τ_{wall} via (4.6) and (4.8) allows for fluctuations of τ_{wall} in time, it does not allow for fluctuations in space. In order to include the latter, typically the wall shear stress is calculated as

$$\tau_{wall} = u_*^2 \, \frac{u_1(x_1, x_2, x_3^{\mathrm{ol}}, t)}{U^{\mathrm{ol}}} \tag{4.9}$$

where $u_1(x_1, x_2, x_3^{\mathrm{ol}}, t)$ is taken to be the LES downwind velocity on the first horizontal plane of grid points above the bottom wall denoted by $x_3 = x_3^{\mathrm{ol}}$. Velocity U^{ol} is calculated as explained earlier, i.e. $U^{\mathrm{ol}} = \langle u_1(x_1, x_2, x_3^{\mathrm{ol}}, t) \rangle_{x_1, x_2}$ where brackets and subpscript x_1 and x_2 denote averaging over these two directions.

In summary, the boundary term over Γ_{bottom} in (4.2) is expressed as

$$\left(\mathbf{w}^h, 2\nu\nabla^s\mathbf{u}^h\cdot\mathbf{n} - p^h\mathbf{n}\right)_{\Gamma_{\text{bottom}}} = -\int_{\Gamma_{\text{bottom}}} w_1^h\ \tau_{wall}\ d\Gamma_{\text{bottom}} \tag{4.10}$$

where the wall shear stress τ_{wall}^d is computed from (4.9) with friction velocity obtained at each time step via iterative solution of the log-law in (4.8).

4.1.2 Weak Dirichlet Bottom Boundary Condition

In the LES-NWR of Chapter 3, the no-slip bottom boundary condition was enforced strongly. Thus, the second term on the right hand side of (4.2) (i.e. the integral over Γ_{bottom}) becomes zero because $\mathbf{w}^h = 0$ is taken at essential (or Dirichlet) boundaries, as is typically done [20]. In the case of weak imposition of the no-slip bottom boundary condition (proposed in [4]), the second term on the right hand side of (4.2) is replaced by

$$\begin{aligned} B_{wbc}(\{\mathbf{w}^h\},\{\mathbf{u}^h\}) = &(\mathbf{w}^h, 2\nu\nabla^s\mathbf{u}^h\cdot\mathbf{n})_{\Gamma_{\text{bottom}}} \\ &+(2\nu\nabla^s\mathbf{w}^h\cdot\mathbf{n}, (\mathbf{u}^h-\mathbf{g}))_{\Gamma_{\text{bottom}}} \\ &-(\mathbf{w}^h, \tau_B(\mathbf{u}^h-\mathbf{g}))_{\Gamma_{\text{bottom}}}, \end{aligned} \tag{4.11}$$

weakly imposing the no-slip Dirichlet bottom boundary condition $\mathbf{u}^h = \mathbf{g}$ on Γ_{bottom} with $\mathbf{g} = \mathbf{0}$. The previous integrals may be reduced further if inserting $\mathbf{n} = (0,0,-1)$, the unit outward normal to Γ_{bottom}. Also note that in this approach, $u_3 = 0$ on Γ_{bottom} is enforced strongly, thus $w_3^h = 0$ there.

The first term on the right hand of (4.11) corresponds to the resolved viscous shear stress at the bottom wall. In LES-NWR the computed velocity is poorly resolved in the near-wall region, thus

this stress is not expected to match the correct wall shear stress. Thus, a penalty stress is added coreesponding to the third term in the right side of (4.11). The penalty stress plus the resolved viscous shear stress are expected to give the correct wall shear stress.

To ensure numerical stability and optimal convergence, the penalty parameter τ_B in equation (4.11) is chosen as

$$\tau_B = \frac{C_b \nu}{h_b} \tag{4.12}$$

with

$$h_b = \frac{2}{\sqrt{n_i G_{ij} n_j}}, \tag{4.13}$$

where n_i's are the Cartesian component of the unit outward normal vector to Γ_{bottom}, G_{ij} was defined in Chapter 3 and $C_b = 4$ is an element-wise constant emanating from error analysis [5]. For rectangular meshes, (4.13) results in the element length in the wall-normal direction. Further numerical stability can be gained via the middle term on the right hand side of (4.11) which is a so-called adjoint-consistency term. This is related to the fact that if the exact solution of the adjoint problem is inserted as the weight function into the RVBMS weak formulation (including the handling of the bottom boundary via (4.11)), then the RBVMS formulation is satisfied exactly. Additional discussion and computational results employing weakly-enforced Dirichlet conditions may be found in [4, 5].

4.2 Computational Setup

The computational domain is similar to that depicted in 6.1 and consists of a rectangular box with dimensions L_1 in the streamwise or downwind (x_1) direction, L_2 in the spanwise or crosswind (x_2) direction and L_3 in the vertical or wall-normal (x_3) direction. Various domain lengths over x_1 and x_2 directions were utilized in order to investigate their influence on turbulence structure and statistics. Domain sizes are listed in Table (4.1). This table also shows mesh resolutions in terms of the numbers of quadratic NURBS basis functions (N_1, N_2 and N_3) used in each tensor product direction. Mesh resolution is uniform in all three directions. The coarse mesh resolution in the wall-normal (vertical) direction (relative to the LES-NWR of Chapter 3) is such that viscous wall and buffer sublayers are not well-resolved, thereby requiring near-wall modeling.

Table 4.1: Summary of domain sizes and mesh resolutions used in LES-NWM.

L_1	L_2	L_3	N_1	N_2	N_3
$4\pi\delta$	$\frac{8}{3}\pi\delta$	2δ	32	64	34
$28\pi\delta$	$\frac{16}{3}\pi\delta$	2δ	256	128	34
$40\pi\delta$	$\frac{16}{3}\pi\delta$	2δ	320	128	34

4.3 Results

Figure 4.1 shows velocity fluctuations averaged over the streamwise (x_1) direction and over time on the streamwise-wall-normal plane. These averaged fluctuations reveal the cellular structure captured by the LES. In this case, one Langmuir cell was resolved with spanwise length of the domain $L_2 = 8\pi\delta/3$. This spanwise length of the cell is consistent with the field measurements in [17, 18] and the LES-NWR of Chapter 3 which used the same spanwise domain length.

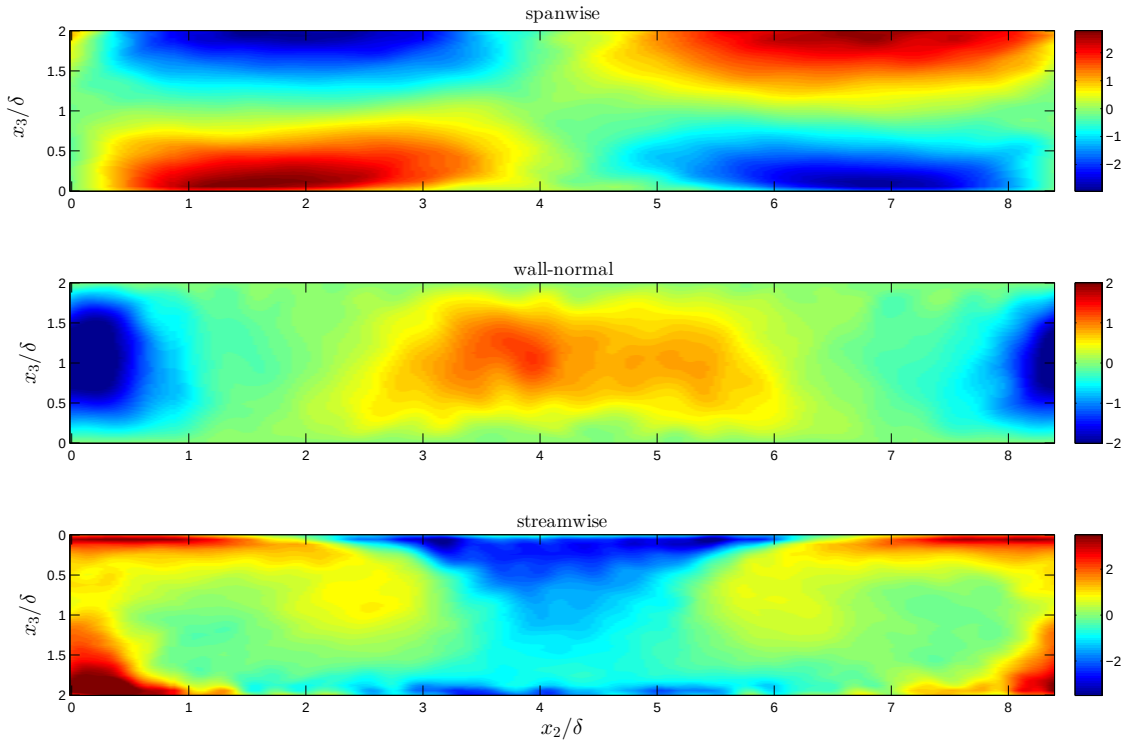

Figure 4.1: Spanwise-vertical variation of streamwise- and time-averaged spanwise (top), wall-normal (middle) and streamwise (bottom) velocity fluctuations defined in Eq. (3.26) from LES-NWM in the domain $L_1/\delta \times L_2/\delta \times L_3/\delta = 4\pi \times \frac{8}{3}\pi \times 2$. Results were obtained with the traditional wall model described in sub-section 4.1.1 with $B = 6.5$ in (4.8). Streamwise (downwind) direction (x_1) is out of page.

In Figure 4.2, the structure of the Langmuir cells is seen in the horizontal (streamwise-spanwise) $(x_1 - x_2)$ plane at mid-depth of the domain. Here instantaneous streamwise and wall-normal velocity fluctuations are characterized by downwind-elongated streaks alternating in sign in the spanwise direction, consistent with the LES-NWR results of Chapter 3.

Figure 4.3 shows instantaneous streamwise and wall-normal velocity fluctuation streaks at mid-depth in LES-NWM with the domain expanded to $L_1 = 40\pi\delta$ and $L_2 = 16\pi\delta/3$ compared to $L_1 = 4\pi\delta$ and $L_2 = 8\pi\delta/3$ in Figure 4.2. The expanded domain is able to resolve three Langmuir cells, as can be seen by the three pairs of positive and negative downwind-elongated streaks characterizing the instantaneous streamwise and wall-normal velocity fluctuations. Furthermore, the

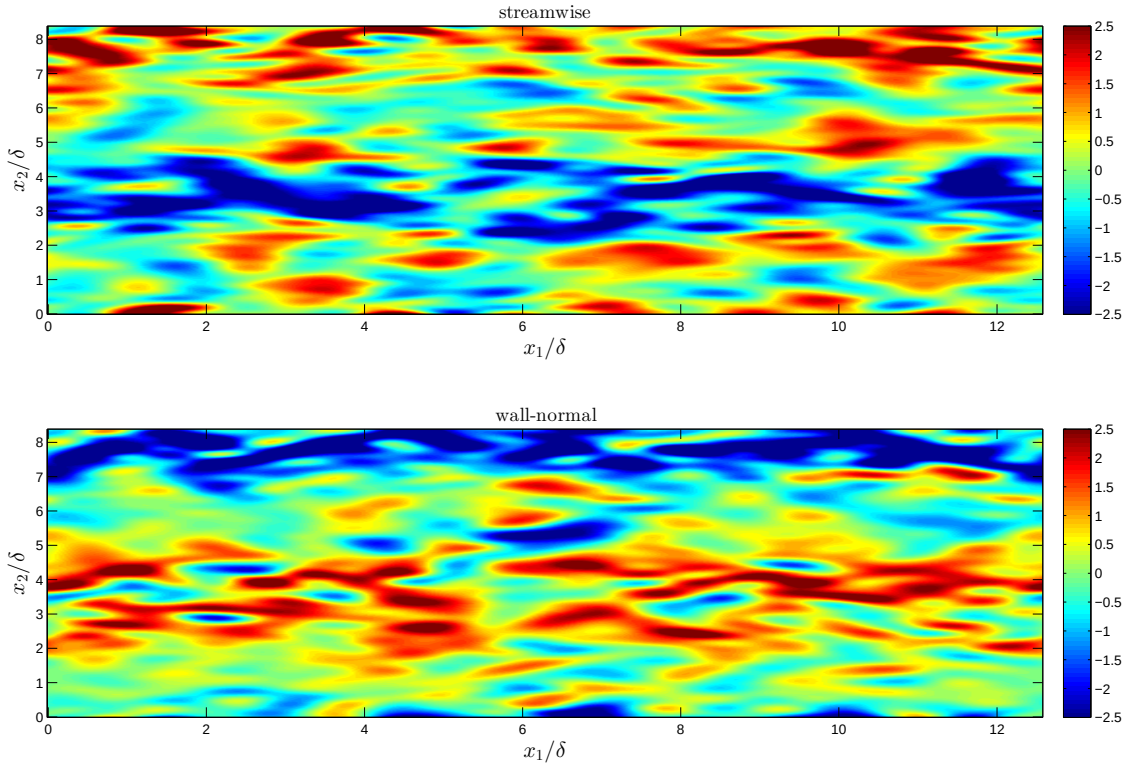

Figure 4.2: Mid-depth streamwise-spanwise plane of instantaneous streamwise (top) and wall-normal (bottom) velocity fluctuations from LES-NWM in the domain $L_1/\delta \times L_2/\delta \times L_3/\delta = 4\pi \times \frac{8}{3}\pi \times 2$. Results were obtained with the traditional wall model with $B = 6.5$ in (4.8).

expanded streamwise length of the domain allows for the cells to interact with each other. Such interaction gives rise to cell meanderings and mergings as is seen in Figure 4.3. The merging of cells is often observed during field occurrences of Langmuir cells and is typically referred to as a "y-junction" [58]. The expanded domain also gives rise to finer (grainier) scale features associated with the streaks.

Figure 4.4 shows mean velocity in LES-NWM with the traditional wall model. This figure shows results from the different domains listed earlier in Table 4.1. The mean velocity in wall units is characterized by a deviation from the log-law. As described in Chapter 3, this deviation has been attributed to the high speed fluid brought down to the near-wall region by the downwelling limbs of

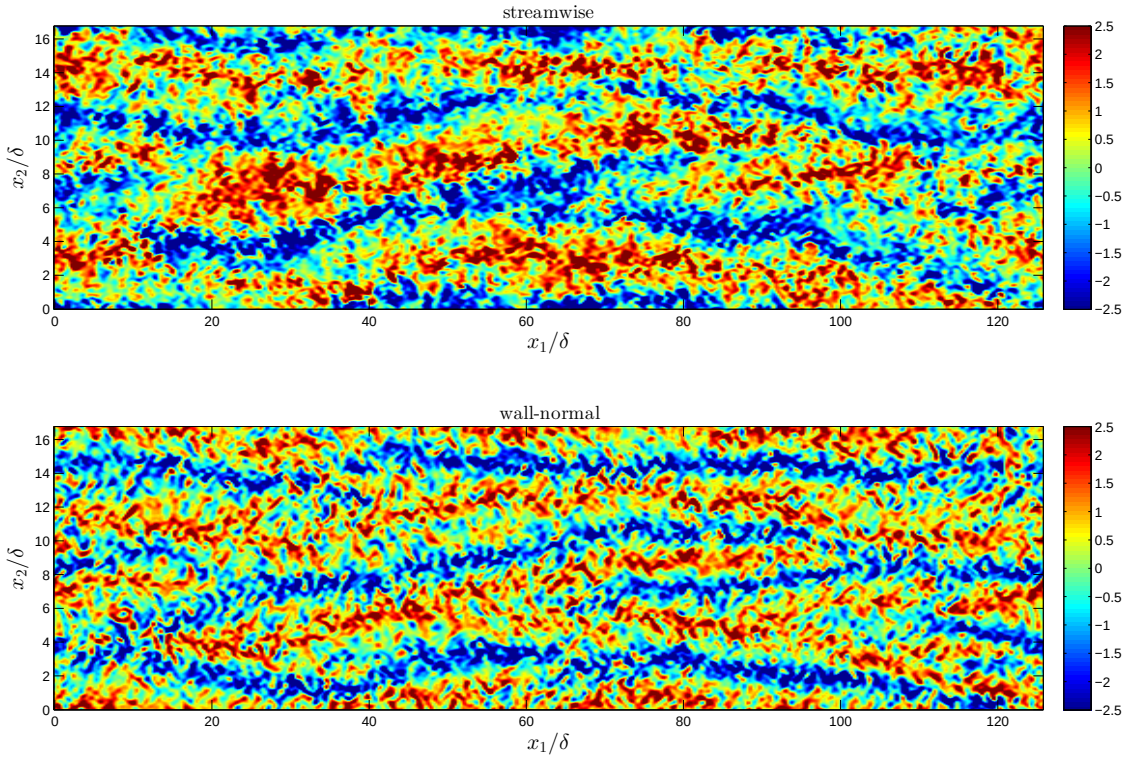

Figure 4.3: Mid-depth streamwise-spanwise plane of instantaneous streamwise (top) and wall-normal (bottom) velocity fluctuations scaled by u_τ from LES-NWM in the domain $L_1\delta \times L_2/\delta \times L_3/\delta = 40\pi \times \frac{16}{3}\pi \times 2$. Results were obtained with the traditional wall model in sub-section with $B = 6.5$ in (4.8).

the Langmuir cells [53]. Thus, the log-law deviation depends on the strength of these limbs, which can be measured, for example, in terms of root mean square of wall-normal velocity [45]. As can be seen in Figure 4.4, the deviation from the log law is robust across LES-NWM simulations with different horizontal domain lengths. Furthermore, all LES-NWM cases predict a mean velocity in good agreement with the velocity calculated via LES-NWR (in Chapter 3), the latter using the smallest domain listed in Table 4.1 and a stretched mesh in the x_3 direction so as to resolve the viscous boundary layer at the bottom wall. In contrast, the LES-NWM simulations use a uniform mesh in x_3 with fewer elements so as to not resolve all of the energetic scales within this region. These results imply that LES-NWM is able to perform well in capturing the strength of the full-

depth upwelling and downwelling limbs of the Langmuir cells and the associated disruption of the velocity log law despite its poor resolution of the near-wall region. Furthermore, the strength of the downwelling limbs and resulting deviation of mean velocity from the log law is nearly independent of horizontal domain length and cell meanderings.

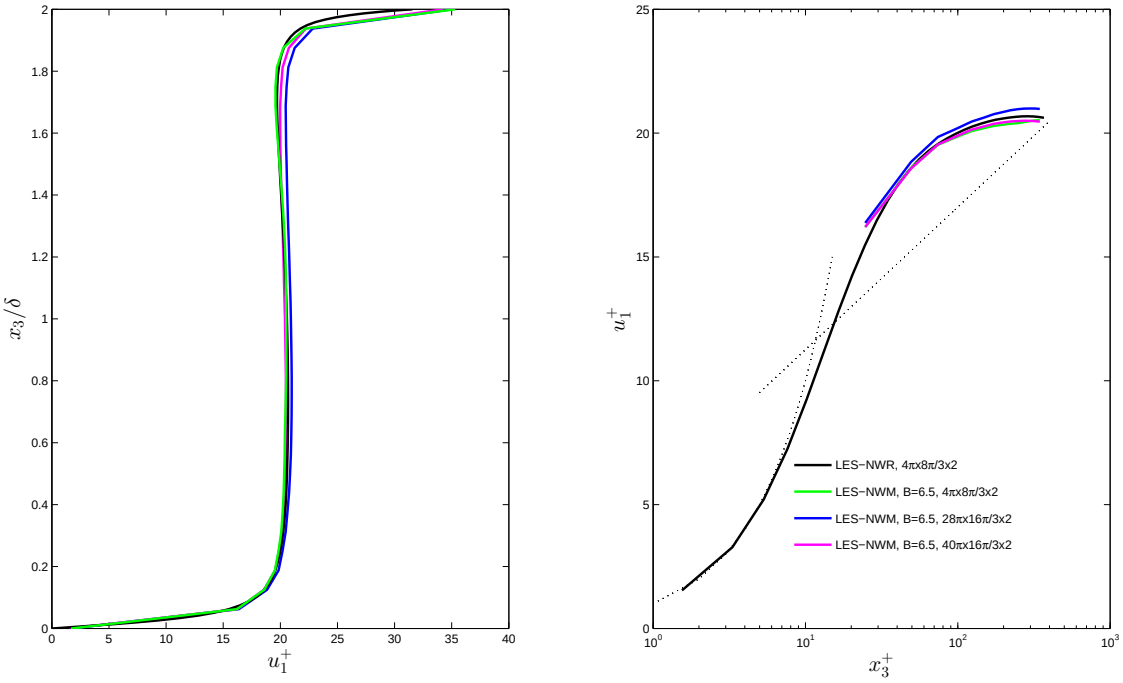

Figure 4.4: Mean velocity in regular units (left) and plus units (right) for LES-NWM in domains of various lengths. Domain lengths are specified in the figure legend in dimensionless units. Results were obtained with the traditional wall model described in sub-section 4.4.1 with $B = 6.5$ in (4.8). The LES-NWR appearing in the figure was performed with a quadratic NURBS mesh with $N_1 = N_2 = 64$ and $N_3 = 66$ with non-uniform mesh in x_3. Details of the LES-NWM are shown in Table 4.1.

Figure 4.5 shows root mean square (rms) of velocity. These rms quantities are obtained following the Reynolds decomposition described in (3.24) as

$$u_i\text{-rms} \equiv \langle u^{h\,\prime}_{(i)} u^{h\,\prime}_{(i)} \rangle = \langle u^h_{(i)} u^h_{(i)} \rangle - \langle u^h_{(i)} \rangle \langle u^h_{(i)} \rangle \tag{4.14}$$

where the parenthesis is meant to supress the Einstein summation convention. Note that for flows in statistical equilibrium as being considered in this work, time averages are sufficiently long such that $\langle u^{h\prime}_{(i)} \rangle = 0$ and thus the latter expression is used to obtain (4.14). Results from LES-NWM with the traditional wall model and different domain lengths in x_1 and x_2 do not show significant differences in streamwise, spanwise and wall-normal velocity rms (u_1-rms, u_2-rms, u_3-rms, respectively). In Figure 4.5 (left panel) the near-bottom peak in u_1-rms predicted by LES-NWM with the traditional wall model on the smallest domain listed in Table 1 is significantly higher than the peak predicted by LES-NWR on the same domain. This could potentially be due to the under-resolution of the LES-NWM ($N_1 = 32$) compared with the LES-NWR ($N_1 = 64$) in the streamwise direction. Finally, the significant non-zero value of u_2-rms at the bottom wall (see Figure 4.5; middle panel) is an artifact of the wall slip velocity associated with the traditional wall model. This non-zero value of u_2-rms at the wall may simply be over-written with a zero.

As mentioned earlier, the LES-NWM results of Figures 4.4 and 4.5 were obtained with the tradional wall model. Cases (not shown here) were run with different values of B in (4.8), given the deviation from the log-law induced by the Langmuir cells. For example, a case with $B = 5.5$ did not yield significant differences from the mean velocity and rms of velocity profiles in Figures 4.4 and 4.5 obtained with $B = 6.5$.

Finally, Figure 4.6 shows a comparison between LES-NWM with the traditional wall model described in sub-section 4.1.1 and the weak imposition of the no-slip bottom described in sub-section 4.1.2. The weakly enforced no-slip bottom boundary condition leads to under-prediction of the near-bottom u_1-rms and u_2-rms peaks relative to the traditional wall model, perhaps due to damping of near-wall fluctuations by the penalty term (i.e. the third term on the right hand side) in equation (4.11). Differences between the mean velocity predicted by these two near-wall

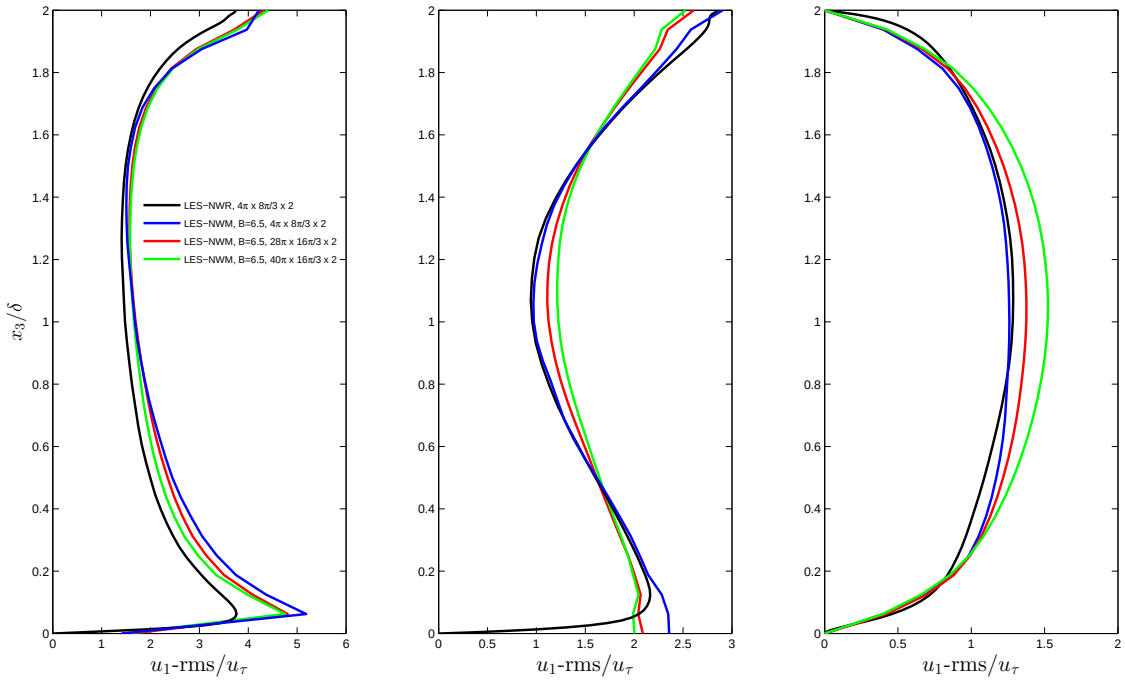

Figure 4.5: Root mean square of velocity for LES-NWM in domains of various lengths. Domain lengths are specified in the figure legend in dimensionless units. Results were obtained with classical wall model in sub-section 3.1 with $B = 6.5$ in (4.8). The LES-NWR appearing in the figure was performed with a quadratic NURBS mesh with $N_1 = N_2 = 64$ and $N_3 = 66$ with non-uniform mesh in x_3. Details of the LES-NWM are shown in Table 4.1.

treatments were not significant (not shown) and thus both wall models are able to accurately predict the strength of upwelling and downwelling limbs of full-depth Langmuir cells, and the asociated disruption of the velocity log law.

4.4 Summary

This chapter presented results from LES-NWM of Langmuir turbulence in shallow water characterized by full-depth Langmuir circulation. LES-NWM with domain lengths sufficiently wide and long allowed for the resolution of multiple Langmuir cells and the interaction between the cells resulting in cell meanderings and thus the so-called “y-junctions”. It was seen that the strength of full-depth downwelling limbs generating deviation from the log law (characteristic of the mean

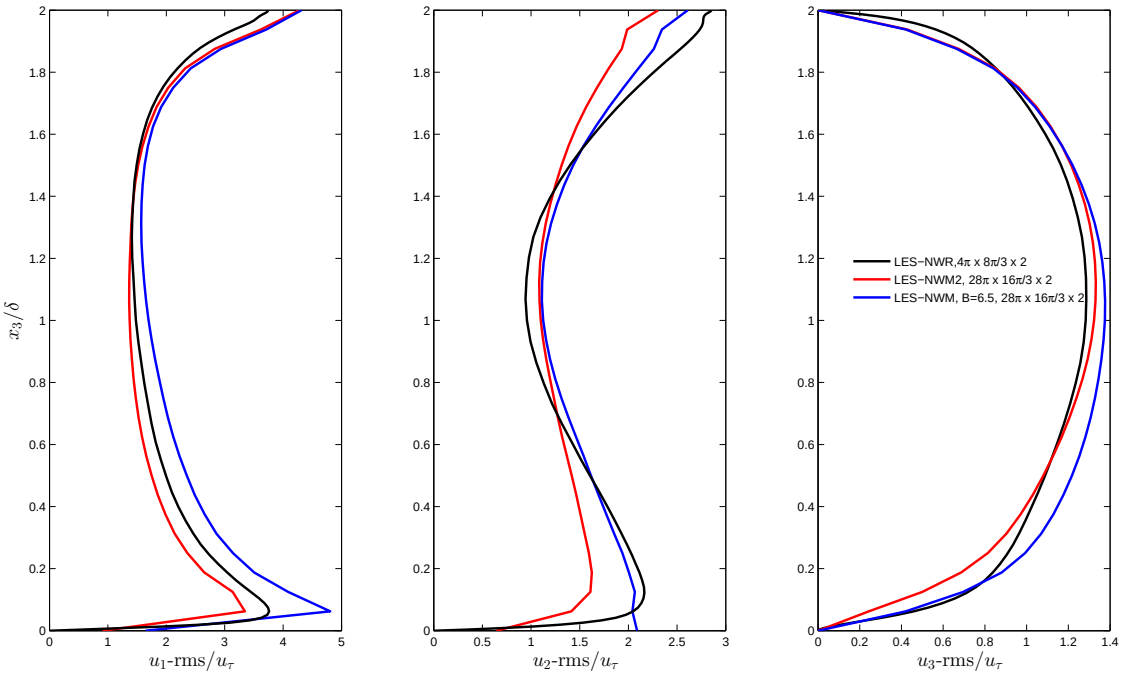

Figure 4.6: Root mean square of velocity from LES with the classical wall model in sub-section 3.1 with $B = 6.5$ in (4.8) (denoted as LES-NWM in the figure legend) and LES with the alternate wall treatment based on weak imposition of the no-slip bottom boundary condition in (3) (denoted as LES-NWM2 in the legend). Domain lengths are specified in the figure legend in dimensionless units.

velocity profile of typical boundary layers) is independent of cell meanderings and thus horizontal domain lengths. This is an important result as it shows that future LES simulations aiming to obtain parameterizations of the strength of full-depth downwelling and upwelling limbs of Langmuir cells in terms of wind and wave forcing conditions may be performed on smaller domains capturing only one single cell and thus requiring less expensive meshes. As was shown in [53] and [45], the deviation from the log-law caused by full-depth Langmuir cells is directly proportional to the strength of the downwelling limbs. Furthermore, parameterizations of the vertical mixing in the Reynolds-averaged Navier-Stokes (RANS) equations resulting from the action of these limbs is principally dependent on their strength and thus require accurate parameterization of this strength [45]. Such a vertical mixing parameterization would be useful for inclusion in coarse-scale coastal

general circulation models that do not resolve the Langmuir cells yet still (up to date) use vertical mixing parameterizations that do not account for Langmuir circulation.

Langmuir cell meanderings are an important feature of lateral dispersion by Langmuir turbulence, thus LES-NWM simulations on horizontally expanded domains are still recommended in order to provide a parameterization of lateral dispersion by Langmuir cells.

Finally, LES-NWM with weak imposition of the no-slip bottom condition tends to underpredict streamwise and spanwise velocity rms relative to LES-NWM with the traditional wall model. However, LES-NWM with weak imposition of the no-slip bottom is still able to accurately represent the strength of the downwelling limbs of the Langmuir cells and thus the mean velocity log-law deviation.

The next chapter focuses on extending the weak imposition of the no-slip bottom to coarse-scale simulations of wind and wave driven flows based on the RANS equations that do not resolve the Langmuir cells. As will be seen, results show that weak imposition of the no-slip bottom is a viable option for these types of simulations given the observed significant dependence of traditional RANS turbulence models on the B coefficient in (4.8).

Chapter 5:

RANS Simulation of Shallow Water Langmuir Turbulence with Near-Wall Modeling

As described in the Introduction, the total number of grid points required for a direct numerical simulation (DNS) should be $N \approx Re^{9/4}$. Most of the flows in applied sciences and engineering applications have a Reynolds number in range of $10^4 < Re < 10^8$. Therefore, the requirement of massive computational resources for DNS limits its applicability. Although LES offers a less computationally intensive alternative, it is still prohibitive in many applications such as in geophysical flows as LES requires resolution of a disparate range of scales extending from the largest scales of the turbulence down to the significantly smaller scales within the inertial subrange. In oceanic flows, one of the largest domains LES has been applied to consists of a 5.76 km by 10.5 km horizontal upper ocean region, 120 meters in depth with grid resolution of 3 meters [47]. The focus of that study was to understand the breakdown of frontal sub-mesoscale eddies of 1 km in horizontal scale into smaller scale turbulence. The necessity to study the general ocean circulation requires resolution of much larger scales. For example, the classical problem of wind-driven coastal upwelling and downwelling requires resolution of horizontal scales of O(100 km), for which LES (say with grid cell size of O(1 m) similar to that of [47]) is out of reach given current computational resources. In order to investigate such flow phenomena, researchers turn to simulation based on the Reynolds-averaged Navier-Stokes (RANS) equations in which only the mean component of the flow is resolved while the effect of the entire spectrum of unresolved turbulent scales is param-

eterized often via a an eddy viscosity stress. In RANS simulation, none of the turbulent scales are resolved. This in contrast to LES in which a significant portion of the turbulence is resolved.

In this chapter, stabilization in the form of SUPG is extended to the RANS simulation methodology along with near-wall modeling based on weak imposition of the no-slip boundary condition. This combination will be used to peform RANS of the wind and wave forced flows with full-depth Langmuir cells studied in previous chapters. In these RANS simulations, the Langmuir cells are not resolved and the turbulence will be be accounted for through the aforementioned eddy viscosity stress, and so the role of SUPG will be purely to stabilize the computation given the expected sharp gradients of the eddy viscosity stress. Note that stabilization is not able to account for all of the unresolved scales, in this case corresponding to the full spectrum of turbulent scales. As will be seen, results show that weak imposition of the no-slip bottom is a viable option for RANS simulations with full-depth Langmuir cells given the observed significant dependence of results on the B coefficient in in the log law (4.8) assumed when using a traditional wall model.

5.1 Reynolds-Averaged Craik-Leibovich Equation

Recall the Reynolds decomposition of a turbulent field such as velocity:

$$\mathbf{u} = \langle \mathbf{u} \rangle + \mathbf{u}' \tag{5.1}$$

where the brackets denote an ensemble average (e.g. averaging over time) the superscript prime denotes the turbulent fluctuation. Ensemble-averaging (i.e. Reynolds-averaging) the Craik-Leibovich

equation and the momentum equation results in

$$\frac{\partial \langle \mathbf{u} \rangle}{\partial t} + \nabla \cdot (\langle \mathbf{u} \rangle \otimes \langle \mathbf{u} \rangle) + \nabla \langle p \rangle + \nabla \cdot \langle \mathbf{u}' \otimes \mathbf{u}' \rangle - \nabla \cdot (2\nu \nabla^s \langle \mathbf{u} \rangle) - \phi \times \nabla \times \langle \mathbf{u} \rangle = \langle \mathbf{f} \rangle \text{ in } \Omega \quad (5.2)$$

$$\nabla \cdot \langle \mathbf{u} \rangle = 0 \text{ in } \Omega \quad (5.3)$$

where the classical Reynolds stress is $-\langle \mathbf{u}' \otimes \mathbf{u}' \rangle$, not to be confused with the subgrid-scale Reynolds stress resulting from scale decomposition in the RBVMS LES equations (2.23)-(2.16). Ensemble-avaraging generates a closure problem in terms of the Reynolds stress given that the fluctuations $\mathbf{u}'$ are unknown. Thus, the Reynolds stress needs to be modeled or approximated. Here, the Reynolds stress is modeled using an eddy viscosity stress as

$$-\langle \mathbf{u}' \otimes \mathbf{u}' \rangle = 2\nu_t \nabla^s \langle \mathbf{u} \rangle \quad (5.4)$$

where ν_t is the eddy viscosity.

Considering only local wind and surface wave forcing (e.g. setting $\mathbf{f} = \mathbf{0}$ and neglecting meso and submesoscale eddies and effects due to lateral boundaries and bottom bathymetry) as was done in previous chapters, the ensemble averaging may be taken as an average over time and horizontal directions x_1 and x_2. In this case the flow equations reduce to the following one-dimensional or single water column model for the ensemble or Reynolds-averaged downwind (x_1) velocity $u(x_3)$

$$\frac{d}{dx_3}\left((\nu + \nu_t) \frac{du}{dx_3} \right) = 0 \quad (5.5)$$

Note that the Craik-Leibovich vortex force does not appear in this x_1-momentum equation, given that the Stokes drift velocity vector ϕ is taken to have a non-zero component only along x_1 as was the case in previous chapters.

The effect of Craik-Leibovich vortex forcing or better yet Langmuir turbulence on mean velocity downwind u is incorporated through a depth-dependent (x_3-dependent) eddy viscosity ν_t. Such an eddy viscosity has been derived in [45] based on the well-known k-profile parameterization (KPP) [32] and following LES results of [53].

The eddy viscosity ν_t introduced in [45] accounts for near-top surface local vertical mixing induced by Stokes drift shear (i.e. vertical gradient of Stokes drift velocity). In order to account for non-local vertical mixing induced by the full-depth upwelling and downwelling limbs of Langmuir cells, an additional depth-dependent stress was introduced in [45], τ_{nl}. With this new stress, the single water column model becomes

$$\frac{d}{dx_3}\left((\nu+\nu_t)\frac{du}{dx_3}+\tau_{nl}\right)=0\in(0,2\delta) \tag{5.6}$$

with a stress boundary condition at the top of the water column $(x_3=2\delta)$ and no-slip at the bottom $(x_3=0)$, respectively,

$$\begin{aligned}\nu\left(\tfrac{du}{dx_3}\right)_{x_3=2\delta} &= u_\tau^2\\ u|_{x_3=0} &= 0\end{aligned} \tag{5.7}$$

These boundary conditions are the same as the full three dimensional problem solved via LES-NWR in Chapter 3.

The interested reader is directed to [45] for the derivations of and explicit expressions for eddy viscosity ν_t and non-local stress τ_{nl} in terms of wind and wave forcing parameters: La_t, λ (see

Chapter 3 for defintions) and Stokes drift vertical shear. In the absence of Craik-Leibovich vortex forcing τ_{nl} vanishes and ν_t reverts back to the eddy viscosity given by the standard KPP model in [32]. Furthermore, τ_{nl} and ν_t vanish at $x_3 = 0$ and $x_3 = 2\delta$.

Single water column models such as (5.6) are often employed to test vertical mixing parameterizations for further implementation in three-dimensional general circulation simulations as well as for water column response to local forcing conditions and impact on biological and chemical processes (e.g. see GOTM.net and references within).

5.2 Stablized Discrete Formulation

The strong form in (5.6) may be re-expressed as

$$a\frac{du}{dx_3} + \nu_t\frac{d^2u}{dz^2} + \frac{d}{dx_3}\left(\nu\frac{du}{dx_3} + \tau_{nl}\right) = 0 \tag{5.8}$$

with $a = d\nu_t/dx_3$. The term $a\,du/dx_3$ possesses the form of an advective term, thus, application of the Galerkin method to (5.8) can result in instability and the formulation needs to be stabilized. However, stabilization via application of the variational multiscale method (described in Chapter 2) is not possible because the so-called advective term in (5.8) can not be expressed in conservation form (i.e. in the form of $d(au)/dx_3$) as in the case of the Navier-Stokes equation. Consequently, here the Galerkin method is stabilized using traditional application of streamline upwind Petrov / Galerkin (SUPG) stabilization with advective velocity a. Furthermore, note that the SUPG stabilization is not able to account for the turbulence, which is being parameterized via the eddy viscosity ν_t and non-local stress τ_{nl} described earlier.

Let $\mathscr{V}^h$ denote the space piecewise linear functions (i.e. linear finite elements) and let the solution and test (weighting) functions both come from this same space. The weak form of the problems is stated as follows: Find $u^h \in \mathscr{V}^h$ such that $\forall w^h \in \mathscr{V}^h$,

$$\int_0^{2\delta} \frac{dw^h}{dx_3}(\nu+\nu_t)\frac{du^h}{dx_3}dx_3 + \int_0^{2\delta} \frac{dw^h}{dz}\tau_{nl}dx_3 - w^h u_\tau^2 + B_{\text{SUPG}}(w^h,u^h) = 0 \tag{5.9}$$

where the SUPG terms are

$$B_{\text{SUPG}}(w^h,u^h) = -\int_{x_3=0}^{2\delta} \tau\, a\, \frac{dw^h}{dx_3}\left((\nu+\nu_t)\frac{d^2u^h}{dx_3^2} + a\frac{du^h}{dx_3} + \frac{d\tau_{nl}}{dx_3}\right)dx_3 \tag{5.10}$$

and the stabilization parameter is

$$\tau = \frac{C\,h^2}{\nu+\nu_t} \tag{5.11}$$

with C a coefficient defined in [13].

5.3 Wall Modeling

As noted in the introduction of Chapter 4, wall-bounded turbulent flows are characterized by sharp gradients at the wall. The fact that sharp gradients exist within narrow regions near the walls, posses extensive computational challenges and cost. As the result, any successful numerical simulation will require fine grid resolution and particularly in near wall regions. In order to by-pass resolution of these gradients, we resort to wall modeling. In this chapter will implement both, the traditional Wall Model (TWM) and, weakly imposed No-slip velocity condition at the wall.

5.3.1 Traditional Wall Model (TWM)

In the traditional approach tested here, the no-slip condition at the bottom of the water column (see (5.7)) is enforced strongly. A uniform mesh in x_3 will be chosen such that the first grid point is within the expected log-layer. That is, this mesh will not resolve the viscous sub-layer where molecular viscosity plays a dominant role in the dynamics and the velocity is characterized by a strong gradient in x_3. Thus given this relatively coarse mesh at the wall and if the velocity at the first grid point off the wall is to satisfy the log-law, then the resolved viscous wall shear is not expected to match the prescribed surface wind stress (in (5.7)) as required by conservation of momentum. In fact, given the no-slip velocity at the wall and assuming the velocity at the first grid point off the wall satisfies the log-law, the resolved viscous wall shear stress should under-predict the expected wall shear stress. In order to overcome this difficulty, at the wall, the molecular viscosity is replaced with an effective viscosity

$$\nu_{\text{eff}} = \frac{(z_1/\delta)}{\frac{1}{\kappa}\log(z_1\nu/u_\tau)+B} \tag{5.12}$$

derived in [7] in accordance with classical boundary layer (log-layer) theory. In (5.12), z_1 denotes the distance between the wall at $x_3 = 0$ and the first grid point off the wall. As described in Chapter 3 (see discussion of Figure 3.13), full-depth Langmuir cells induce a deviation from the typical velocity log-law profile with $B = 5.5$ which may be approximated by letting $B > 5.5$. The appropriate value of B depends on wind and wave forcing parameters, however, a parameterization of B does not exist. In the LES-NWR of wind and wave-driven flow with $La_t = 0.7$ and $\lambda = 12\delta$ studied in Chapter 3, B was found to be 8.5. Here we will use the single water column model to model this same flow study the dependance of results on B by setting B to 5.5 and 8.5.

5.3.2 Weak Imposition of The Wall No-Slip Condition

Rather than modifying the viscosity at the wall, in the weak imposition of the no-slip condition, the left hand side of the weak form in (5.9) is augmented with the following term:

$$B_{wbc}(w^h,u^h) = \left[w^h \nu \frac{du^h}{dx_3}\right]_{x_3=0} - \left[\frac{dw^h}{dx_3}\nu u^h\right]_{x_3=0} + \left[w^h \tau_B u^h\right]_{x_3=0} = 0 \tag{5.13}$$

where penalty parameter is $\tau_B = C_b\nu/h$ with $C_b = 4$ and h the uniform grid spacing. The terms in (5.13) are the one-dimensional versions of the terms in (4.11) in Chapter 4.

5.4 Results

The single water column model previously developed is used to predict the mean velocity for wind and wave driven flow with $Re = 395$, $La_t = 0.7$, and $\lambda = 12\delta$ (see Chapter 3; sub-section 3.3) studied in previous chapters via LES-NWR (LES with near-wall resolution) and LES-NWM (LES with near-wall modeling). In particular we compare results of the single water column with LES-NWR. Recall that LES-NWR made use of 64x64x64 quadratic NURBS elements with wall normal grid stretching so as to resolve down into the viscous sub-layer. In the case of the single water column model, the domain (i.e. the range $[0,2\delta]$) is discretized into 32 linear finite elements with 33 uniformly spaced grid points.

A comparison of results obtained with the single water column model and LES-NWR is shown in Figure (5.1). The single water column model with the weak no-slip bottom boundary condition performs well predicting the deviation of the mean velocity away from the logl-law in excellent agreement with LES-NWR. Meanwhile, the prediction of the single water column model with the traditional wall model strongly depends on the B coefficient used to determine the effective

viscosity in (5.12) in accordance with the log-law. The advantage of the weak imposition of the no-slip wall is clearly evident as this wall treatment does not make use of the log-law and thus there is no need for the B coefficient. These results suggest that weak imposition of the Dirichlet boundary condition is a robust wall model capable of leading to good results even for cases when the near-wall behavior deviates from classical boundary layer theory (i.e. the log-law).

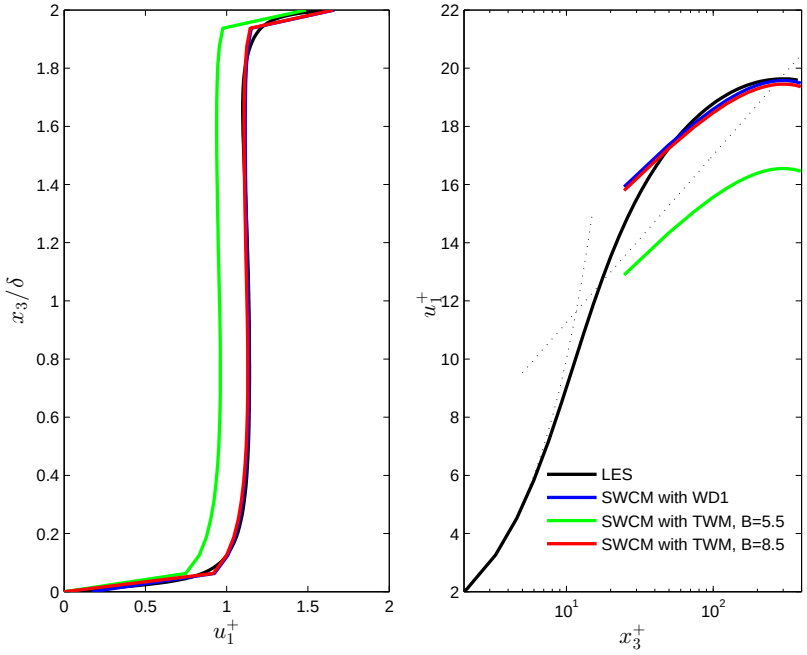

Figure 5.1: Mean velocity obtained in wind and wave-driven flow simulated via the single water column model (SWCM) with different wall models and LES-NWR.

5.5 Summary

In this chapter, stabilization in the form of SUPG was extended to the Reynolds-averaging methodology along with near-wall modeling based on weak imposition of the no-slip boundary condition. This combination was used to develop a single water column model of the wind and wave forced flows with full-depth Langmuir cells studied in previous chapters. In the single water

column model, the Langmuir cells are not resolved and the associated turbulence was accounted for through an eddy viscosity stress. It was seen that the single water column model with weak imposition of the no-slip wall boundary condition led to a prediction of the mean downwind velocity in excellent agreement with LES-NWR. Furthermore, it was seen that the mean velocity prediction of the single water column model with a traditional wall model depends greatly on the B coefficient in the log-law used to calculate the model's effective eddy viscosity at the wall. The B coefficient itself depends on the strength of the Langmuir cells being parameterized. In the absence of a parameterization of the B coefficient, the weak imposition of the no-slip wall was deemed a robust wall model leading to excellent results without the need to tune parameters.

Chapter 6:

New Developments in RBVMS LES with Near-Wall Modeling

6.1 Introduction

In large-eddy simulations (LES) of wall-bounded turbulent flows, near-wall sharp gradients and near-wall small eddies scaling with distance to the wall pose undesired computational cost. Wall modeling is often employed to reduce this cost [42], as was done in chapter 4 in flows with full-depth Langmuir cells. In LES with near-wall modeling (or LES-NWM) the core flow is resolved and the unresolved near-wall region is modeled through a suitable boundary condition. The wall model obviates the need to refine the mesh in the near-wall region in order to capture near-wall features such as sharp gradients and small eddies. This is in contrast to simulations in which the mesh is made finer near the wall (often referred to as LES with near-wall resolution or LES-NWR) in order to resolve near-wall features. With the lower computation cost brought about with wall modeling, more realistic problems in terms of computational domain size and Reynolds number can be solved when compared to those of LES-NWR and direct numerical simulation (DNS).

In traditional wall modeling, instead of imposing the no-slip condition at a wall, the wall shear stress is prescribed by assumming the presence of a log layer where the mean of the LES-resolved velocity is taken to satisfy the log law, part of the well-known law of the wall. The mean of the computed flow is assumed to satisfy the log law from which a wall friction velocity is extracted and in turn used to prescribe the wall shear stress.

An alternate approach to wall modeling was introduced in [4]. This approach is based on weak imposition of the Dirichlet no-slip condition at the wall. More specifically, the variational (weak) form of the Navier-Stokes equations is augmented by terms that enforce the no-slip conditions weakly as Euler Lagrange conditions. A key component is a penalty term whose integrand is comprised of the deviation of the discrete solution from the Dirichlet no-slip condition at the wall. The integrand of the penalty term is also proportional to a penalty parameter, τ_B, chosen to ensure numerical stability and optimal convergence of the discretization. This approach has already been seen in Chapter 4 in LES-NWM of Langmuir turbulence in shallow water.

Weak imposition of the no-slip condition is based on numerical considerations and not on physical conditions as is the case of traditional wall modeling. In this chapter, weak imposition of the no-slip condition is re-visited and reformulated to be consistent with the law of the wall. In particular, the penalty parameter τ_B is computed following the law of the wall by considering the penalty term as being representative of the unresolved shear stress at the wall, given that the relative coarseness of the mesh in the wall-normal direction causes the resolved molecular viscous shear to under-predict the expected wall shear stress.

The merit of this new formulation is that it is designed to inherit the positive numerical attributes of the original formulation while being consistent with the law of the wall. Furthermore, its alignment with the law of the wall opens the door for future improvements of the new formulation following developments already made for the traditional wall model [42].

In this chapter, results from LES-NWM of pressure gradient-driven open channel flow with prior and new (current) formulations of the weak Dirchlet no-slip condition at the wall are compared with those from LEWS-NWM with a traditional wall model. Additional comparisons are made between results with weak imposition of the no-slip condition and DNS. It is observed that

the new (current) formulation of the weak Dirchlet condition offers improvements over the prior formulation, in particular, in terms of root mean square of stream-wise velocity.

The chapter is organized as follows. Sections 2 and 3 present the incompressible Navier-Stokes equations and their weak form. Section 3 gives the discrete, residual-based variational multiscale formulation for the weak form. Section 4 gives details of the traditional wall model and the models based on weak imposition of the no-slip condition at the wall. Section 5 provides descriptions of the flow configuration, the mesh and overall numerical algorithm. Section 6 provides a comparison of results obtained from DNS, LES-NWM with the traditional wall model, and LES-NWM with the various formulations of the weak imposition of the no-slip wall condition. Conclusions are drawn in section 7.

6.2 The Navier-Stokes Equations at The Continuous Level

Let $\Omega \in \mathbb{R}^3$ be the problem domain and let $\partial\Omega$ denote its boundary. A conservative form of the dimensionless Navier-Stokes equations in the Eulerian frame are taken as a starting point of our developments, and are given as

$$\frac{\partial \mathbf{u}}{\partial t} + \nabla \cdot (\mathbf{u} \otimes \mathbf{u}) + \nabla p - \nabla \cdot (2\nu \nabla^s \mathbf{u}) = \mathbf{f} \text{ in } \Omega \tag{6.1}$$

$$\nabla \cdot \mathbf{u} = 0 \text{ in } \Omega \tag{6.2}$$

Eqns. (6.1) and (6.2) represent conservation of linear momentum and mass, respectively, assuming density is constant. In the above $\mathbf{u}$ and p are the fluid velocity and pressure (divided by density), ν is kinematic viscosity, $\nabla^s = \frac{1}{2}\left(\nabla + (\nabla)^T\right)$ is the symmetric spatial gradient, and $\mathbf{f}$ is a body force per unit mass.

6.3 The Space-Discrete Formulation of The Navier-Stokes Equations

In this section we present the residual-based variational multiscale (RBVMS) formulation of the incompressible Navier-Stokes equations originally developed and tested in [1, 3]. For better approximation of thin boundary layers near no-slip walls, various wall-modeling approaches will be employed and compared. In particular, we will explore wall-modeling via weak enforcement of the Dirichlet boundary conditions, proposed in [4].

Let $\mathscr{V}^h$ denote the discrete solution space for the velocity-pressure pair $\{\mathbf{u}^h, p^h\}$ and let $\mathscr{W}^h$ denote the discrete weighting space for the linear momentum and continuity weighting functions $\{\mathbf{w}^h, q^h\}$. The space-discrete Navier-Stokes problem is stated as: Find $\{\mathbf{u}^h, p^h\} \in \mathscr{V}^h$ such that $\forall \{\mathbf{w}^h, q^h\} \in \mathscr{W}^h$,

$$\begin{aligned} B(\{\mathbf{w}^h, q^h\}, \{\mathbf{u}^h, p^h\}) + B_{vms}(\{\mathbf{w}^h, q^h\}, \{\mathbf{u}^h, p^h\}) \\ + B_{wm}(\{\mathbf{w}^h, q^h\}, \{\mathbf{u}^h, p^h\}) = (\mathbf{w}^h, \mathbf{f})_\Omega. \end{aligned} \tag{6.3}$$

In the above, $(\cdot,\cdot)_A$ denotes an L_2-inner product over A. The terms of the above formulation are defined in what follows.

$$\begin{aligned} B(\{\mathbf{w}, q\}, \{\mathbf{u}, p\}) = \left(\mathbf{w}, \frac{\partial \mathbf{u}}{\partial t}\right)_\Omega - (\nabla \mathbf{w}, \mathbf{u} \otimes \mathbf{u})_\Omega + (q, \nabla \cdot \mathbf{u})_\Omega \\ - (\nabla \cdot \mathbf{w}, p)_\Omega + (\nabla^s \mathbf{w}, 2\nu \nabla^s \mathbf{u})_\Omega, \end{aligned} \tag{6.4}$$

is the Galerkin part of the weak form. Furthermore,

$$B_{vms}(\{\mathbf{w}, q\}, \{\mathbf{u}, p\}) = -\left(\nabla \mathbf{w}, \mathbf{u}' \otimes \mathbf{u} + \mathbf{u} \otimes \mathbf{u}' + \mathbf{u}' \otimes \mathbf{u}'\right)_\Omega$$

$$-(\nabla \cdot \mathbf{w}, p')_\Omega - (\nabla q, \mathbf{u}')_\Omega. \tag{6.5}$$

are the RBVMS terms, and the pair $\{\mathbf{u}', p'\}$ denotes the velocity and pressure subgrid scales (i.e., the scales that are too small to be reasonably approximated on a given mesh).

Analogously to [3], the subgrid scales are modeled as

$$\begin{aligned} \mathbf{u}' &= -\tau_M \left(\frac{\partial \mathbf{u}}{\partial t} + \mathbf{u}\nabla\mathbf{u} + \nabla p - \nu\Delta\mathbf{u} - \mathbf{f} \right) \\ p' &= -\tau_C \nabla \cdot \mathbf{u} \end{aligned} \tag{6.6}$$

where τ_M and τ_C are the subgrid-scale parameters defined in Chapter 2.

In the formulation described, the wall-normal component of the flow velocity vector at a Dirichlet boundary, say a wall, is imposed strongly. The other two components of the no-slip wall velocity will not be imposed strongly, but rather a wall model will be prescribed.

6.4 Wall Modeling

6.4.1 Traditional Wall Modeling (TWM)

The term B_{wm} in (6.3) contains the wall model employed in the formulation. In traditional wall model formulations the Dirichlet boundary condition, say at a no-slip wall, is replaced with imposition of the wall shear stress such that

$$B_{wm}(\{\mathbf{w}, q\}, \{\mathbf{u}, p\}) = \left(\mathbf{w}, u^{*2} \frac{\mathbf{u}_{slip}}{||\mathbf{u}_{slip}||} \right)_{\Gamma_{wall}} \tag{6.7}$$

with Γ_{wall} denoting the wall portion of the domain boundary and $||\cdot||$ the Euclidean length. Furthermore, u^{*2} and $\mathbf{u}_{slip}/||\mathbf{u}_{slip}||$ are the magnitude and the direction of the applied wall traction vector, respectively, with $\mathbf{u}_{slip}$ the slip velocity at the wall. In traditional wall modeling, wall friction velocity u^* is obtained by assuming that the LES-computed mean flow speed parallel to the wall at a point A within the log layer (or outer layer) satisfies the classical log law:

$$U^{A+} = \frac{U^A}{u^*} = \frac{1}{\kappa}\log\left(\frac{x_3^A u^*}{\nu}\right) + B \tag{6.8}$$

where x_3^A denotes the wall-normal distance from the wall to point A, and U^A denotes the mean LES-computed flow speed parallel to the wall at point A:

$$U^A = \langle ||\mathbf{u}_t^A|| \rangle \tag{6.9}$$

In the previous expression $\mathbf{u}_t^A$ is the LES-computed fluid velocity parallel to the wall at point A and the brackets denote averaging. Typically the averaging is performed over homogenous directions of the flow, as will both be the case for the results presented further below. Coefficients in (6.8) are $\kappa = 0.41$ (the von Karman constant) and $B = 5.5$. Finally, Eq. (6.8) is non-linear in u^* and is thus solved iteratively for u^* yielding imposed traction magnitude u^{*2} in Eq. (6.7).

Note that in Chapter 4, point A was denoted as a point in the outer layer (ol) or log layer, and notation with superscript ol was used instead of the notation used here with supercript A. Also note that the traditional wall model presented here is slightly different than the traditional wall model used in Chapter 4. In Chapter 4 a more advanced traditional wall model was used in that the computed wall shear stress was pre-multiplied by the ratio $u_1(x_1, x_2, x_3^A, t)/U^A$ (see 4.9) in order

to allow for fluctuations in space. Here we remove this level of complexity in order to facilitate comparison with the other models studied below.

6.4.2 Weak Imposition of The Dirichlet Condition (WD1)

Rather than prescribing the wall shear stress as in the case of traditional wall modeling, a different approach was introduced in [4] based on weak imposition of the no-slip condition at the wall. In this case term B_{wm} in (6.3) is taken as

$$\begin{aligned} B_{wm}(\{\mathbf{w},q\},\{\mathbf{u},p\}) = (\mathbf{w}, -2\nu\nabla^s\mathbf{u}\cdot n)_{\Gamma_{wall}} \\ +(-2\nu\nabla^s\mathbf{w}\cdot n, (\mathbf{u}-g))_{\Gamma_{wall}} \\ +(\mathbf{w}, \tau_B(\mathbf{u}-g))_{\Gamma_{wall}}, \end{aligned} \tag{6.10}$$

containing terms that weakly impose the Dirichlet boundary condition $\mathbf{u} = g$, i.e. $\mathbf{u} = 0$ at the wall. To ensure numerical stability and optimal convergence, the penalty parameter τ_B in Eq. (6.10) is chosen as

$$\tau_B = \frac{C_b\nu}{h_b} \tag{6.11}$$

with $C_b = 4$ and

$$h_b = \frac{2}{\sqrt{n_i G_{ij} n_j}}, \tag{6.12}$$

where n_i's are the Cartesian components of the unit outward normal vector (n) to Γ_{wall}. For rectangular meshes, (6.12) results in the element length in the wall-normal direction.

Description of the terms in Eq. (6.10) as given originally in [4] follows. The first term on the right side of Eq. (6.10) is referred to as the consistency term given than the Euler Lagrange equations for Eq. (6.3) contain a term (arising from integration by parts) that cancels the consistency term. The second term on the right side of Eq. (6.10) is referred to as athe adjoint consistency term. If the exact solution of the adjoint problem is used in Eq. (6.3) as the test function, then (6.3) is satisfied exactly. The third term on the right side of Eq. (6.10) is a penalty term proportional to the deviation of the discrete solution from the Dirichlet (no-slip) condition at the wall.

Recall that the previously described wall modeling approach was used in Chapter 4 in LES-NWM of flow with full-depth Langmuir cells.

6.4.3 Weak Dirichlet Condition Aligned with The Law of The Wall on Fine Meshes (WD2)

The weak imposition of the no-slip condition was re-visited in [5] and a modification was introduced with the goal of aligning the formulation with traditional wall modeling. Rather than calculating τ_B as given by Eq. (6.11), a new expression for τ_B was postulated by comparing the right side of Eq. (6.7) with the third term (i.e. the penatly term) in the right side of Eq. (6.10) with $g = 0$, resulting in

$$\tau_B = \frac{u_{mod}^{*2}}{||\mathbf{u}_{slip}||} \tag{6.13}$$

Modified wall friction velocity u^*_{mod} is computed iteratively through Spalding's formula,

$$x_3^+ = f(u^+) = u^+ + \mathrm{e}^{-\kappa B}\left(\mathrm{e}^{\kappa u^+} - 1 - \chi u^+ - \frac{(\kappa u^+)^2}{2} - \frac{(\kappa u^+)^3}{6}\right), \tag{6.14}$$

with

$$u^+ = \frac{||\mathbf{u}_{slip}||}{u^*_{mod}}, \quad x_3^+ = \frac{x_3^A u^*_{mod}}{\nu} \quad \text{and} \quad x_3^A = \frac{h_b}{C_b} \tag{6.15}$$

Wall-normal mesh size h_b is defined in (6.12) and $C_b = 4$ as before. Note that here Spalding's formula is being evaluated at $x_3^A = h_b/C_b$ with wall slip speed $||\mathbf{u}_{slip}||$ instead of the mean flow speed parallel to the wall at $x_3^A = h_b/C_b$, i.e. $||\mathbf{u}_t^A||$. Consequently, the solution has been denoted here as a modified friction velocity, u^*_{mod}, instead of the actual friction velocity, u^*.

As noted in [5], in the limit of wall-normal mesh refinement in the near-wall region (i.e. letting h_b go to zero), $||\mathbf{u}_{slip}|| \to ||\mathbf{u}_t^A||$, Spalding's formula in (6.14) becomes $x_3^+ = u^+$, and penalty parameter τ_B in Eq. (6.13) becomes independent of $||\mathbf{u}_{slip}||$ taking on the expression

$$\tau_B = \frac{\nu C_b}{h_b} \tag{6.16}$$

Thus, the seemingly disparate evaluation of Spalding's formula at $y_A = h_b/C_b$ with wall slip speed $||\mathbf{u}_{slip}||$ (noted above) is a mathematical construct designed to yield the original formulation of the weak Dirichlet (no-slip) condition in Eqs. (6.10) and (6.11) in the limit $h_b \to 0$. In this limit, the new formulation for τ_B in (6.13) inherits the positive attributes of the original formulation described in [4].

6.4.4 Weak Dirichlet Condition Aligned with Law of The Wall on Coarse and Fine Meshes (WD3)

The modified weak Dirichlet (no-slip) condition in the previous sub-section approaches its original version in the limit of wall-normal mesh refinement. Furthermore, in this limit, the formulation is consistent with the law of the wall. However, when wall-normal mesh size h_b is large, this modified weak Dirichlet condition not only deviates from its original version, but it also deviates from the law of the wall, the latter due to the disparate evaluation of the Spalding's formula described in the previous sub-section. Next, the evaluation of penalty parameter τ_B is re-formulated such that it is aligned with the law of the wall when h_b is large.

Inserting the weak Dirichlet formulation terms in Eq. (6.10) into Eq. (6.3), it is realized that the consistency term in (6.10) (i.e. the first term on the right side of (6.10)) and the penalty term in (6.10) (i.e. the third term on the right side of (6.10)) act as shear stresses at the wall. The consistency term is the resolved molecular shear stress at the wall. Given the under-resolution of the LES velocity in the near-wall region as is the case for near-wall modeling with coarse meshes, the resolved molecular shear stress at the wall (provided by the consistency term) will underpredict the expected wall shear stress based on the flow forcing conditions. Thus, the penalty term is interpreted here as providing the necessesary shear stress (i.e. a "penalty stress") such than when added to the resolved molecular shear stress provided by the consistency term, the sum gives rise to the expected wall shear stress. Symbolically,

$$\{-2\nu\nabla^s\mathbf{u}\cdot n\}_{\Gamma_{wall}} + \{\tau_B(\mathbf{u}-g)\}_{\Gamma_{wall}} = u^{*2}\frac{\mathbf{u}_{slip}}{||\mathbf{u}_{slip}||} \tag{6.17}$$

with $g = 0$. An expression for τ_B can be obtained by dotting the left and right sides of (6.17) with unit vector $\mathbf{u}_{slip}/||\mathbf{u}_{slip}||$ and solving for the former:

$$\tau_B = \frac{1}{||\mathbf{u}_{slip}||}\left[u^{*2} - \nu\left(\frac{\partial||\mathbf{u}_t||}{\partial n}\right)_{\Gamma_{wall}}\right] \tag{6.18}$$

where $\partial||\mathbf{u}_t||/\partial n$ denotes the wall-normal derivative of the velocity parallel to the wall.

Estimation of τ_B via (6.17) has been inspired by a popular technique in RANS (Reynolds-averaged Navier-Stokes) simulations (e.g. see [7]) in which the under-prediction of the wall shear stress by the resolved molecular viscous shear stress is off-set by the introduction of an effective wall viscosity ν_e calculated from

$$\nu_e\left(\frac{\partial||\mathbf{u}_t||}{\partial n}\right)_{\Gamma_{wall}} = u^{*2} \tag{6.19}$$

with the wall-normal derivative of $||\mathbf{u}_t||$ at the wall approximated as

$$\left(\frac{\partial||\mathbf{u}_t||}{\partial n}\right)_{\Gamma_{wall}} \approx \frac{u^A}{x_3^A} \tag{6.20}$$

where x_3^A is the wall-normal distance from the wall to a point A within the log layer. The computed speed parallel to the wall at point A is denoted as $u^A = ||\mathbf{u}_t^A||$. This same approximation of the wall-normal derivative of $||\mathbf{u}_t||$ at the wall is used here to evaluate (6.18).

The formulation proposed above does not recover the original formulation for τ_B ($\tau_B = C_b\nu/h_b$) in the limit $h_b \to 0$, unlike the formulation in sub-section 4.3. Instead, in the limit $h_b \to 0$, it can be shown that the proposed τ_B in Eq. (6.18) goes to zero. However, the proposed formulation does retain the overall structure of the original formulation, comprised of the consistency, adjoint

consistency and penalty terms. Furthemore, the proposed formulation is aligned with the law of the wall for simulations on relatively coarse meshes.

In order to avoid instability of the formulation ocurring when $\tau_B \to 0$, as it does when $h_b \to 0$, and in order to recover the positive attribute of the original formulation in this latter limit, an alternate expression to Eq. (6.18) is adopted:

$$\tau_B = \max(\tau_B^{wall}, \tau_B^{WD}) \tag{6.21}$$

In the previous expression, τ_B^{wall} is given by the right side of Eq. (6.18) based on the law of the wall and τ_B^{WD} is given by the right side of Eq. (6.11) of the original model.

In summary, τ_B is computed from (6.21), with τ_B^{wall} set to the right side of Eq. (6.18) and τ_B^{WD} set to the right side of Eq. (6.11). In (6.18), the wall-normal derivative of $||\mathbf{u}_t||$ at the wall is obtained via (6.20) with U^A being the LES-computed speed parallel to the wall at point A. Point A is taken within the log layer. Wall friction velocity u^* in Eq. (6.18) is computed iteratively via (6.8).

6.5 Computational Setup

The flow consists of a pressure gradient-driven open channel flow. The computational domain, depicted in Figure 6.1, is a rectangular channel with dimensions $4\pi\delta \times 2\delta \times \frac{8}{3}\pi\delta$ in the stream-wise (x_1 or x), wall-normal (x_2 or y), and span-wise (x_3 or z) directions, respectively. The half-height of the domain (in the y-direction) is δ. The open top surface of the channel is at $x_3 = 2\delta$ and the bottom wall is at $x_3 = 0$.

No-penetration boundary condition ($v = 0$) is imposed strongly at the open top surface and at the bottom wall. Furthermore, the open top surface is characterized by an imposed zero shear stress and the bottom wall is treated with the wall models described in section 4.

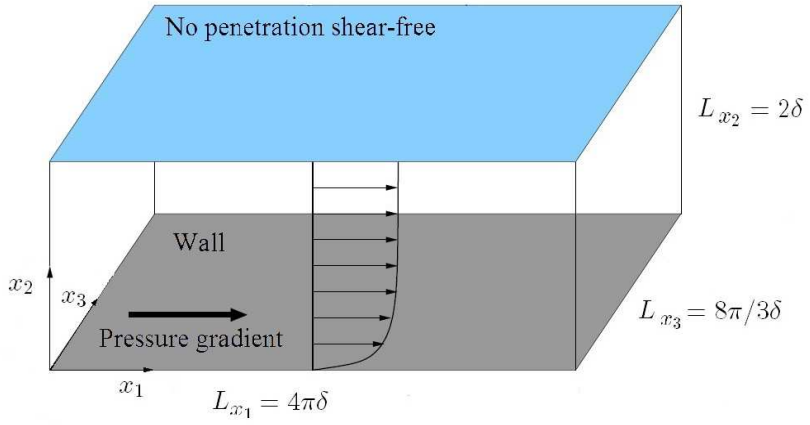

Figure 6.1: Computational domain.

The flow is driven by an imposed pressure gradient (or body force) in the x direction and thus $\mathbf{f} = (f_1, 0, 0)$ in Eq. (6.1). The first entry of this vector, f_1, is chosen to drive flow at $Re = 395$ where the Reynolds number ($Re = u^* \delta / \nu$) is based on friction velocity u^* and channel half-height (δ).

Periodic boundary conditions are set in the homogeneous directions of this flow, that is the stream-wise (x) and spanwise (z) directions.

Just as in Chapter 4, quadratic NURBS (non-unform rational B-splines) that are C^1-continuous across mesh knots are employed in the computations. The mesh used consists of $64 \times 64 \times 32$ quadratic NURB elements in the x, y and z directions. These elements are of uniform size in all three directions.

The traditional wall model in sub-section 4.1 and the wall model based on weak imposition of the no-slip condition and the law of the wall in sub-section 4.4 both require evaluation of the LES velocity parallel to the wall at a point A within the log layer. In the current implementation, point A is taken to be at a distance $z^+ = 24.7$ from the wall, within the log layer. This location corresponds to the first level of mesh (element) points away from the wall.

6.6 Numerical Results

Next, results are presented from LES-NWM of the open channel flow with the quadratic NURBS mesh described in the previous section and the various wall models described in Section 4: WD2, WD3 and TWM. Note that the wall models in sub-section 4.2 and 4.3 are denoted as WD1 and WD2, respectively, and the wall model given through the expression in Eq. (6.21) in sub-section 4.4 is referred to as WD3. The traditional wall model described in sub-section 4.1 is denoted as TWM. LES results with these models are compared with DNS results of channel flow of [37]. Results with WD1 are not included in this comparison because they are very close to results with WD2 (for example, see [5]).

Figure 6.2 shows mean velocity in wall units from DNS and LES-NWW with the various wall treatments. Mean velocity profiles obtained with the various wall treatments are in overall good agreement with the DNS and the theoretical log law. For $x_3^+ > 50$, the TWM gives rise to an under-prediction of velocity relative to the various near-wall treatments based on weak imposition of the no-slip condition. The newly introduced WD3 (the wall model based on weak imposition of no-slip aligned with the law of wall for relatively coarse meshes) leads to a slighlty improved prediction of mean velocity compared to its predecessor WD2 and also TWM. Looking at mean

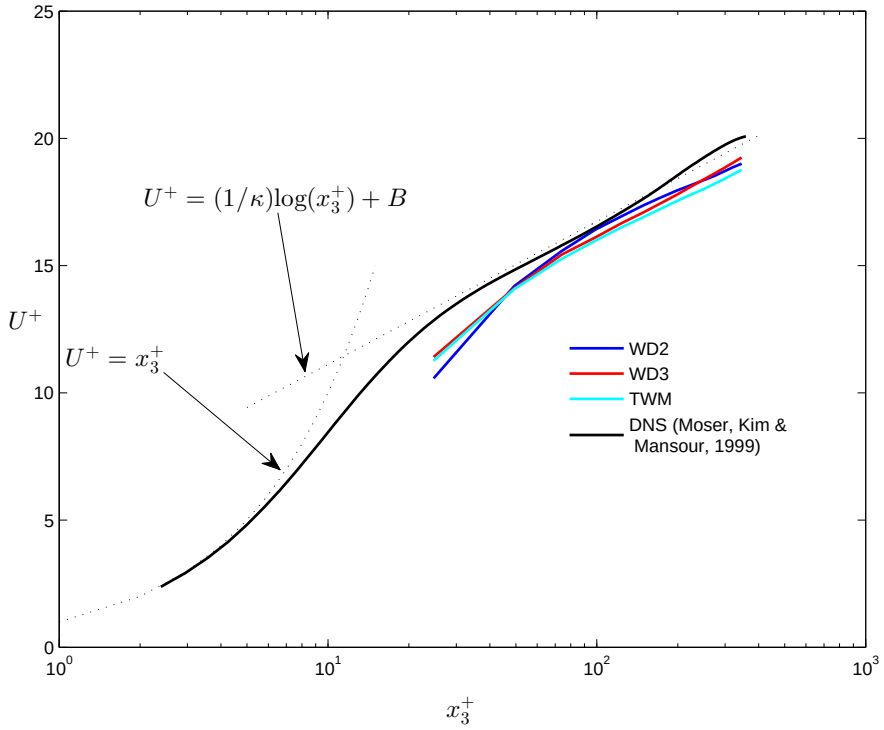

Figure 6.2: Mean velocity in log wall units from DNS and LES-NWR with various wall treatments. WD2 and WD3 are wall models of sub-sections 4.3 and 4.4, respectively; TWM is the wall model of sub-section 4.1. The theoretical log law is plotted with $\kappa = 0.41$ and $B = 5.5$.

velocity in Figure 6.3 it can be seen that the WD3 leads to better prediction of the bulk velocity compared to both WD2 and TWM with respect to the DNS.

Figure 6.4 shows root mean square (rms) of velocity in wall units from DNS and LES-NWM with the various wall treatments. The WD3 formulation results in an improved prediction of the streamwise velocity rms (u_1-rms) compared with WD2 in the approximate range $100 < x_3^+ < 225$. LES with WD3 predicts u_1-rms in excellent agreement with the DNS within this range. The WD3 formulation also provides an improved prediction of the peak u_1-rms. Furthermore, the WD3 model leads to significant improvements over WD2 in terms of spanwise (u_2-rms) and wall-normal (u_2-rms) velocity rms throughout most of the channel. Overall, the velocity rms prediction with the WD3 model is in close agreement with the prediction obtained with the TWM.

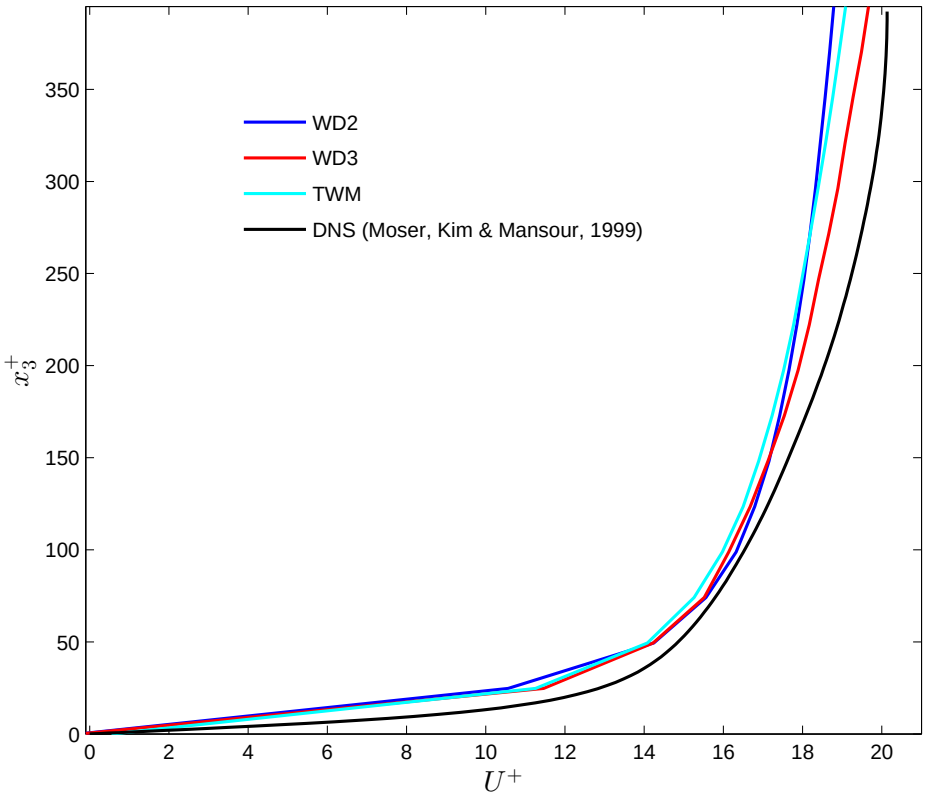

Figure 6.3: Mean velocity in wall units from DNS and LES-NWR with various wall treatments. WD2 and WD3 are wall models of sub-sections 4.3 and 4.4, respectively; TWM is the wall model of sub-section 4.1.

Finally, instantaneous snapshots of the speed of the flows with the different near-wall treatments can be seen in Figure 6.5. The TWM and WD3 wall treatments lead to a more active near-wall region characterized by more energetic eddies emmanating from this region in comparison to WD2 which leads to greater dampening of the turbulence with decreasing distance to the wall.

6.7 Summary

In LES-NWM with weak imposition of the no-slip condition at the wall, the wall model consists of augmenting the variational (weak) form of the Navier-Stokes equations with terms that enforce

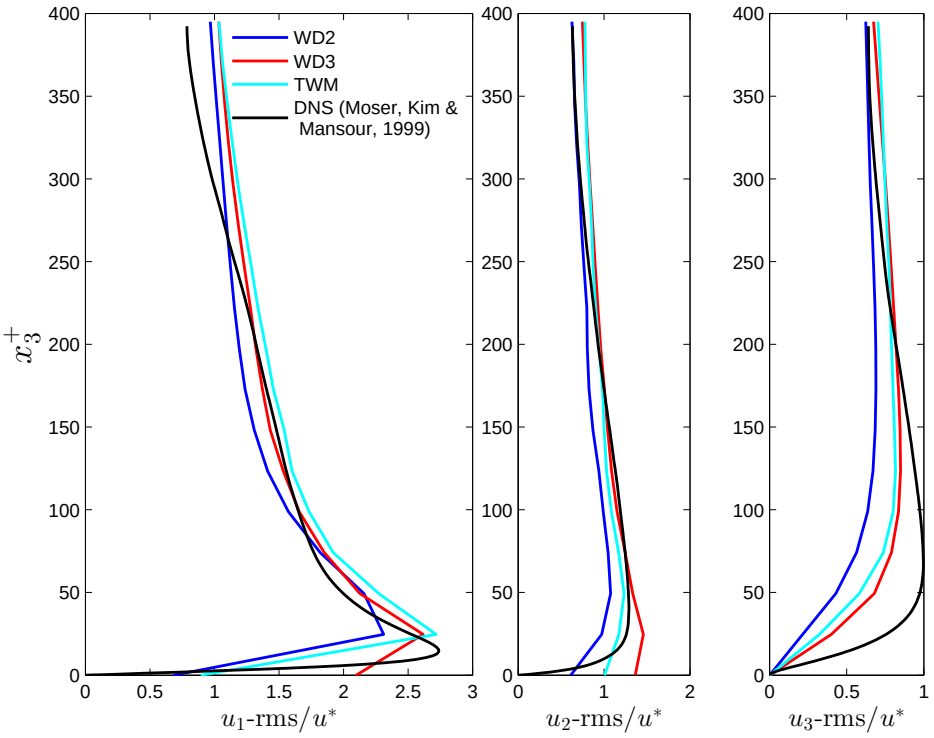

Figure 6.4: Root mean square (rms) of velocity in wall units from DNS and LES-NWR with various near-wall treatments. WD2 and WD3 are wall models of sub-sections 4.3 and 4.4, respectively; TWM is the wall model of sub-section 4.1. Streamwise velocity rms (u_1-rms) is in the left panel, spanwise velocity rms (u_2-rms) is in the middle panel and wall-normal velocity rms (u_3-rms) is in the right panel.

the no-slip conditions weakly as Euler Lagrange conditions [4]. Weak imposition of the no-slip condition is primarily based on numerical considerations and not on physical conditions as is the case of traditional wall modeling. In this chapter, weak imposition of the no-slip condition was re-visited and reformulated to be fully consistent with the law of the wall, while simultaneously possessing the positive attributes of the earlier weak Dirichlet formulations. For an open channel flow simulation, the new formulation led to improved results in terms of mean velocity and rms of velocity while allowing more energetic near-wall flow structures.

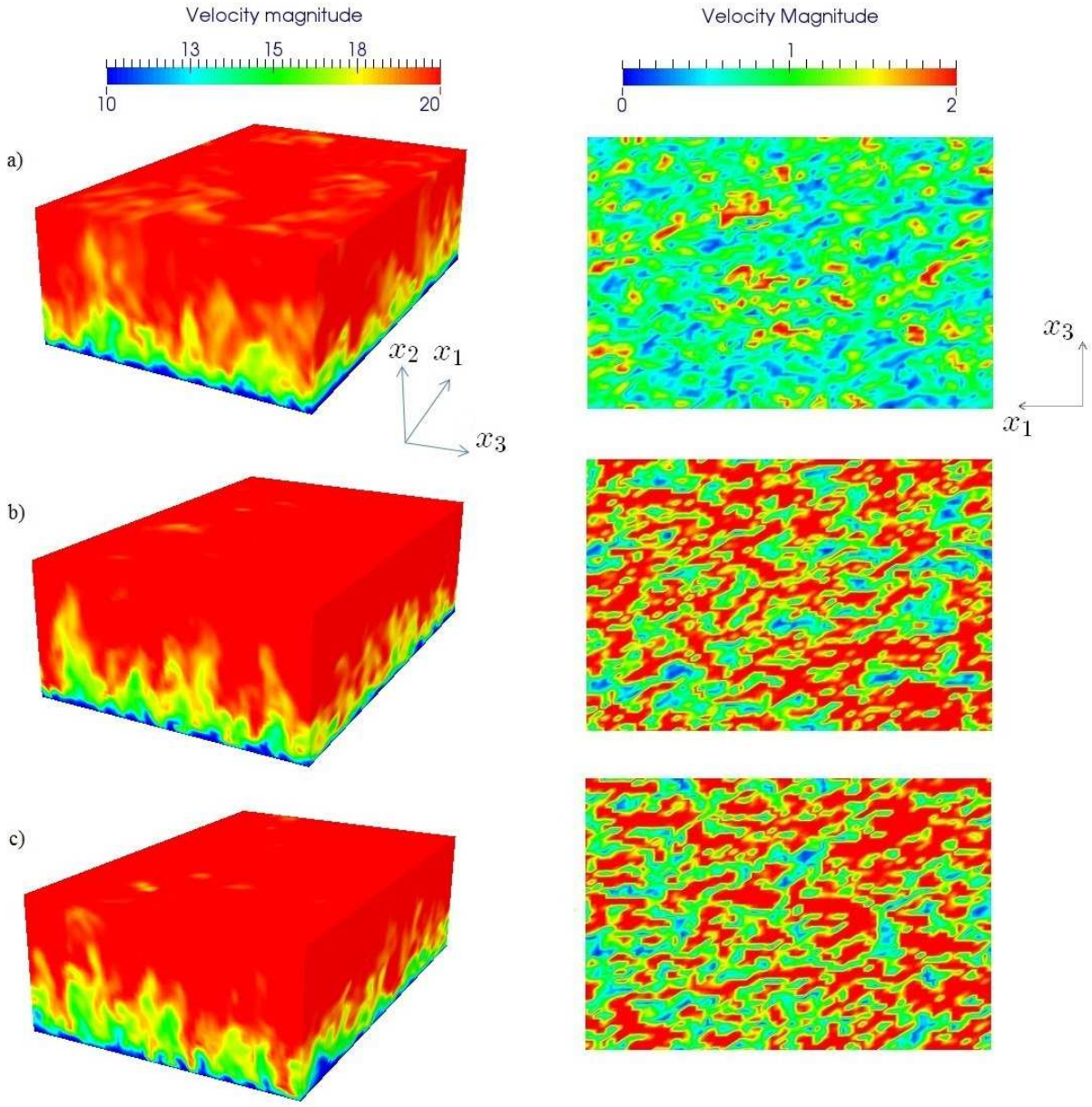

Figure 6.5: Instantaneous snapshot of flow speed in simulations with (a) WD1, (b) WD2 and (c) TWM in 3D (left panels) and on the bottom wall (right panels). Mean speed is scaled by friction velocity.

Chapter 7:

Summary and Future Research

The developments presented in this dissertation constitute an initial attempt towards residual-based variational multiscale (RBVMS) large-eddy simulation (LES) of the coastal ocean. The RBVMS with quadratic NURBS (non-Uniform rational B-splines) basis functions was chosen due to its flexibility in potentially representing complex geometry features as well as its accurate representation of turbulent flow fields [3].

In this dissertation, RBVMS LES simulations of Langmuir turbulence in shallow water were performed. Langmuir turbulence is generated by interaction between waves and the wind-driven shear current. In shallow coastal shelf regions Langmuir turbulence is characterized by full-depth Langmuir cells consisting of parallel counter-rotating vortices aligned in the direction of the winds. This turbulence regime has important physical, chemical and biological implications as it promotes vertical mixing throughout the entire water column and can also impact lateral (horizontal) mixing at the submesoscales. In RBVMS LES of Langmuir turbulence, the RBVMS method serves to stabilize the discretization which is generally unstable under the advective nature of the governing equations for the Langmuir turbulence regime. The RBVMS also served as a subgrid-scale model in the sense of LES.

The governing equation for Langmuir turbulence consist of the Craik-Leibovich vortex force augmenting the Navier-Stokes equation. In Chapter 3, the Craik-Leibovich vortex force was expressed in advective form and the RBVMS method was applied to develop a stable, LES formu-

lation of the momentum equation. This RBVMS LES formulation with quadratic NURBS was used to perform LES of Langmuir turbulence in shallow water and was shown to possess good convergence characteristics in terms of predicted mean downwind velocity and turbulent kinetic energy.

Wall modeling, an important component towards RBVMS LES of the coastal ocean, was discussed in Chapter 4. In wall-bounded turbulent flows such as those characterizing the coastal ocean, resolution of the bottom viscous boundary layer is computationally expensive requiring fine mesh resolution in order to resolve sharp velocity gradients and small-scale eddies of size on the order of their distance to the bottom. A wall model can be introduced in the LES in order to predict the correct wall shear stress without having to resolve the viscous layer. Thus the simulation resolves the core flow region while relying on the wall model to prescribe the wall shear stress rather than imposing the no-slip condition at the wall. In Chapter 4, RBVMS LES with near wall-modeling (LES-NWM) of Langmuir turbulence in shallow water was performed. A key issue investigated via these simulations is that traditional wall models assume the existence of a near-wall log layer. However, LES-NWR (i.e. LES with near-wall resolution) in Chapter 3 showed that full-depth Langmuir cells induce log-layer disruption, for example, in terms of a departure or deviation from the mean velocity log-law. This deviation may be approximated by shifting the log-law velocity profile

$$U^+ = \frac{1}{\kappa}\log(z^+) + B \tag{7.1}$$

via an adjustment of the B coefficient from its traditional value $B = 5.5$ to a value greater than 5.5. Remarkably, RBVMS LES-NWM of Langmuir turbulence in shallow water employing a traditional wall model was found to be roughly independent of the value of the B coefficient,

thereby eliminating the need for tuning the B coefficient. The main reason for this was that it is the strength of the full-depth Langmuir cell that sets the deviation away from the log-law for the mean velocity. If the core flow is well-resolved, as can be the case in LES-NWM, then the full-depth Langmuir cells are also well-resolved, ultimately leading to accurate prediction of log-layer disruption caused by the cells without the need to tune the wall model with the correct value of B.

In Chapter 4, RBVMS LES-NWM allowed simulations of Langmuir turbulence in shallow water on horizontally (downwind and crosswind) expanded domains domains. These wider domains allowed for resolution of multiplied Langmuir cells. Despite lateral (horizontal) interactions between the cells in these simulations with wider domains, vertical mixing characteristics were found to be similar to those in simulations with smaller domains.

In Chapter 5, simulations of Langmuir turbulence in shallow water were performed based on the Reynolds-averaged governing equations. These equations reduced to a single water column model for the mean velocity of the wind and wave-driven flow with an eddy viscosity stress and a non-local stress accounting for the effects of unresolved full-depth Langmuir cells and associated turbulence. Unlike in LES-NWM, the single water column model with a traditional wall model did show sensitivity to the B coefficient in the assumed log-law velocity profile. Remarkably, a recent wall-model (introduced in [4]) based on weak imposition of the wall no-slip condition led to a mean velocity in good agreement with that from LES-NWR without the need to tune parameters. Note that this wall treatment does not make any assumptions about the existence of a log-law, unlike traditional wall models.

In the coastal ocean, LES-NWR has shown that Langmuir cells can be periodically destroyed by the action of the tides thereby restoring the log-layer [45]. Finally, in Chapter 6, given the near-universality of wall-bounded flows characterized by a log-layer, a new wall-model based on

weak imposition of the no-slip wall was developed in accordance with the law of the wall (e.g. the log law). This model was also designed to retain the functional form of the original model based on weak imposition of the no-slip wall. This form ensures stability and convergence of the overall formulation (discretization) [4]. In RBVMS LES-NWM of open channel flow (without Langmuir turbulence) the new wall model led to improved results in terms of mean velocity and rms of velocity over its predecessor.

Before moving on to coastal LES featuring complex geometries (boundaries), future research should focus on extending the RBVMS formulation to stratified turbulent flows. In particular, stable stratification leads to suppression of turbulence fluctuations [2], and thus a numerical method that can accurately capture this effect is of importance. Stably stratified turbulence has been numerically studied primarily using pseudo-spectral discretization techniques and the ability of lower order discretizations to accurately represent this turbulence regime remains largely unexplored.

References

[1] I. Akkerman, Y. Bazilevs, V.M. Calo, T.J.R. Hughes, and S. Hulshoff. The role of continuity in residual-based variational multiscale modeling of turbulence. *Computational Mechanics*, 41:371–378, 2008.

[2] V. Armenio and S. Sarkar. An investigation of stably stratified turbulent channel flow using large-eddy simulation. *Journal of fluid mechanics*, 459:1–42, 2003.

[3] Y. Bazilevs, V.M. Calo, J.A. Cottrel, T.J.R. Hughes, A. Reali, and G. Scovazzi. Variational multiscale residual-based turbulence modeling for large eddy simulation of incompressible flows. *Computer Methods in Applied Mechanics and Engineering*, 197:173–201, 2007.

[4] Y. Bazilevs and T.J.R. Hughes. Weak imposition of Dirichlet boundary conditions in fluid mechanics. *Computers and Fluids*, 36:12–26, 2007.

[5] Y. Bazilevs, C. Michler, V.M. Calo, and T.J.R. Hughes. Weak Dirichlet boundary conditions for wall-bounded turbulent flows. *Computer Methods in Applied Mechanics and Engineering*, 196:4853–4862, 2007.

[6] J.P. Boris, F.F. Grinstein, E.S. Oran, and R.L. Kolbe. New insights into large eddy simulation. *Fluid Dynamics Research*, 10:199–229, 1992.

[7] J. Bredberg. On the wall boundary condition for turbulence models. Technical report, Department of Thermo and Fluid Dynamics, Chalmers University of Technology, 2000.

[8] A.N. Brooks and T.J.R Hughes. Streamline Upwind / Petrov-Galerkin formulations for convection dominated flows with particular emphasis on the incompressible navier-stokes equations. *Computer Methods in Applied Mechanics and Engineering*, 32:199–259, 1982.

[9] A.N. Brooks and T.J.R. Hughes. Streamline upwind/Petrov-Galerkin formulations for convection dominated flows with particular emphasis on the incompressible Navier-Stokes equations. *Computer Methods in Applied Mechanics and Engineering*, 32:199–259, 1982.

[10] H. Burchard. *Applied Turbulence Modelling in Marine Waves*. Springer, 2002.

[11] A. D. D Craik and S. Leibovich. A rational model for Langmuir circulation. *Journal of Fluid Mechanics*, 73:401–426, 1976.

[12] E.D. Denman and A.N. Beavers. The matrix sign function and computations in systems. *Appl. Math. Comput.*, 2:63–94, 1976.

[13] J. Donea and A. Huerta. *Finite Element Methods for Flow Problems*. John Wiley and Sons, 2005.

[14] M. A. Donelan. Air-water exchange processes. In J. Imberger, editor, *Physical Processes in Lakes and Oceans*, Coastal and Estuarine Studies, pages 19–36. American Geophysical Union, 1998.

[15] S.M. Durski. Vertical mixing schemes in the coastal ocean: Comparison of the level 2.5 mellor-yamada scheme with an enhanced version of the k-profile parameterization. *Jounal of Geophysical Research*, 109:C01015, 2004.

[16] C. Fureby and F.F. Grinstein. Monotonically integrated large eddy simulation of free shear flows. *AIAA Journal*, 37:544–556, 1999.

[17] A.E. Gargett and J.R. Wells. Langmuir turbulence in shallow water. Part 1. observations. *Journal of Fluid Mechanics*, 576:27–61, 2007.

[18] A.E. Gargett, J.R. Wells, A.E. Tejada-Martínez, and C.E. Grosch. Langmuir supercells: A mechanism for sediment resuspension and transport in shallow seas. *Science*, 306:1925–1928, 2004.

[19] R.D. Hetland. Submesoscale eddies along the Mississippi/Atchafalaya river plume front. Ocean Sciences Meeting, 2014.

[20] T.J.R Hughes. *The finite element method: Linear static and dynamic finite element analysis*. Prentice Hall, Englewood Cliffs, NJ, 1987.

[21] T.J.R. Hughes. Multiscale phenomena: GreenâĂŹs functions, the Dirichlet-to-Neumann formulation, subgrid scale models, bubbles and the origins of stabilized methods. *Computer Methods in Applied Mechanics and Engineering*, 127:387–401, 1995.

[22] T.J.R. Hughes, J.A. Cottrell, and Y. Bazilevs. Isogeometric analysis: Cad, finite elements, nurbs, exact geometry, and mesh refinement. *Computer Methods in Applied Mechanics and Engineering*, 194:4135–419, 2005.

[23] T.J.R. Hughes, L.P. Franca, and M. Mallet. A new finite element formulation for fluid dynamics: VI. Convergence analysis of the generalized SUPG formulation for linear time–dependent multidimensional advective–diffusive systems. *Computer Methods in Applied Mechanics and Engineering*, 63:97–112, 1987.

[24] T.J.R. Hughes and M. Mallet. A new finite element formulation for fluid dynamics: III. The generalized streamline operator for multidimensional advective-diffusive systems. *Computer Methods in Applied Mechanics and Engineering*, 58:305–328, 1986.

[25] T.J.R Hughes, L. Mazzei, and K.E. Jansen. Large eddy simulation and the variational multiscale method. *Computing and Visualization in Science*, 3:47–59, 2000.

[26] T.J.R. Hughes, G. Scovazzi, and L.P. Franca. Multiscale and stabilized methods. In E. Stein, R. de Borst, and T. J. R. Hughes, editors, *Encyclopedia of Computational Mechanics, Vol. 3, Computational Fluid Dynamics*, chapter 2. Wiley, 2004.

[27] K.E. Jansen. Unstructured grid large eddy simulation of flow over an airfoil. *Annual Research Briefs*, Center for Turbulence Research, NASA Ames/Stanford University:161–173, 1994.

[28] K.E. Jansen. A stabilized finite element method for computing turbulence. *Computer Methods in Applied Mechanics and Engineering*, 174:299–317, 1999.

[29] K.E. Jansen and A.E. Tejada-Martinez. An evaluation for the variational multiscale model for large-eddy simulation using a hierarchical basis. 40th AIAA Aerospace Sciences Meeting and Exhibit, AIAA Paper 2002-0283, 2002.

[30] K.E. Jansen, C.H. Whiting, and G.M. Hulbert. A generalized alpha method for integrating the navier-stokes equations with a stabilize element method. *cmame*, 190:305–319, 1999.

[31] I. Langmuir. Surface motion of water induced by wind. *Science*, 87:119–123, 1938.

[32] W. Large, McWilliams J., and S. Doney. Oceanic vertical mixing: A review and a model with non-local boundary layer parameterization. *Reviews of Geophysics*, 32:363–403, 1994.

[33] P. H. LeBlond and L. A. Mysak. *Waves in the Ocean*. Elsevier, 1977.

[34] M. Li, C. Garrett, and E. Skyllingstad. A regime diagram for classifying turbulent large eddies in the upper ocean. *Deep-Sea Research I*, 52:259–278, 2005.

[35] J. Marshall, C. Hill, L. Perelman, and A. Adcroft. Hydrostatic, quasi-hydrostatic, and nonhydrostatic ocean modeling. *Journal of Geophysical Research*, 102:5733–5752, 1997.

[36] J. C. McWilliams, P.P. Sullivan, and C.H. Moeng. Langmuir turbulence in the ocean. *Journal of Fluid Mechanics*, 334:31–58, 1997.

[37] R. Moser, J. Kim, and R. Mansour. DNS of turbulent channel flow up to $Re = 590$. *Physics of Fluids*, 11:943–945, 1999.

[38] Hamlington P.E., Van Roeckel L.P., B. Fox-Kemper, Julien K., and G.P. Chini. Langmuir submesoscale interactions: Descriptive analysis of multiscale frontal spin-down simulations. *Journal of Physical Oceanography*, in press, 2014.

[39] A. Petronio, F. Roman, C. Nosello, and V. Armenio. Large eddy simulation model for wind-driven sea circulation in coastal areas. *Nonlinear Processes in Geophysics*, 20:1095–1112, 2013.

[40] O. M. Phillips. *The Dynamics of the Upper Ocean*. Cambridge U. Press, 1966.

[41] U. Piomelli and E. Balaras. Wall-layer models for large-eddy simulations. *Annual Review of Fluid Mechanics*, 38(4):924–938, 2002.

[42] U. Piomelli and E. Ballaras. Wall-layer models for large-eddy simulations. *Annual Review of Fluid Mechanics*, 34:349–374, 2002.

[43] S. B. Pope. *Turbulent Flows*. Cambridge University Press, 2000.

[44] F. Shakib, T.J.R. Hughes, and Z. Johan. A new finite element formulation for computational fluid dynamics: X. The compressible Euler and Navier-Stokes equations. *Computer Methods in Applied Mechanics and Engineering*, 89:141–219, 1991.

[45] N. Sinha. *Numerical simulations of the stratified oceanic bottom boundary layer*. PhD thesis, University of South Florida, Tampa, 2013.

[46] E.D. Skyllingstad and D.W. Denbo. A ocean large-eddy simulation of langmuir circulations and convection in the surface mixed layer. *Journal of Geophysical Research*, 100:501–522, 1995.

[47] E.D. Skyllingstad and R.M Samelson. Baroclinic frontal instabilities and turbulent mixing in the surface boundary layer. part i: Unforced simulations. *Journal of Physical Oceanography*, pages 1701–1716, 2012.

[48] E.D. Skyllingstad and R.M. Samelson. Large-eddy simulations of baroclinic instability and turbulent mixing. Technical report, ONR, 2014.

[49] J. Smagorinsky. General circulation experiments with the primitive equations I. the basic experiment. *Monthly Weather Review*, 91:3:99–164, 1963.

[50] P. P. Sullivan and J. C. McWilliams. Dynamics of winds and currents coupled to surface waves. *Annual Review of Fluid Mechanics*, 42:19–42, 2010.

[51] P. P. Sullivan, J. C. McWilliams, and W. K. Melville. Surface gravity wave effects in the oceanic boundary layer: Large-eddy simulaion with vortex force and stochastic forcing. *Jounal of Fluid Mechanics*, 593:405–452, 2007.

[52] A. E. Tejada-Martínez and C. E. Grosch. Langmuir turbulence in shallow water. part 2. large-eddy simulation. *Journal of Fluid Mechanics*, 576:63–108, 2007.

[53] A. E. Tejada-Martínez, C. E. Grosch, N. Sinha, C. Akan, and G. Martinat. Disruption of bottom log layer in large-eddy simulations of full-depth Langmuir circulation. *Journal of Fluid Mechanics*, 699:79–93, 2012.

[54] A.E. Tejada-Martínez, I. Akkerman, and Y. Bazilevs. Large-eddy simulation of shallow water langmuir turbulence using isogeometric analysis and the residual-based variational multiscale method. *Journal of Applied Mechanics*, 79:1:205–213, 2012.

[55] A.E. Tejada-Martínez, C.E. Grosch, A.E. Gargett, J.A Polton, J.A. Smith, and J.A. MacKinnon. A hybrid spectral/finite-difference large-eddy simulator and turbulent processes in the upper ocean. *Ocean Modelling*, 39:115–142, 2009.

[56] A.E. Tejada-Martínez and K.E. Jansen. On the interaction between dynamic model dissipation and numerical dissipation due to Streamline Upwind / Petrov-Galerkin stabilization. *Computer Methods in Applied Mechanics and Engineering*, 194:1225–1248, 2005.

[57] T. Tezduyar. Computation of moving boundaries and interfaces and stabilization parameters. *International Journal for Numerical Methods in Fluids*, 43:555–575, 2002.

[58] S. A. Thorpe. Langmuir circulation. *Annual Reviews of Fluid Mechanics*, 36:55–79, 2004.

[59] S.A. Thorpe. *Ocean Turbulence*. Cambridge University Press, 2007.

[60] C. Whiting. *Stabilized Finite Element Methods for fluid dynamics using a hierarchical basis*. PhD thesis, Rensselaer Polytechnic Institute, 1999.

[61] M. Zhou, O. Sahni, T. Xie, M.S. Shephard, and K.E. Jansen. Unstructured mesh partition improvement for implicit finite element at extreme scale. *Jounal of Supercomputing*, 59:1218–1228, 2012.

Appendices

Appendix A Copyright Permissions

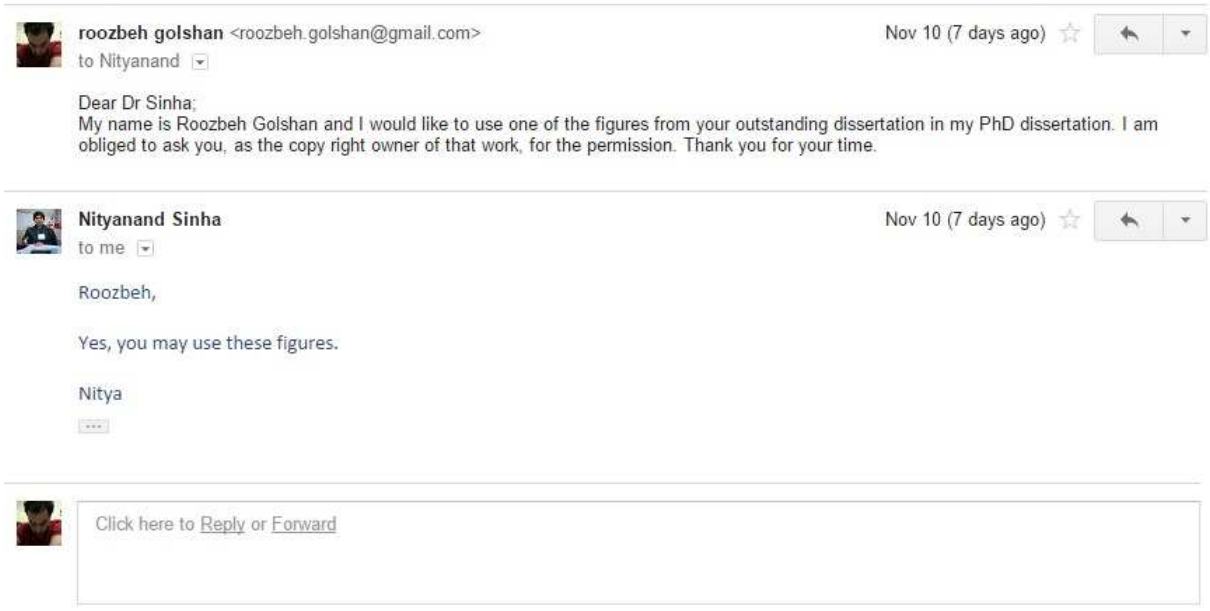

roozbeh golshan <roozbeh.golshan@gmail.com> Nov 10 (7 days ago)
to Nityanand

Dear Dr Sinha;
My name is Roozbeh Golshan and I would like to use one of the figures from your outstanding dissertation in my PhD dissertation. I am obliged to ask you, as the copy right owner of that work, for the permission. Thank you for your time.

Nityanand Sinha Nov 10 (7 days ago)
to me

Roozbeh,

Yes, you may use these figures.

Nitya

Click here to Reply or Forward

In this Appendix, Copyright permissions for use of materials in chapters 1,3 and 4, are presented respectively. Above is the screen-cap of email correspondence between me and dr Sinha regarding the permission request for a figure I used in Chapter 1. The following two permission documents correspond to the figures I used in chapters 3 and 4 respectively. I would like to thank Dr Sinha, Elsevier Publishing Company and Cambridge University Press, for providing me with these permission documents in such short amount of time.

ELSEVIER LICENSE
TERMS AND CONDITIONS

Nov 12, 2014

This is a License Agreement between Roozbeh Golshan ("You") and Elsevier ("Elsevier") provided by Copyright Clearance Center ("CCC"). The license consists of your order details, the terms and conditions provided by Elsevier, and the payment terms and conditions.

All payments must be made in full to CCC. For payment instructions, please see information listed at the bottom of this form.

Supplier	Elsevier Limited The Boulevard,Langford Lane Kidlington,Oxford,OX5 1GB,UK
Registered Company Number	1982084
Customer name	Roozbeh Golshan
Customer address	15210 Amberly Drive TAMPA, FL 33647
License number	3503110623331
License date	Nov 06, 2014
Licensed content publisher	Elsevier
Licensed content publication	Computer Methods in Applied Mechanics and Engineering
Licensed content title	Variational multiscale residual-based turbulence modeling for large eddy simulation of incompressible flows
Licensed content author	Y. Bazilevs,V.M. Calo,J.A. Cottrell,T.J.R. Hughes,A. Reali,G. Scovazzi
Licensed content date	1 December 2007
Licensed content volume number	197
Licensed content issue number	1-4
Number of pages	29

PERMISSION INVOICE

Inv. # P03J 24555

November 7, 2014

Roozbeh Golshan
15210 Amberly Drive 423
Tampa, FL, 33467

CAMBRIDGE UNIVERSITY PRESS

32 Avenue of the Americas
New York, NY 10013-2473, USA

www.cambridge.org

Telephone 212 924 3900
Fax 212 691 3239

REFERENCE

ISSN: EISSN:

Journal:	Journal of Fluid Mechanics, Volume 576 / April 2007, pp. 27-61
Author:	ANN E. GARGETT and JUDITH R. WELLS
Title:	Langmuir turbulence in shallow water. Part 1. Observations
Selection/pp.:	Figure 6, p. 43

USE

Reprint Title:	Residual-based Variational Multiscale LES of Stratified Oceanic Boundary Layers in Shallow Water
Publisher:	University of South Florida
Format:	dissertation / thesis
Quantity (Limit*):	100
Avail. Date:	2014